

OPTIMAL DESIGN OF HYBRID RENEWABLE ENERGY SYSTEM

FOR MICROGRID RELIABILITY ENHANCEMENT

BY

ABASS AFOLABI YAHAYA

A Thesis Presented to the
DEANSHIP OF GRADUATE STUDIES

KING FAHD UNIVERSITY OF PETROLEUM & MINERALS

DHAHRAN, SAUDI ARABIA

In Partial Fulfillment of the
Requirements for the Degree of

MASTER OF SCIENCE

In

ELECTRICAL ENGINEERING

MAY, 2016

KING FAHD UNIVERSITY OF PETROLEUM & MINERALS

DHAHRAN- 31261, SAUDI ARABIA

DEANSHIP OF GRADUATE STUDIES

This thesis, written by **ABASS AFOLABI YAHAYA** under the direction his thesis advisor and approved by his thesis committee, has been presented and accepted by the Dean of Graduate Studies, in partial fulfillment of the requirements for the degree of **Master of Science** in **Electrical Engineering**.



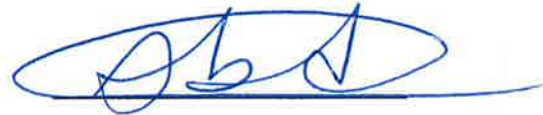
Dr. Ali Ahmad Al-Shaikhi
Department Chairman



Dr. Mohammad M. Al-Muhaini
(Advisor)



Dr. Salam A. Zummo
Dean of Graduate Studies



Dr. Mohammad Abido
(Member)

5/6/15

Date



Dr. Ibrahim O.A. Habiballah
(Member)

© Abass Afolabi Yahaya

2016

This thesis is dedicated to future minds that will continue to strive and thrive

ACKNOWLEDGMENTS

I will like to acknowledge the Kingdom of Saudi Arabia for giving me the wonderful opportunity to study my Masters in Electrical Engineering via its prestigious scholarship program. I also like to thank the citadel of learning, King Fahd University of Petroleum and Minerals (KFUPM), for being the platform of my academic endeavor in the Kingdom. I am grateful to my advisor, Dr. M. Al-Muhaini for his patience and encouragements all through. I will like to give thanks my thesis committee members, Dr. M.A. Abido and Dr. O.I. Habiballah, for their support and advices. My family, in persons of my wife, my parents, and siblings, have been really supportive too. I cannot afford not to mention the Nigerian community in KFUPM for its wonderful social and financial supports. And lastly, my roommate, colleagues, and lecturers have all been very wonderful.

TABLE OF CONTENTS

ACKNOWLEDGMENTS.....	v
LIST OF TABLES.....	ix
LIST OF FIGURES.....	x
LIST OF ABBREVIATIONS.....	xii
ABSTRACT.....	xvii
ملخص الرسالة.....	xix
CHAPTER 1: INTRODUCTION.....	1
1.1 Thesis Motivation.....	2
1.2 Thesis Objectives.....	4
1.3 Thesis Organization.....	5
CHAPTER 2: LITERATURE REVIEW	6
2.1 Reliability Effects of Wind and Solar Energy on Microgrids.....	6
2.2 DG Sizing and Placement to Improve Reliability	8
2.3 Models of the Solar and Wind DGs	10
CHAPTER 3: SYSTEM MODELING	14
3.1 Solar DG Model.....	14
3.1.1 Sandia Array Performance Model (SAPM)	14
3.1.2 Luft et al's Model.....	16
3.1.3 Improvement of Luft et al's Model	16

3.1.4	Hadj Arab et al Model	18
3.1.5	The 5-Parameter Model	20
3.2	Wind DG Models	23
3.3	Battery Energy Storage System	25
3.3.1	Third Order Battery Dynamic Model	27
3.3.2	A Simple Battery Model	29
3.4	Conventional DG Model	30
3.5	Modeling Output of the Power Sources on a Long-Term Basis	31
3.5.1	Solar PV Power Output	31
3.5.2	Wind Power Output	33
3.5.3	Combined Wind Turbine and Solar PV Power Output	38
3.5.4	Combined Wind Turbine, Solar PV and Conventional DG Power Output	38
3.5.5	Combined Solar PV Power and Energy Storage	39
CHAPTER 4: PROBLEM FORMULATION AND METHODS		41
4.1	Proposed General Network Tie Set Algorithm	41
4.2	Monte-Carlo Simulation and Inverse Transform Method	44
4.3	Proposed Method to Obtain Reliability Indices	46
4.4	Problem Formulation	48
4.4.1	Load Point Reliability Indices	48
4.4.2	System Reliability Indices	51
4.4.3	Objective Functions and Constraints	52
4.5	Mixed-Integer Multi-Objective Particle Swarm Optimization	55
4.5.1	Dealing with the Discrete Variable	57

4.6 Theory of Calculating the Objective Functions.....	58
4.7 Other Important Algorithms	62
4.7.1 Clustering Algorithm	62
4.7.2 Fuzzy Approach to Extract Best Compromise Solution	62
CHAPTER 5: SIMULATION AND RESULTS.....	64
5.1 TEST SYSTEM: RBTS-BUS2	64
5.1.1 Consumer Types and Load Modeling	65
5.1.2 Seasonal Effects	66
5.1.3 Load Profile.....	67
5.1.4 LP Tie-Sets and Reliability Data of RBTS-BUS2 Components.....	69
5.2 LP and System Reliability Indices without DGs (Base Case).....	71
5.3 LP and System Reliability Indices with System-Connected DGs	75
5.3.1 System With All DGs Including Battery (Case-1).....	76
5.3.2 System With All DGs Excluding The Battery (Case-2)	83
CHAPTER 6: CONCLUSION AND RECOMMENDATION.....	89
6.1 Conclusion.....	89
6.2 Recommendation	90
REFERENCES.....	91
VITAE.....	97

LIST OF TABLES

Table 3.1: CS6X-320P Datasheet and Model Parameter	32
Table 3.2: The Calculated 5-Parameters Values	32
Table 3.3: GE 1.5s Specification	34
Table 4.1: Tie Set of an Example LP	47
Table 4.2: Operations to Obtain the States of an LP	48
Table 5.1: Load Points Data and Consumers	66
Table 5.2: Northern Hemisphere Seasons, Dates and Hours	67
Table 5.3: Tie Set of LPs in RBTS-Bus2	70
Table 5.4: Reliability Data of RBTS-Bus2 Components	70
Table 5.5: Reliability Indices of All Load Points without DGs	74
Table 5.6: System Reliability Indices without DGs	74
Table 5.7: Variables and Objectives of the Best Compromise Solution (Case-1)	77
Table 5.8: Comparison of Objective Function Values at both Extremes	79
Table 5.9: Values of the Eight Particles with the Extreme Objective Functions	80
Table 5.10: Reliability Indices of All Load Points with DGs at BCS (Case-1)	82
Table 5.11: Variables and Objectives of the Best Compromise Solution (Case-2)	83
Table 5.12: Comparison of Objective Function Values at both Extremes (Case-2)	85
Table 5.13: Values of the Eight Particles with the Extreme Objective Functions (Case-2)	86
Table 5.14: Reliability Indices of All Load Points with DGs at BCS (Case-2)	88

LIST OF FIGURES

Figure 3.1: Equivalent Circuit of the 5-Parameter Model	20
Figure 3.2: I-V Characteristics of CS6X-320P Solar Panel at SRC and NOCT.....	33
Figure 3.3: A Month Power Output of Solar PV	33
Figure 3.4: Power Curve of GE 1.5s.....	35
Figure 3.5: General Curve of $C_p-\lambda$	35
Figure 3.6: A Month Power Output of the GE 1.5s Model.....	36
Figure 3.7: Wind Speed of a Month.....	36
Figure 3.8: Pitch Variation of a Month.....	37
Figure 3.9: Plot of Power Coefficient for a Month.....	37
Figure 3.10: Rotor Speed Variation for a Month.....	37
Figure 3.11: Combined Power Output of Wind Turbine and Solar PV DGs	38
Figure 3.12: Combined Output of Wind, Solar PV and Conventional DG.	39
Figure 3.13: A Day Power Output of a Solar PV Panel with 500Wh Battery Charging	40
Figure 4.1: Proposed Tie-Set Algorithm Flow Chart.....	43
Figure 4.2: Flow Chart for the Monte-Carlo Simulation Process	45
Figure 5.1: Single line diagram of RBTS-BUS2	64
Figure 5.2: Single Line Block Diagram of RBTS-Bus2	65
Figure 5.3: Residential Load Profile	68
Figure 5.4: Commercial Load Profile	68
Figure 5.5: Industrial Load Profile.....	69
Figure 5.6: Government/Institution Load Profile	69
Figure 5.7: Variation of Failure Frequency of all LPs.....	71

Figure 5.8: Variation of Repair Times of All LPs	72
Figure 5.9: Variation of Average Interruption Duration of All LPs	72
Figure 5.10: Variation of Energy Not Served of All LPs	73
Figure 5.11: Variation of System Reliability Indices without DGs.....	75
Figure 5.12: Plot of Four Dimensional Pareto Optimal Solutions (Case-1).....	77
Figure 5.13: Plot of SAIFI, SAIDI and Total Cost.....	78
Figure 5.14: Plot of SAIFI, ENS and Total Cost	78
Figure 5.15: Plot of SAIDI, ENS and Total Cost	79
Figure 5.16: Plot of Normalized Objective Values BCS and Extreme Particles (Case-1)	80
Figure 5.17: Comparison of SAIDI and SAIFI of Pareto Optimal Front with Base Case (Case-1).....	81
Figure 5.18: Comparison of Energy Not Served of Pareto Optimal Front with Base Case (Case-1).....	81
Figure 5.19: Plot of Four Dimensional Pareto Optimal Solutions (Case-2).....	83
Figure 5.20: Plot of SAIFI, SAIDI and Total Cost (Case-2)	84
Figure 5.21: Plot of SAIFI, ENS and Total Cost (Case-2)	84
Figure 5.22: Plot of SAIDI, ENS and Total Cost (Case-2).....	85
Figure 5.23: Plot of Normalized Objective Values BCS and Extreme Particles (Case-2)	86
Figure 5.24: Comparison of SAIDI and SAIFI of Pareto Optimal Front with Base Case (Case-2).....	87
Figure 5.25: Comparison of Energy Not Served of Pareto Optimal Front with Base Case (Case-2).....	87

LIST OF ABBREVIATIONS

SRC	:	Standard Rating Conditions
a	:	Ideality Factor Parameter
a_0	:	Ideality Factor Parameter at SRC
G	:	Total Solar Irradiance
G_0	:	Effective Irradiance at SRC (1000 W/m ²)
I_L	:	Light Current
I_{L0}	:	Light Current at SRC
I_{mp}	:	Current at Maximum Power Point
I_{mp0}	:	Current at Maximum Power Point at SRC
I_{sc}	:	Short Circuit Current
I_{sc0}	:	Short Circuit Current at SRC
I_o	:	Diode Reverse Saturation Current
I_{o0}	:	Diode Reverse Saturation Current at SRC
NOCT	:	Nominal Operating Cell Temperature
N_s	:	Number of Cells in Series on a Solar Panel
P_{mp}	:	Maximum Power
R_s	:	Series Resistance of the Solar PV Model
R_{s0}	:	Series Resistance of the Solar PV Model at SRC
R_p	:	Shunt Resistance of the Solar PV Model
R_{p0}	:	Shunt Resistance of the Solar PV Model at SRC
T_c	:	Cell Temperature

T_0	:	Cell Temperature at SRC (25° C)
T_{amb}	:	Ambient Temperature
V_{oc}	:	Open Circuit Voltage
V_{oc0}	:	Open Circuit Voltage at SRC
V_{mp}	:	Voltage at Maximum Power Point
V_{mp0}	:	Voltage at Maximum Power Point at SRC
β_T	:	Open Circuit Voltage Temperature Coefficient
E_g	:	Material Band Gap Energy
E_{g0}	:	Material Band Gap Energy at SRC
a_0, a_1, a_2, a_3, a_4	:	Coefficients for Air Mass Modifier Calculation
$b_0, b_1, b_2, b_3, b_4, b_5$:	Coefficients for Incidence Angle Modifier Calculation
AOI	:	Solar Angle of Incidence
C_0, C_1	:	Coefficients relating I_{mp} to Irradiance
C_2, C_3	:	Coefficients relating V_{mp} to Irradiance
C_4, C_5	:	Coefficients relating I_x to Irradiance
C_6, C_7	:	Coefficients relating I_{xx} to Irradiance
E_b	:	Beam Component of Irradiance on Module
E_{diff}	:	Diffuse Component of Irradiance on Module
E_e	:	Dimensionless Effective Irradiance
E_o	:	Irradiance at SRC (1000 W/m ²)
F_d	:	Fraction of Diffuse Irradiance used by Module
I_{TRW}	:	Current predicted using TRW Incorporated Equation
I_x	:	Current at $V = 0.5V_{oc}$

I_{x0}	:	Current at $V = 0.5V_{oc}$, at SRC
I_{xx}	:	Current at $V = 0.5(V_{mp} + V_{oc})$
I_{xx0}	:	Current at $V = 0.5(V_{mp} + V_{oc})$, at SRC
k	:	Boltzmann's constant (1.38066E-23 J/K)
n	:	Diode Factor for Each Cell in Module
q	:	Elementary Charge (1.60218E-19 Coulomb)
T_0	:	Cell temperature at SRC (25° C)
V_{mp0}	:	Voltage at Maximum Power Point at SRC
V_{oc}	:	Open Circuit Voltage
V_{oc0}	:	Open Circuit Voltage at SRC
α_{Imp}	:	Temperature Coefficient for I_{mp}
α_{Isc}	:	Temperature Coefficient for I_{sc}
β_{Vmp}	:	Temperature coefficient for V_{mp}
β_{Voc}	:	Temperature coefficient for V_{oc}
$\delta(T_c)$:	Thermal Voltage at Cell Temperature
V_w	:	Wind Velocity
$C_p(\lambda, \theta)$:	Power Coefficient of Wind Turbine
λ	:	Tip Speed Ratio
θ	:	Pitch Angle of the Wind Turbine
θ_f	:	Freezing Temperature of Battery Electrolyte
K_C, δ, ε	:	Battery Empirical Constants referring to Battery Capacity
SOC	:	State of Charge
DOC	:	Depth of Charge

Q_e	:	Battery's Quantity of Charge
τ_1	:	Time Constant
C_θ	:	Battery Thermal Capacitance
R_θ	:	Thermal Resistance between Battery and its Environment
θ_a	:	Ambient Temperature Surrounding the Battery
P_s	:	Source Thermal Power, i.e. Heat generated in the Battery
s	:	Variable of the Laplace Transform
$C(t)$:	Battery Capacity at Time, t.
$P_t^{B,c}$:	Battery Charging Power
$P_t^{B,d}$:	Battery Discharging Power
$P_t^{c,max}$:	Maximum Battery Charging Power
$P_t^{d,max}$:	Maximum Battery Discharging Power
$CF(P)$:	Cost Function of Thermal Generator producing Power, P.
i	:	Index for Interval Number
D	:	Duration of an Interval
h	:	Index for Hour of the Year
y	:	Index for the Year
MT	:	Mission Time.
C_{ihy}^x	:	State of component x at time division i, hour h and year y
T_{ihy}^w	:	State of Tie w at time division i, hour h and year y
S_{ihy}^z	:	State of Load Point z at time division i, hour h and year y
$MTTF$:	Mean Time to Failure
$MTTR$:	Mean Time to Repair

TUT_z	:	Total Uptime of Load Point z
TDT_z	:	Total Downtime of Load Point z
NF_z	:	Number of Failures of Load Point z
NPV	:	Net Present Value
SAIDI	:	System Average Interruption Duration Index
SAIFI	:	System Average Interruption Frequency Index
ENS	:	Energy Not Served
ICW	:	Total Investment Cost of Wind Turbines per KW
ICS	:	Total Investment Cost of Solar PV per KW
ICB	:	Total Investment Cost of Battery per KWh
ICD	:	Total Investment Cost of Conventional DG per KWh
P_W^R	:	Power Rating of Wind Turbine System
P_S^R	:	Power Rating of Solar PV Farm
C_B^R	:	Capacity Rating of Battery Energy Storage System
P_D^R	:	Power Rating of Conventional DG
iL	:	Islanded Loads
$iLNS$:	Islanded Loads Not Served
P_{ihy}^W	:	Power Output of Wind Turbine at Time Division i, Hour h and Year y
P_{ihy}^S	:	Power Output of Solar PV Farm at Time Division i, Hour h and Year y
P_{ihy}^B	:	Power Output of Battery at Time Division i, Hour h and Year y
P_{ihy}^T	:	Power Output of Conventional DG at Time Division i, Hour h and Year y
P_{ihy}^{iL}	:	Power Demand of Islanded Loads at Time Division i, Hour h and Year y

ABSTRACT

Full Name : Abass Afolabi Yahaya

Thesis Title : Optimal Design of Hybrid Renewable Energy System for Microgrid
Reliability Enhancement.

Major Field : Electrical Power

Date of Degree: May, 2016

The concept of microgrids, just like the renewable energy systems, is not entirely new, but not until recent decades did these technologies gain tremendous interests from researchers, utilities and governments. The world now clamours for renewable energy integration into the conventional electricity supply chain. However, setbacks challenge renewable sources and their integration. The uncontrollable intermittency of the sun irradiance and wind speed needed for solar photovoltaic and wind energy generation respectively have made these energy sources non-dispatchable. Hence, neither the conventional power grid nor the renewable sources are 100 percent reliable. This thesis, while acknowledging the reliability issues of these sources, intends to make-out possibilities for a hybridized microgrid system. In particular, the wind, battery and solar energy resources will be used in connection to the grid for improved energy supply reliability of several consumer types.

In analyzing the reliability performance of the hybrid renewable system, a new set of formulations for load points and system reliability indices are proposed. This method is based on a pseudo-digitization technique of recording system conditions over the mission time which aids analysis via counting procedures. A method of obtaining the tie-sets between sources and load points based on depth first search was also proposed. A four-objective optimization model is formed and solved via a mixed-integer multiple objective particle swarm optimization method for several cases. Long

term models of wind turbine, solar PV, battery and conventional DG are employed. Ten years of real life data of solar irradiance, wind speed, and temperature were used as inputs to the models. The method provides a viable means of improving several reliability indices of any distribution system with minimum cost implications for both installation and operation costs. The methods proposed and utilized can serve as a motivation for further digitization of electric power systems studies in general. In the sense that, formulations can be made compatible with the ways digital equipment view and utilize data.

ملخص الرسالة

الاسم الكامل : عباس أفولابي يحيى

عنوان الرسالة : التصميم الأمثل ل نظام هجين للطاقة المتجددة ل Microgrid الموثوقية التحسين.

التخصص : الطاقة الكهربائية

تاريخ الدرجة العلمية : مايو، 2016

مفهوم microgrids ، تماما مثل أنظمة الطاقة المتجددة ، ليست جديدة تماما ، ولكن ليس حتى لم العقود الأخيرة هذه التقنيات كسب مصالحي هائلة من الباحثين والمرافق والحكومات العالم الصخب الآن ل دمج الطاقة المتجددة في سلسلة إمدادات الكهرباء التقليدية . ومع ذلك ، والنكسات تتحدى مصادر الطاقة المتجددة و تكاملها . و التقطع لا يمكن السيطرة عليها من الإشعاع الشمس و سرعة الرياح اللازمة ل الضوئية وطاقة الرياح والطاقة الشمسية الجيل التالي جعلت هذه مصادر الطاقة غير إرسال قادرا . وبالتالي ، لا شبكة الكهرباء التقليدية ولا مصادر الطاقة المتجددة يمكن الاعتماد عليها بنسبة 100 في المئة . هذه الأطروحة ، مع الاعتراف القضايا الاعتمادية من هذه المصادر ، ينوي جعل التدريجي الاحتمالات عن نظام microgrid المهجنة . على وجه الخصوص ، سيتم استخدام طاقة الرياح ، وبطارية و موارد الطاقة الشمسية في اتصال الشبكة لتحسين موثوقية إمدادات الطاقة من عدة أنواع المستهلكين.

في تحليل أداء موثوقية النظام المتجددة الهجين ، يقترح مجموعة جديدة من مستحضرات للحصول على نقاط تحميل ومؤشرات اعتمادية النظام. ويستند هذا الأسلوب على تقنية الزائفة رقمنة تسجيل شروط النظام خلال وقت البعثة الذي يساعد تحليل عن طريق إجراءات الفرز. واقترح أيضا طريقة الحصول على مجموعات التعادل بين المصادر ونقاط التحميل حسب عمق البحث الأول. يتم تشكيل نموذج الأمثل أربعة موضوعي وحلها عن طريق مختلط صحيح متعددة موضوعي سرب الجسيمات الطريقة الأمثل للعديد من الحالات. ويعمل النماذج على المدى الطويل من توربين الرياح ، والطاقة الشمسية الكهروضوئية ، وبطارية والمديرية العامة التقليدية. استخدمت عشر سنوات من البيانات واقع الحياة من الإشعاع الشمسي وسرعة الرياح ، ودرجة الحرارة كمدخلات للنماذج. يوفر طريقة وسيلة ناجعة لتحسين مؤشرات عدة موثوقية أي نظام التوزيع مع التكاليف المترتبة على الحد الأدنى لتكاليف التركيب والتشغيل على حد سواء. الطرق المقترحة واستخدامها يمكن أن تكون بمثابة حافز لمزيد من رقمنة دراسات أنظمة الطاقة الكهربائية بشكل عام. بمعنى ، تركيبات يمكن أن تكون متوافقة مع طرق عرض المعدات الرقمية والاستفادة من البيانات.

CHAPTER 1

INTRODUCTION

The non-renewable nature of depleting fossil fuels, issues of climate changes, and calls for increased power quality and reliability, have provoked worldwide concerted efforts seeking solutions in distributed generations (DG), microgrids and the ultimate smart grid. The microgrid is at the center of this new scheme; it contains at least one DG and load, and also serves as building block for the smart grid [1]. Essentially, the microgrid is popularly termed as a consortium of energy generation resources, storage facilities and associated loads, together perceived as a single entity capable of power balancing function and, demand and supply resource management [1] [2]. The de-facto concept of microgrid is not entirely new. During Thomas Edison's era in the late nineteenth century, the power system was modular and generators were only installed at the distribution level before the support for centralized generation by state-regulated monopolies became rampant [3].

However, recent literatures reiterated that recent driving forces for the successful comeback of microgrid concept are breakthroughs in power electronics, solar photovoltaic (PV), wind turbines, micro-turbines, fuel cells, energy storage technologies and so on [1] [2] [4] [5]. The microgrid conceptualizes the connection of generation resources close to consumers on the low voltage grids, 460V class, supports the integration of diverse renewable and non-renewable energy sources, such as wind, solar energy and internal combustion engines. It also makes heat energy easily accessible through combined heat and power (CHP), i.e. cogeneration, which increases the thermal efficiency of generation plants to about 70% [6].

Several features of the microgrid scheme earns it several advantages over the hierarchical, unidirectional power flow convention of traditional power grid system. Microgrids are established at the power distribution system level either by reconfiguration of existing distribution system or newly built [4]. This proximity to loads precludes power losses hitherto incurred when power is transferred via longer transmission lines from centralized generations to distant loads. Efficiency is therefore improved. Microgrids can operate in two modes—grid-connected or standalone—and, any DG that is only grid-connected and cannot operate in the islanding mode is merely referred to as grid-tied DG [7] [8]. The microgrid islanding capability enables the microgrid to disconnect from the utility grid during times of disturbances or fault in the local grid. This increases the availability, reliability and power quality of electricity supply.

Through the capacity to integrate and operate only on renewable energy sources and use of storage facilities to smoothen generator responses, the microgrid can operate environmentally friendly power generation system, hence reducing carbon footprint and ameliorating the dangers of climate change. Furthermore, the microgrid architectures are either AC or DC bus types. These architectures and advanced power electronic technology facilitate the plug and play feature which is critical to the potentials of microgrids. The plug and play feature is what enables any types and numbers of electrical power energy sources to be connected to the same bus and feed loads in the same microgrid. Also, this feature eases the rigmarole of expansion planning, rather than the extensive transmission and distribution planning which takes years to accomplish and is very costly.

1.1 Thesis Motivation

Electricity is said to be a fresh commodity, that is, demand and supply must be balanced at all times with or without storage facility. Hence proper amount of generation facility must be

scheduled for the load at times. Usually, load demands are usually volatile and really never constant but generation can be ramped up and down to satisfy the load. This is the working condition of the conventional power system where all the generation facilities, majorly turbine-generator systems, are dispatch-able units. In the modern grid structure where several renewable energy resources are to be integrated, the luxury to dispatch units at will is lost. This is because most of the energy sources needed by these highly demanded renewable energy systems are uncontrollable, intermittent, and cannot be stored in a direct form. The solar radiation required by solar PV cells to generate direct current is dependent on time of the day, season of the year, and other arbitrary weather conditions. The wind gale needed by wind-turbine systems is intermittent and cannot be stored. Furthermore, the high heads of water falls cannot be solely claimed by hydro-turbine generation station because these water bodies usually serve other purposes such as irrigation, fishing and recreation. However, hydrogen and earth-crust heat required, respectively, by fuel cells and geothermal stations seems more readily available. But the fuel cells, geothermal, and other renewable energy technologies are not as researched and advanced as are the wind and solar energy systems technologies in recent years. One of such advancement in wind and solar systems technologies is the attainment of grid parity.

In a broader view, the intermittency of wind and solar energy is not necessarily a deficiency. These resources usually oscillate between being in excess and deficient in supply. Therefore, another function of the storage facilities is to store excess energy at times of abundance. Apparently, recent power system technologies support varieties of energy resources integrated into the system such as hydro-power and nuclear energy, wind and solar energy, fossil fuel, fuel cells, biomass, geothermal, micro-turbines and cogeneration. Power demands are typically cyclical and consist of daily peaks, weekly peaks and monthly peaks over the period of a week, month and year

respectively. Since some sources too are intermittent and unpredictable, these resources and loads must be synchronized and optimized in order that peak loads at all demand cycles are efficiently satisfied with minimum production and distribution costs, power losses, and maximum reliability. It is worthy of note that the configuration of such a system must be well chosen. The sizes of every installed generation capacity, the number of each type of unit to be installed, and where to be installed, are the parameters of each unit that must be determined in the optimization.

The above mentioned fleet of optimization is what is aimed at in this thesis. However, the types of DGs proposed for use in this work are mainly the solar-PV and wind energy systems, in addition to storage facilities and few conventional generators. The effects of the randomness of the wind gale and sun light on the electricity generation levels of wind-turbine and solar-PV energy systems are put into consideration. A microgrid system with maximized efficiency, reliability, and minimized cost and power losses is sought through multi-objectively optimized parameters of size, numbers of each type of DG and storage to be used, and where to be placed. The downtimes experienced by the different types of customers during failures are minimized through restorative measures.

1.2 Thesis Objectives

The main objectives of this thesis are given below.

1. To model the impact of renewable and non-renewable DG systems on the reliability of load points.
2. To analyze the effects of the location, type, size and numbers of generation units on the reliability of the microgrid system.

3. To develop an optimization model that minimizes the cost of investment and maximizes the reliability parameters of the load points and entire microgrid system.
4. To analyze the effects of energy storage on the reliability of the microgrid system.

1.3 Thesis Organization

In the second chapter, past works from the literature about the effects of wind and solar DGs on the quality and reliability of power systems. Several hitherto proposed methods and objective functions for the derivation of maximum reliability at minimal cost are presented. A chronicle of the most popular solar and wind DG models are also discussed. Several mathematical models of solar and wind DGs, battery energy storage system, and cost function of conventional diesel DG are given in the third chapter. In chapter four, a general tie-set algorithm, and a pseudo-digitization method of obtaining reliability indices of any system are proposed. The thesis formulated problems and methods of obtaining solutions, including the monte-carlo simulation and multi-objective particle swarm optimization, are presented. The RBTS-Bus2 test system and results of several system simulations based on the thesis problem formulations are presented and discussed in the fifth chapter. Finally, the last chapter contains statements of possible future works and conclusion paragraphs.

CHAPTER 2

LITERATURE REVIEW

2.1 Reliability Effects of Wind and Solar Energy on Microgrids

The sophisticated interconnection of the traditional grid system has both its advantages and disadvantages. This interconnection helps in several ways to supply power to distant consumers, make-up for loss of generation in a plant by other distant plants, reduces generation reserves, and hence, reduces generation cost and increases the system reliability. However, there is a limit to the reliability of the conventional power system based on its limited contingency design platform. This leads to some of the disadvantages when a contingency limit is reached or major events occur, such as natural disaster or accidents, a large number of customers are usually affected due to the massive interconnection of the feeders and inherent transfer of the effects of outages [9]. Obviously, the significance and importance of the microgrid concept and structure can help ameliorate these system failures.

The microgrid is an interconnection of a single type or varieties of microsources, storage systems, and loads that the macro-grid sees as single entity [10] [11]. Typically, the microsources, such as PV panels and wind generators (mostly <500KW) are situated at the load centers [10] [12] [13] [14]. The microgrid could be AC or DC microgrid and can operate in two modes; on-grid (non-autonomous), and islanded (autonomous) mode [15]. In on-grid mode, the microgrid is connected with the main grid. This enables it to deliver or receive power from the main grid or otherwise in accordance with the market policy [16]. Although microgrids are mostly sought to increase supply reliability during contingencies, microsources are slow in response and have little inertia which hampers their ability to immediately meet sudden rise in loads, hence, the need for storage

elements [17]. Storage systems, such as batteries, flywheels and super-capacitors, are used in microgrids to meet such unbalance between supply and load. This intervention is required as often as load fluctuates but for few seconds ($<100s$) with the requirements that the storage system has high charging and discharging rates in order to satisfy immediate response. The heart of the microgrid is an advanced power electronics interface that controls the disconnection, connection and exchange of power between the microgrid and macro-grid [18]. Both power wind mills and solar panels require power electronics and energy storage systems to smoothen their power outputs.

The sole purpose of reliability studies of power systems is to measure and reduce the frequency and duration of power system failures or interruptions. Interruptions have economic and social consequences for both the utilities providing power and the power consumers [19]. The cost of interruptions is usually huge based on the durations of the interruptions and types of customers interrupted. The more sensitive the loads interrupted, the higher the cost, therefore, industrial and commercial load interruptions are most costly [17] [19]. Venkataramanan et al [17] connoted that distributed generation be used for sensitive loads. Moreover, in present dispensation, the concept of microgrid shoulders the responsibility of improving the entire system reliability. Microgrids are closer to the consumers and allow easy expansion by the “plug and play” feature where a microsource can be added at any point without need for central system reconfiguration [12]. The distributed generation concept of the microgrid will facilitate localization of the effects of faults, maintain supply to local loads during faulty grid, and hereby, increase the reliability of the power system. However, it is widely indicated in literatures that the microgrid is to support the macro-grid rather than replacing it. In this thesis, solar panel and wind power supplies are used to support the main grid system in order to reduce the frequency and duration of interruptions. During

interruptions on the main grid, these renewable resources are expected to supply the loads. However, due to the unpredictable nature of wind and sun heat supply, these power sources are not hundred percent reliable and the need to be critically studied. In general, the aim of microgrids is to increase system reliability and questions of what if the solar and/or wind is not available during power failures come to mind. This is a probabilistic problem; however, reliable results are possible after extensive study and analysis of trends. The two sources are tested on residential, commercial and industrial loads. However, little research has been made on the reliability risks of going green [20].

2.2 DG Sizing and Placement to Improve Reliability

The distribution system conveys electricity from the distribution substation to consumer equipment. It's divided into primary and secondary distribution systems which are widely radial or partially meshed [21]. Due to this topology, failures in distribution system account for 80% of the interruptions experienced by customers [22] [23]. Also, it is claimed that distribution systems are accountable for 70% of the electrical power losses in power systems [24] and suggested the use of flexible D-STATCOM devices in reducing system power loss and improving voltage profile. In essence, the conventional distribution system is faced with power reliability issues and several methods have been researched in literatures for improvements. Rajaram et al [25] suggested continuous network reconfiguration of distribution systems, through switching of tie lines, in order for continuous operation at minimal loss and improve voltage profile. Also, Muller et al [26] proposed rebuilding of old systems using the Greenfield planning method to reduce operating cost and increase reliability. However, in general, most of the proposed solutions in the literature are broadly distribution automation (DA), smart restoration, and microgrid implementation.

Most solutions require the installation of distributed energy resources, including distributed generation (DG) and storage, as in the microgrid, while others call for additional control, two-way communication, advance metering and monitoring infrastructure in the distribution system for a self-healing system, as in the smart grid [27] [28]. As regards microgrid implementation, one or more DGs must be installed to improve reliability, and this also makes islanding possible. Furthermore, the location and size of the DGs must be optimized for an effectively optimum operation. Several works in the literature with different methodologies, but similar objectives, have been done. Bahram et al [29] proposed a new voltage stability index to optimally size and place DG to enhance voltage stability and reduce active power losses while considering load variations using the cuckoo search algorithm and imperialist competitive algorithm. Benvindo et al [30] proposed a model that simultaneously considers capacitor and DG placements and capacity to effect optimal system performance using a hybrid of tabu search and genetic algorithm (GA) techniques. Amir et al [31] used the traditional multi-objective PSO technique to optimize loss minimization, voltage profile improvement to optimally locate and size DGs in distribution system while considering the economical merits for both the operator and the utility.

Sevya et al [32] proposed an analytical solution method based on base case power flow and most beneficial location and size of DG considering both active and reactive power loss minimization. Hajar et al [33] suggested a multiple objective model in a fuzzy ant colony optimization hybrid method for location and sizing of PV array and DSTATCOM considering load balancing, voltage profile and loss minimization. Neeraj et al [34] proposed improved versions of PSO, GA and cat swarm optimization techniques for placing DGs and shunt capacitors for optimal reduction of losses. Wanxing et al [35] proposed an improved nondominated sorting genetic algorithm that deals with the familiar multi-objective power system problem of DGs sizing and location. Hegazy

et al [36] proposed the use of Big Bang-Big Crunch algorithm (BB-BC) for optimal location of pv-modeled DGs where the Big Bang is about the spread-out searching of solution space while the Big Crunch uses the idea of center of mass to converge all solution points and to choose the best solution. Komail et al [37] claim that using an improved harmony search algorithm for the optimal location and sizing of DG in a distribution system in multi-objective model of minimizing power loss and voltage deviations is effective. For the nearest future, when plug-in electric vehicles (PEV) become common, Kaiqiao et al have proposed coordination of PEV charging at appropriate times contingent on load profiles in order to preserve the reliability of future systems [38].

2.3 Models of the Solar and Wind DGs

Solar photovoltaic and wind energy have been tagged the two most important renewable energy sources after hydro energy in terms of their totally installed world capacities, research spending and attainment of grid parity [39]. In 2014, solar energy has reached grid parity in more than 19 countries while wind energy had earlier recorded such feats in most European countries. The solar and wind energy presently have more than 177GW and 336GW globally installed capacity respectively [39] [40]. Their applications ranges from power stations, transportation, water pumping, telecommunication and signaling, to satellite missions. Obviously, these technologies are very paramount and, hence, the importance of their mathematical modeling is high.

The solar PV performance and characteristics modeling, as well as wind energy, has received lots of attention in the literature. Luft et al proposed a simple explicit I-V characteristic equation, called TRW equation, for predicting the output of solar PV cells using manufacturer provided data [41] [42]. However, this model grossly overestimates solar PV outputs at several points. King et al used spectral data, empirically and directly measured parameters with manufacturer supplied data to predict the power output and five points on the I-V characteristics of any solar cell or module [43].

The five points are voltage current pairs at open circuit, short circuit, maximum power, mid of open circuit, and midway between maximum and open circuit points. The model is also known as Sandia Array Performance Model (SAPM) and it is used by some PV modeling software. The model has a good degree of accuracy but requires lots of not-easily-available input parameters and can only predict five points [42].

The commonly used solar PV model is called the 5-parameter model. The model comprises a parallel combination of an irradiance controlled current source, a diode, and a shunt resistor, all in series with a resistor. Once the 5-parameters are calculated, usually at reference conditions, the power output and I-V characteristics can be predicted for any temperature and irradiance. The parameters are output of the current source, the diode's reverse saturation current, series and shunt resistor values, and diode ideality factor. The 5-parameter model equation is inherently implicit. Several works and improvements have been done to the 5-parameter model. Hadj et al used classical data provided by manufacturers, and slopes at open and short circuit point to plot the output curve of the model [44]. However, curves at other conditions other than reference conditions are obtained by translation. Barker and Norton proposed a scheme that manipulates the combination of the SAPM, 5-parameter, and TRW equations [41]. It requires tuning of two parameters, series resistor and ideality factor, to fit the characteristics at the two non-classical points predicted by SAPM and uses TRW equation to avoid implicitness of the conventional 5-parameter equation. They claimed that the tuning process will compensate for the inconsistency of the TRW equation.

Desoto et al [42] proposed an improvement to the 5-parameter model by relating the temperature and irradiance dependence of the needed five parameters to the model. By ensuring that temperature coefficient of open circuit voltage is well accounted for, Desoto et al further achieved

an improvement of the model. The model requires only manufacturer provided data. Desoto et al model is used in solar PV modeling programs and shows better reliability and accuracy than all the earlier discussed models. Furthermore, Hongmei et al expanded Desoto et al's model to work for modules of cells, and arrays of series and/or parallel connected modules [45]. This model can also be used to study partial shading effects. The five parameter model is not entirely limited to a single diode model. Two, three or more multi diode models have been proposed in literature [46] [47]. These models are usually more complex with two additional parameters, diode reverse saturation current and ideality factor, for each diode added.

More so, the improvements sought after is either not guaranteed or insignificant despite increased complexity [47]. However, in 2015 Jing et al [48] proposed using generalized multidimensional diodes in solar PV models. The model uses $(n \times m)$ number of diodes; where n is the number of parallel branches and m is the number of series diodes per branch. This makes the model flexible and configurable for any type of PV cell technology. Jing et al claimed that both single and double diode model perform poorly at lower temperatures. The Jing et al model showed marked improvement and accuracy than the single and double diode models. However, the Jing et al model is more computationally extensive due to large number of parameters needed for modeling and the use of particle swarm optimization technique for parameter calculation.

Mathematical models give designers, manufacturers and researchers the chance to easily interact, predict, and vary several parameters and conditions of operations of any device without consequences. This can also be said of wind energy systems. The wind turbine system technology has received great attentions from researchers and sponsors within few decades. All subsections of the earlier wind turbine systems have been fully overhauled. Blades are now longer, towers are higher, individual blades can now be turned to improve efficiency and turbine protection at high

wind speed, and variable speed wind turbine systems are fast taking over from the conventional fixed speed systems. At an attempt to the increase the accuracy of wind turbine output model, Anderson and Bose paid a detailed attention to the aerodynamic modeling of several parts of a wind gust thereby complementing the works of Wasynczuk et al on the effects of wind fluctuations on the dynamic stability of power system [49] [50]. Wasynczuk et al [49] obtained a non-linear relationship between the power coefficient and both tip speed ratio and pitch angle using least squares best fit.

Initially, wind generating systems used synchronous generators directly connected to the grid. This system can only operate at constant speed, the synchronous speed, despite the high fluctuations of the wind. Hence the system was prone to frequent faults. Later on, cheaper and better performing induction machines replaced synchronous generators. But the system was still directly connected to the grid and tolerates only fixed speed operations. Recent achievements in the field of power electronics and advanced control principles have made the wind energy system more robust. Attention swiftly turned to electronic converter-assisted systems, such as the doubly-fed induction generator and full converter wind generating systems. These systems are variable speed tolerant, have higher performance, more flexibility, and can maintain rated output, however, they cost more. Several studies and improvements of these configurations have been proposed in literatures; stability analysis, wind forecasting, load modeling, grid integration requirements and issues, control methods and load flow analysis including wind power.

CHAPTER 3

SYSTEM MODELING

3.1 Solar DG Model

Several models have been developed to predict the I-V characteristics, power outputs, and performances of PV solar generators. These models work well for individual cells, modules of series and parallel connected cells, and arrays of interconnected modules. Most of these models utilize the Standard Reference Condition (SRC) or Standard Test Condition (STC) to calibrate the parameters needed to depict their models. SRC defines the ambient temperature of 25° Celsius, irradiance of 1000W/m² and air mass of 1.0 or 1.5 at which manufacturers usually provide solar PV model data.

3.1.1 Sandia Array Performance Model (SAPM)

This is also referred to as King's model. The SAPM method of modeling PV modules is to provide information for five different points for a predicted I-V characteristics curve. These points include the short circuit current (I_{sc}), maximum power point (MPP), open circuit voltage (V_{oc}), mid of V_{oc}, and midway between MPP and V_{oc}. SAPM provides information about the voltages and currents at these five points [43]. This model can translate the module data from the STC to any other utility conditions. The SAPM model is presented in equations (3.1)-(3.14).

$$I_{sc} = I_{sc0} f_1(AM_a) [1 + \alpha_{I_{sc}}(T_c - T_0)] \left[\frac{E_b f_2(AOI) + F_d E_{diff}}{E_0} \right] \quad (3.1)$$

$$I_{mp} = I_{mp0} [C_0 E_e + C_1 E_e^2] [1 + \alpha_{I_{mp}}(T_c - T_0)] \quad (3.2)$$

$$V_{mp} = V_{mp0} + C_2 N_s \delta(T_c) \ln(E_e) + C_3 N_s [\delta(T_c) \ln(E_e)]^2 + \beta_{V_{mp}}(E_e) \cdot (T_c - T_0) \quad (3.3)$$

$$V_{oc} = V_{oc0} + N_s \delta(T_c) \ln(E_e) + \beta_{V_{oc}}(E_e) \cdot (T_c - T_0) \quad (3.4)$$

$$I_x = I_{x0} [C_4 E_e + C_5 E_e^2] [1 + \alpha_{I_{sc}}(T_c - T_0)] \quad (3.5)$$

$$I_{xx} = I_{xx0} [C_6 E_e + C_7 E_e^2] [1 + \alpha_{I_{mp}}(T_c - T_0)] \quad (3.6)$$

$$P_{mp} = I_{mp} V_{mp} \quad (3.7)$$

$$FF = \frac{P_{mp}}{(V_{oc} \cdot I_{sc})} \quad (3.8)$$

Where:

$$E_e = \frac{I_{sc}}{I_{sc0} [1 + \alpha_{I_{sc}}(T_c - T_0)]} \quad (3.9)$$

$$\delta(T_c) = \frac{nk(T_c + 273.15)}{q} \quad (3.10)$$

$$f_1(AM_a) = a_0 + a_1 AM_a + a_2 (AM_a)^2 + a_3 (AM_a)^3 + a_4 (AM_a)^4 \quad (3.11)$$

$$f_2(AOI) = b_0 + b_1 (AOI) + b_2 (AOI)^2 + b_3 (AOI)^3 + b_4 (AOI)^4 + b_5 (AOI)^5 \quad (3.12)$$

$$\beta_{V_{oc}}(E_e) = \beta_{V_{oc0}} + m_{\beta_{V_{oc}}} (1 - E_e) \quad (3.13)$$

$$\beta_{V_{mp}}(E_e) = \beta_{V_{mp0}} + m_{\beta_{V_{mp}}} (1 - E_e) \quad (3.14)$$

Where AOI is solar angle of incidence, I_{mp} is current at maximum power point, I_{mp0} current at maximum power point at SRC, I_{sc} is short circuit current, V_{oc} is open circuit voltage, V_{oc0} is open circuit voltage at SRC, V_{mp} is voltage at maximum power point, V_{mp0} is voltage at maximum power point at SRC, I_x is current at $V = 0.5V_{oc}$, I_{x0} is current at $V = 0.5V_{oc}$, at SRC, I_{xx} is current at $V = 0.5(V_{mp} + V_{oc})$, I_{xx0} is current at $V = 0.5(V_{mp} + V_{oc})$, at SRC, $f_1(AM_a)$ is the polynomial

relating spectral influence on I_{sc} to AM_a , $f_2(AOI)$ is polynomial describing AOI influence on I_{sc} , T_c is cell temperature, T_0 is cell temperature at SRC (25° C), T_{amb} is ambient temperature, E_b is beam component of irradiance on module, E_{diff} is diffuse component of irradiance on module, E_e is dimensionless effective irradiance, F_d is fraction of diffuse irradiance used by module.

3.1.2 Luft et al's Model

Luft et al proposes an equation to predict all the points in the I-V characteristics of any PV module [41] [42]. This model is represented in equations (3.15)-(3.17). This work was carried out with the sponsorship of TRW Systems Group, hence, the TRW subscript in equation (3.15). An advantage of this model is the simplicity of its usage. On the other hand, inaccuracies such as over-estimation at several data points in Luft et al's model, were claimed by Hart and Raghuraman [41].

$$I_{TRW} = I_{sc} [1 - k_2 (e^{\frac{V}{V_{oc} k_1}} - 1)] \quad (3.15)$$

$$k_1 = \frac{\frac{V_{mp}}{V_{oc}} - 1}{\ln(1 - \frac{I_{mp}}{I_{sc}})} \quad (3.16)$$

$$k_2 = [1 - \frac{I_{mp}}{I_{sc}}] e^{\frac{-V_{mp}}{V_{oc} k_1}} \quad (3.17)$$

Where I_{TRW} is current predicted using TRW Incorporated equation, I_{mp} is current at maximum power point, I_{sc} is short circuit current, V_{oc} is open circuit voltage, V_{mp} is voltage at maximum power point.

3.1.3 Improvement of Luft et al's Model

Barker and Norton sought to use the strength of three different models (5-parameter, King's and Luft et al's models) to improve the PV performance model [41]. The original 5-parameter model is given in (3.18) while the improved model is given in equations (3.19)-(3.22). By using the points

predicted by the King's model, Barker and Norton manipulated the 5-parameter model to obtain a function for current output in terms of two of the five parameters, R_s and a , in a 5-parameter model. Solving for I_L in (3.18) by using the open-circuit voltage data point, $I = 0$ at $V = V_{oc}$, gives (3.19). Substituting (3.19) into (3.18) and solving for I_o considering the short-circuit data point, $I = I_{sc}$ at $V = 0$, gives (3.20). Also by slotting (3.19) and (3.20) into (3.18) and solving for R_p considering the MPP, $I = I_{mp}$ at $V = V_{mp}$, gives (3.21). These three equations, (3.19)-(3.21), are then slotted into (3.18) to obtain an implicit equation for I in terms of R_s and a . The implicit function is very cumbersome, hence, is not shown here. Barker and Norton realized using the implicit function did not give a steady result, so they replaced the I terms on the right hand side of the function with I_{TRW} as shown in (3.22).

$$I = I_L - I_o \left[e^{\frac{V+IR_s}{a}} - 1 \right] - \frac{V+IR_s}{R_p} \quad (3.18)$$

$$I_L = \frac{V_{oc}}{R_p} + I_o \left[e^{\frac{V_{oc}}{a}} - 1 \right] \quad (3.19)$$

$$I_o = \frac{I_{sc}R_p + I_{sc}R_s - V_{oc}}{R_p \left(e^{\frac{V_{oc}}{a}} - e^{\frac{I_{sc}R_s}{a}} \right)} \quad (3.20)$$

$$R_p = \frac{(I_{sc}R_s - V_{oc}) \left(e^{\frac{V_{oc}}{a}} - e^{\frac{V_{mp} + I_{mp}R_s}{a}} \right) + (V_{oc} - V_{mp} - I_{mp}R_s) \left(e^{\frac{V_{oc}}{a}} - e^{\frac{I_{sc}R_s}{a}} \right)}{I_{mp} \left(e^{\frac{V_{oc}}{a}} - e^{\frac{I_{sc}R_s}{a}} \right) + I_{sc} \left(e^{\frac{V_{mp} + I_{mp}R_s}{a}} - e^{\frac{V_{oc}}{a}} \right)} \quad (3.21)$$

$$I = I_L - I_o \left[e^{\frac{V+I_{TRW}R_s}{a}} - 1 \right] - \frac{V+I_{TRW}R_s}{R_p} \quad (3.22)$$

Where I is the current output of the solar PV model and V is the terminal voltage at the solar PV terminal, I_{TRW} is current predicted using TRW Incorporated equation, I_{mp} is current at maximum

power point, I_{sc} is short circuit current, V_{oc} is open circuit voltage, V_{mp} is voltage at maximum power point, a is ideality factor parameter, I_L is light current, I_o is diode reverse saturation current, R_s is series resistance of the Solar PV model and R_p is shunt resistance of the Solar PV model.

3.1.4 Hadj Arab et al Model

The Hadj Arab et al model proposed a method to predict the I-V characteristics of PV modules based on the analytical 5-parameter model. Once the five parameters, (I_L, I_o, m, R_s, R_p) , are known and plugged into the 5-parameter model, (3.23), the I-V characteristics can be graphed for a particular irradiance and cell temperature.

$$I = I_L - I_o \left[e^{\frac{V+IR_s}{mV_t}} - 1 \right] - \frac{V+IR_s}{R_p} \quad (3.23)$$

Where:

$$V_t = \frac{kT}{q} \quad (3.24)$$

Where V_t is thermal voltage, k is Boltzmann's constant, q Elementary Charge and m is ideality factor.

The needed five parameters are obtained through classical information associated with any PV module features, $(V_{oc}, I_{sc}, V_{mp}, I_{mp})$, and R_{s0} and R_{p0} defined in (3.25)-(3.26) respectively [44]. Equations (3.27)-(3.31) are used to calculate the five parameters at any particular irradiance and cell temperature. To graph the I-V characteristics of the module at other ambient conditions requires translation of the (I, V) points, usually at STC, to new points using equation (3.32)-(3.35) proposed by Chenlo et al [44]. The curve is translated without distortion of its shape.

$$\left(\frac{dV}{dI}\right)_{V=V_{oc}} = -R_{s0} \quad (3.25)$$

$$\left(\frac{dV}{dI}\right)_{I=I_{sc}} = -R_{p0} \quad (3.26)$$

$$R_p = R_{p0} \quad (3.27)$$

$$m = \frac{V_{mp} + I_{mp}R_{s0} - V_{oc}}{V_t \left[\ln\left(I_{sc} - \frac{V_{mp}}{R_p} - I_{mp}\right) - \ln\left(I_{sc} - \frac{V_{oc}}{R_p}\right) + \left(\frac{R_p I_{mp}}{I_{sc} R_p - V_{oc}}\right) \right]} \quad (3.28)$$

$$I_o = \left(I_{sc} - \frac{V_{oc}}{R_p}\right) e^{\frac{-V_{oc}}{mV_t}} \quad (3.29)$$

$$R_s = R_{s0} - \left(\frac{mV_t}{I_o}\right) e^{\frac{-V_{oc}}{mV_t}} \quad (3.30)$$

$$I_L = I_{sc} \left(1 + \frac{R_s}{R_p}\right) + I_o \left(e^{\frac{I_{sc} R_s}{mV_t}} - 1\right) \quad (3.31)$$

$$I_{sc2} = I_{sc1} \frac{G_2}{G_1} + \alpha(T_2 - T_1) \quad (3.32)$$

$$V_{oc2} = V_{oc1} + mV_t \ln\left(\frac{G_2}{G_1}\right) + \beta(T_2 - T_1) \quad (3.33)$$

$$I_2 = I_1 + (I_{sc2} - I_{sc1}) \quad (3.34)$$

$$V_2 = V_1 + (V_{oc2} - V_{oc1}) \quad (3.35)$$

Where R_{s0} is series resistance of the solar PV model at SRC, R_{p0} is shunt resistance of the solar PV model at SRC, α is short circuit current temperature coefficient, β is open circuit voltage temperature coefficient and G is total solar irradiance.

3.1.5 The 5-Parameter Model

Desoto et al's [42] improved the 5-parameter model and made the model compatible with minimal information for its characterization. The improved model requires data only from the manufacturer's datasheets of a solar PV panel for characterization. The panel current-voltage relationship is given in (3.36). Also, the equivalent circuit of the 5-parameter model depicting all the five parameters is shown in figure 3.1. Where the parameter a is given as $a = nKT N_s/q$.

$$I_A = I_L - I_o \left[e^{\frac{(V_A + I_A R_s)}{a}} - 1 \right] - \frac{V_A + I_A R_s}{R_p} \quad (3.36)$$

Where I_L is light current, I_o is diode reverse saturation current, R_s is series resistance of the Solar PV model and R_p is shunt resistance of the Solar PV model, a is ideality factor, and N_s is the number of solar cells in series.

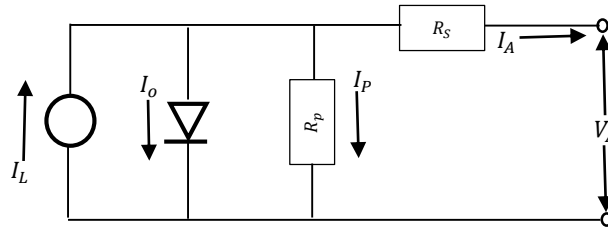


Figure 3.1: Equivalent Circuit of the 5-Parameter Model

As every other 5-parameter based model, once the five parameters (I_L, I_o, a, R_s, R_p) are calculated, usually at SRC, the I-V characteristics of the array at SRC can be obtained. To produce the I-V curve and P-V curve at any other temperature and irradiance, the parameters at that ambient condition must be obtained. Equations (3.37)-(3.42) show the relationships of the parameters at SRC to changes in operating conditions [51]. These equations are used to obtain the parameters at different temperature and irradiance, however, R_s does not change.

$$I_L = \left(\frac{G}{G_0}\right) [I_{L0} + \alpha_{I,sc}(T_c - T_{c0})] \quad (3.37)$$

$$I_o = I_{o0} \left(\frac{T_c}{T_{c0}}\right)^3 e^{\left[\frac{E_{g0}}{kT_{c0}} - \frac{E_g}{kT_c}\right]} \quad (3.38)$$

$$E_g = 1.17 - 4.73 \times 10^{-4} \left(\frac{T_c^2}{T_c + 636}\right) \quad (3.39)$$

$$\frac{R_p}{R_{p0}} = \frac{G_0}{G} \quad (3.40)$$

$$R_s = R_{s0} \quad (3.41)$$

$$\frac{a}{a_0} = \frac{T_c}{T_{c0}} \quad (3.42)$$

Where R_{s0} is series resistance of the solar PV model at SRC, R_{p0} is shunt resistance of the solar PV model at SRC, $\alpha_{I,sc}$ is short circuit current temperature coefficient, G is total solar irradiance, G_0 is total solar irradiance at SRC, I_{L0} is light current at SRC, I_{mp0} is current at maximum power point at SRC, I_{sc0} is short circuit current at SRC, I_{o0} is diode reverse saturation current at SRC, E_g is material band gap energy, and E_{g0} is material band gap energy at SRC.

To calculate the 5-parameters at reference conditions, equations (3.43)-(3.49) are used including information provided by the manufacturers. Equations (3.43)-(3.45) are based on the open circuit ($I_A = 0, V_A = V_{oc0}$), short circuit ($I_A = I_{sc0}, V_A = 0$), and MPP ($I_A = I_{mp0}, V_A = V_{mp0}$) respectively substituted into (3.36) at SRC. Equation (3.46) is based on the fact that the derivative of power at maximum power point is zero, $\frac{\partial P}{\partial V_{P=P_{max}}} = 0$. In order to properly account for temperature coefficient of open circuit voltage β_T , (3.47) is used. In (3.47) temperature is taken

within the range $T = T_{c0} \pm 10$. To evaluate V_{oc} at T , this open circuit condition is slotted into (3.36) to obtain (3.49). Then equations (3.37)-(3.39), giving the temperature dependencies of I_L and I_o , and (3.48) must be substituted into (3.49). Equations (3.43)-(3.46) and (3.49) are the five equations necessary to solve for the 5-parameters at SRC.

$$0 = I_{L0} - I_{o0} \left[e^{\frac{V_{oc0}}{a_0}} - 1 \right] - \frac{V_{oc0}}{R_{p0}} \quad (3.43)$$

$$I_{sc0} = I_{L0} - I_{o0} \left[e^{\frac{I_{sc0}R_{s0}}{a_0}} - 1 \right] - \frac{I_{sc0}R_{s0}}{R_{p0}} \quad (3.44)$$

$$I_{mp0} = I_{L0} - I_{o0} \left[e^{\frac{(V_{mp0} + I_{mp0}R_{s0})}{a_0}} - 1 \right] - \frac{V_{mp0} + I_{mp0}R_{s0}}{R_{p0}} \quad (3.45)$$

$$\frac{I_{mp0}}{V_{mp0}} = \frac{\frac{I_{o0}}{a_0} e^{\frac{(V_{mp0} + I_{mp0}R_{s0})}{a_0}} + \frac{1}{R_{p0}}}{1 + \frac{I_{o0}R_{s0}}{a_0} e^{\frac{(V_{mp0} + I_{mp0}R_{s0})}{a_0}} + \frac{R_{s0}}{R_{p0}}} \quad (3.46)$$

$$\beta_T = \frac{\partial V_{oc}}{\partial T} = \frac{V_{oc} - V_{oc0}}{T_c - T_{c0}} \quad (3.47)$$

$$V_{oc} = V_{oc0} + \beta_T (T_c - T_{c0}) \quad (3.48)$$

$$0 = I_L - I_o \left[e^{\frac{V_{oc}}{a}} - 1 \right] - \frac{V_{oc}}{R_p} \quad (3.49)$$

In order to obtain MPP voltage and current at any ambient conditions, equations (3.50) and (3.51) must be simultaneously solved. Equation (3.52) gives the cell temperature based on the ambient temperature, irradiance level and NOCT.

$$I_{mp} = I_L - I_o \left[e^{\frac{(V_{mp} + I_{mp}R_s)}{a}} - 1 \right] - \frac{V_{mp} + I_{mp}R_s}{R_p} \quad (3.50)$$

$$\frac{I_{mp}}{V_{mp}} = \frac{\frac{I_0}{a} e^{\frac{(V_{mp} + I_{mp} R_s)}{a}} + \frac{1}{R_p}}{1 + \frac{I_0 R_s}{a} e^{\frac{(V_{mp} + I_{mp} R_s)}{a}} + \frac{R_s}{R_p}} \quad (3.51)$$

$$T_c = T_{amb} + G \left(\frac{NOCT - 20}{0.8} \right) \quad (3.52)$$

Where T_{amb} is ambient temperature and NOCT is nominal operating cell temperature.

3.2 Wind DG Models

The theoretical physics of wind energy conversion via the mechanics of wind turbines to electrical power generation is well known. However, there are several issues with the model of practical wind turbines. This absence of standardized wind turbine models can be attributed to manufacturers' propriety claims, and the lack of sufficient data on how models work [52]. On the other hand, several efforts have been made to predict the working principles and output power of wind turbine systems. The power output models of wind turbines are characteristics of the wind parameters, the wind turbine rotor and blades features, and dynamics of atmospheric condition. The total power available in wind passing through an area A is given in (3.53).

$$P = 0.5\rho AV_w^3 \quad (3.53)$$

Where P is power in wind, ρ is air density, V_w is wind velocity.

But not all this power can be extracted. Betz has proven that the maximum power extractable from wind by a rotor of infinite number of blade is a 59.3%. This derating is accounted for by the parameter C_p , the power coefficient, which is defined as the ratio of the extracted power to total available wind power. Wind turbines with C_p of 0.5 have been claimed. The turbine power is given in (3.54). C_p is a function of tip speed ratio λ and pitch angle θ of the turbine rotor.

$$P_W = 0.5\rho AV_w^3 C_p(\lambda, \theta) \quad (3.54)$$

$$\lambda = \frac{\omega_r R}{V_w} \quad (3.55)$$

Where P_W is power extracted from wind, λ is tip speed ratio, C_p is power coefficient, R is length of turbine blade, and θ is pitch angle.

The relationship between C_p and (λ, θ) is not linear and several attempts have been made using numerical techniques and regression analysis to define $C_p(\lambda, \theta)$. Separate models have been used for constant speed and variable speed wind turbine system types. The most common models for constant speed turbine type are given in (3.56) and (3.58) [50] [53] [54]. For variable speed turbine applications, the models proposed in literature are given by (3.60)-(3.61) [53] [54] [55].

$$C_p(\lambda, \theta) = 0.5(\lambda_i - 0.022\theta^2 - 5.6)e^{-0.17\lambda_i} \quad (3.56)$$

$$C_p(\lambda, \theta) = 0.44\left(\frac{125}{\lambda_k} - 6.94\right)e^{\frac{16.5}{\lambda_k}} \quad (3.57)$$

Where:

$$\lambda_i = \frac{3600R}{1609\lambda} \quad (3.58)$$

$$\lambda_k = \frac{1}{\frac{1}{\lambda} + 0.002} \quad (3.59)$$

$$C_p(\lambda, \theta) = 0.73\left(\frac{151}{\lambda_i} - 0.58\theta - 0.002\theta^{2.14} - 13.2\right)e^{\frac{-18.4}{\lambda_i}} \quad (3.60)$$

$$C_p(\lambda, \theta) = C_1\left(\frac{C_2}{\theta} - C_3\beta\theta - C_4\theta^x - C_5\right)e^{\frac{-C_6}{\beta}} \quad (3.61)$$

Where:

$$\frac{1}{\lambda_i} = \frac{1}{\lambda - 0.02\theta} + \frac{0.003}{1 + \theta^3} \quad (3.62)$$

$$\frac{1}{\beta} = \frac{1}{\lambda + 0.08\theta} - \frac{0.035}{1 + \theta^3} \quad (3.63)$$

A common set of values for the constants of (3.61) are $C_1 = 0.5, C_2 = 116, C_3 = 0.4, C_4 = 0, C_5 = 5, C_6 = 21$, however, Manyonge et al [55] suggest the use of $C_4 = -0.5$.

These models usually perform well for almost all types of wind turbines because only insignificant differences exist among wind turbine models. The given $C_p(\lambda, \theta)$ relations are used to plot $C_p - \lambda$ curves to predict the best performance of turbine at several operational conditions. Mostly, the $C_p - \lambda$ curves are drawn for different values of wind speed while keeping the pitch angle θ constant. Hence, at any wind speed the best power performance coefficient C_p and pitch angle, in case of variable speed turbine, can be chosen along the locus of the MPPT as required.

3.3 Battery Energy Storage System

Energy storage systems have become more important in recent years mainly due to the need to make-up for the intermittency of renewable energy sources, to power hybrid electric vehicles, and for regulation purposes in power markets. Energy storage technologies include mechanical, such as the pumped hydro, compressed air energy storage (CAES) and fly wheel, electrical system, such as ultra-capacitors and super conducting magnetic coil, thermal, such as hot water and thermal fluid storage, and electrochemical storage systems [56]. The electrochemical storage technologies include secondary batteries, such as Lead-acid, sodium-sulphur, Nickel-Cadmium and lithium-ion, flow batteries, such as redox flow and hybrid flow, and chemical hydrogen, such as the electrolyzer

and fuel cell. Pumped hydro and CAES system have geographical limitations and are not modular in nature while batteries can be set-up almost anywhere and can be packed in modules. This makes batteries an ideal system for use with distributed generation facilities. However, not all battery technologies are commercially matured. The lead-acid battery is the most matured and commercially available battery with low cost.

Several mathematical and equivalent circuit models have been proposed for the use of electrical power researches in literature. Mathematical battery models such as the Shepherd, the Unnewehr Universal and the Nernst Models have been proven to be less accurate than equivalent circuit models due to advanced complexity in relating circuit parameters to battery physical states [57]. The most basic circuit model contains an ideal voltage source as its only component. The efficiency is usually considered 100% which is far from reality. A modification included an internal resistance element while an even more advanced modification considered the non-linearity between the voltage source and internal resistance via dependence on state of charge [58]. The Thevenin model includes additional capacitance-resistance parallel branch representing overvoltage and transient conditions. It takes into account the discharging process and the effects of stage of charge on internal resistance and open circuit voltage [58]. An improved resistive Thevenin battery model employs diodes in series with resistors to implement both charging and discharging regimes. This model is better than the former but cannot account for transients and elements are regarded constant.

A dynamic fourth order model having several branch elements representing ohmic effects, electrolytic reactions, energy or power loss and leakages in lead acid batteries have been popular in literature [59]. It is more accurate than aforementioned models, but it is more complex, requires lots of data, and longer computation time [59]. A less complex, yet accurate, model is the third

order model. It consists of two parts; main battery and the parasitic branch. The main branch represented the charging and discharging dynamics while the parasitic branch represented irreversible processes involved in power loss, such as during overcharge [60]. The third order model balances between complexity, accuracy and computation time. All the circuit parameters vary with the electrolyte temperature, state of charge and charging current. Also dynamic model of batteries obtained via manufacturer data have been used. In addition to the manufacturers data, several equations such as Peukerts equation for obtaining capacity in terms of discharging current, and relationships between internal resistance and discharge voltage to the state of charge [61].

3.3.1 Third Order Battery Dynamic Model

The third order model accounts for the effects of changes in electrolyte temperature, charging and discharging current, and state of charge (SOC). The model also considers the heat loss and non-thermal power losses, such as electrolysis of water, in the battery. Though third order model provides an electrical circuit equivalent of the lead acid batteries, its elements are not constant. The elements, including capacity, are functions of the discharging current, electrolyte temperature and SOC. The capacity of the battery systems as proposed by Massimo [60] is shown in (3.64). Equation (3.64) can be used when both current and temperature are considered constant and when they vary with transients. In the latter case, I is replaced with a filtered current value I_{avg} . Also $I_{avg} = I_1$ is proven to perform well in the model, while I_1 is defined in (3.65) and in a differential equation in (3.66). The quantity of charge derived out of the battery is defined in (3.67) while the SOC and depth of charge (DOC) are defined in (3.68)-(3.69). These formulae constitute the capacity model of the third order model.

$$C(I, \theta) = \frac{K_C C_{o*} \left(1 + \frac{\theta}{-\theta_f}\right)^\varepsilon}{1 + (K_C - 1) \left(\frac{I}{I^*}\right)^\delta} \quad (3.64)$$

$$I_1 = \frac{I_m}{1 + \tau_1 s} \quad (3.65)$$

$$\frac{dI_1}{dt} = \frac{I_m - I_1}{\tau_1} \quad (3.66)$$

$$Q_e(t) = Q_e(t_0) + \int_{t_0}^t -I_m(\tau) dt \quad (3.67)$$

$$SOC = 1 - \frac{Q_e(t)}{C(0, \theta)} \quad (3.68)$$

$$DOC = 1 - \frac{Q_e(t)}{C(I_{avg}, \theta)} \quad (3.69)$$

Where C is battery's capacity, C_{o*} is no-load capacity at 0°C, θ is electrolyte temperature, I is discharge current, I^* is nominal battery current, I_m is main branch current, Q_e is battery's charge, I_{avg} is mean discharge current, τ_1 is main branch time constant, SOC is state of charge, DOC is depth of charge, and K_C , δ and ε are empirical constants.

The temperature change of the electrolyte is represented in the third order model as thermal sub-model. The temperature of the electrolyte is assumed uniform, but it has only little effects on the accuracy of the model. The differential equation representing the thermal property in the model is given in (3.70). The parasitic current equation, a function of the parasitic branch voltage and electrolyte temperature, is given in (3.71). Also other parameters of the third order model are given in equations (3.72)-(3.76).

$$\frac{d\theta}{dt} = \frac{1}{C_\theta} \left(P_s - \frac{\theta - \theta_a}{R_\theta} \right) \quad (3.70)$$

$$I_p = V_{PN} G_{po} e^{\frac{V_{PN}}{V_{po} + A_p \left(\frac{1-\theta}{\theta_f} \right)}} \quad (3.71)$$

$$E_m = E_{mo} - K_E (273 + \theta) (1 - SOC) \quad (3.72)$$

$$R_1 = -R_{10} \ln(DOC) \quad (3.73)$$

$$\tau_1 = C_1 R_1 \quad (3.74)$$

$$R_0 = R_{00} [1 + A_o (1 - SOC)] \quad (3.75)$$

$$R_2 = R_{20} \frac{e^{A_{21}(1-SOC)}}{1 + e^{A_{22} \frac{I_m}{T^*}}} \quad (3.76)$$

Where C_θ is battery thermal capacitance, R_θ is battery thermal resistance, θ_a is ambient temperature, P_s is source thermal power loss, i.e. heat generated in the battery, V_{PN} is voltage at parasitic branch, I_p is current of parasitic branch, θ_f is electrolyte freezing temperature, E_m is open-circuit voltage, E_{mo} is open-circuit voltage at full charge, R_1 and R_2 are main branch resistances, R_0 is terminal resistance and G_{po} , V_{po} , A_p , R_{00} , R_{10} , R_{20} , A_{21} , A_{22} , A_o and K_E are constants.

3.3.2 A Simple Battery Model

A battery model which is easily compatible with long term planning of hybrid renewable energy systems, including wind and solar DGs, is considered. This model consists of charge and discharge equations as given in (3.77) and (3.78) respectively. The limits of the charging and discharging power rates are given in (3.79)-(3.80). The minimum and maximum level of energy stored in the

battery is represented in (3.81). The state of charge of the battery at any time is the ratio of the energy stored at the time and the capacity of the battery; this is shown in (3.82).

$$\text{Charging} : C(t + 1) = C(t) - \Delta t P_t^{B,c} \eta_c \quad (3.77)$$

$$\text{Discharging} : C(t + 1) = C(t) - \frac{\Delta t P_t^{B,d}}{\eta_d} \quad (3.78)$$

$$0 \leq P_t^{B,c} \leq P_t^{c,max} \quad (3.79)$$

$$0 \leq P_t^{B,d} \leq P_t^{d,max} \quad (3.80)$$

$$C(t)_{min} \leq C(t) \leq C(t)_{max} \quad (3.81)$$

$$SOC(t) = \frac{C(t)}{C(t)_{max}} \quad (3.82)$$

Where $C(t)$ is battery capacity at time, t , $P_t^{B,c}$ is battery charging power, $P_t^{B,d}$ is battery is charging power, $P_t^{c,max}$ is maximum battery charging power, and $P_t^{d,max}$ is maximum battery discharging power.

3.4 Conventional DG Model

The conventional power generation system uses non-renewable fuels, usually fossil fuel. The most popular of these systems are powered via diesel engines, gas turbines, steam turbines and more recently, micro-turbines. Unlike solar PV and wind DG renewable energy systems, these systems are dispatchable and their power outputs can easily be controlled and predicted. Generally, the control and operation of conventional power systems are well developed and reliable. However, the fossil fuels burned by these systems have created worldwide climate and environment hazards. These hazards are global warming, glacier melting, flooding, and climate changes. Conventional

DG systems incur operation costs as well as installation cost. The cost function is usually a function of the power generated by individual generator. A cubic cost function is given in equation (3.83). The power output of a generator is usually bounded by its limited power capacity, ramp rate and minimum up/down time. In this work, a diesel engine generating system is considered as the conventional DG.

$$CF(P) = A + BP + CP^2 + DP^3 \quad (3.83)$$

$CF(P)$ is cost function of thermal generator producing power, P and, $A, B, C,$ and D constants.

3.5 Modeling Output of the Power Sources on a Long-Term Basis

3.5.1 Solar PV Power Output

The solar PV outputs in this section are obtained via Desoto et al's model of solar PV cell as given in (3.36). The Canadian Solar Max Power CS6X-320P solar panel manufacturer data are used as to characterize the solar model. The required 5-parameters to characterize the solar panel were obtained via (3.43)-(3.49) and the MPP via (3.50)-(3.51). New 5-parameters at different operating points were obtained via (3.37)-(3.42) and cell temperature via (3.52). Table 3.1 compares the parameters obtained from the model with the manufacturer's datasheet [62]. Table 3.2 provides the 5-parameters obtained at SRC and at the NOCT. I-V characteristics of the panel at both SRC and NOCT are shown in figure 3.2. A month output of the solar-PV is shown in figure 3.3. The data used are raw data for the month of January 2014 in Oregon.

Table 3.1: CS6X-320P Datasheet and Model Parameter [62]

Operating Conditions	Parameters	320P Datasheet	Model
SRC 1000 W/m ² 25°C	P_{max} (W)	320	319.79
	V_{mpp} (V)	36.8	36.8
	I_{mpp} (A)	8.69	8.69
	V_{OC} (V)	45.3	45.3
	I_{SC} (A)	9.26	9.26
NOCT 800 W/m ² 47°C	P_{max} (W)	232	236.08
	V_{mpp} (V)	33.6	33.78
	I_{mpp} (A)	6.91	6.99
	V_{OC} (V)	41.6	42.21
	I_{SC} (A)	7.50	7.496

Table 3.2: The Calculated 5-Parameters Values

Operating	Parameters	Model
SRC 1000 W/m ² 25°C	i_L (A)	9.2713
	i_o (A)	5.7832×10^{-11}
	a	1.7569
	R_{sh} (ohm)	301.5768
	R_s (ohm)	0.3692
NOCT 800 W/m ² 47°C	i_L (A)	7.5034
	i_o (A)	1.7818×10^{-9}
	a	1.8865
	R_{sh} (ohm)	376.9710
	R_s (ohm)	0.3692

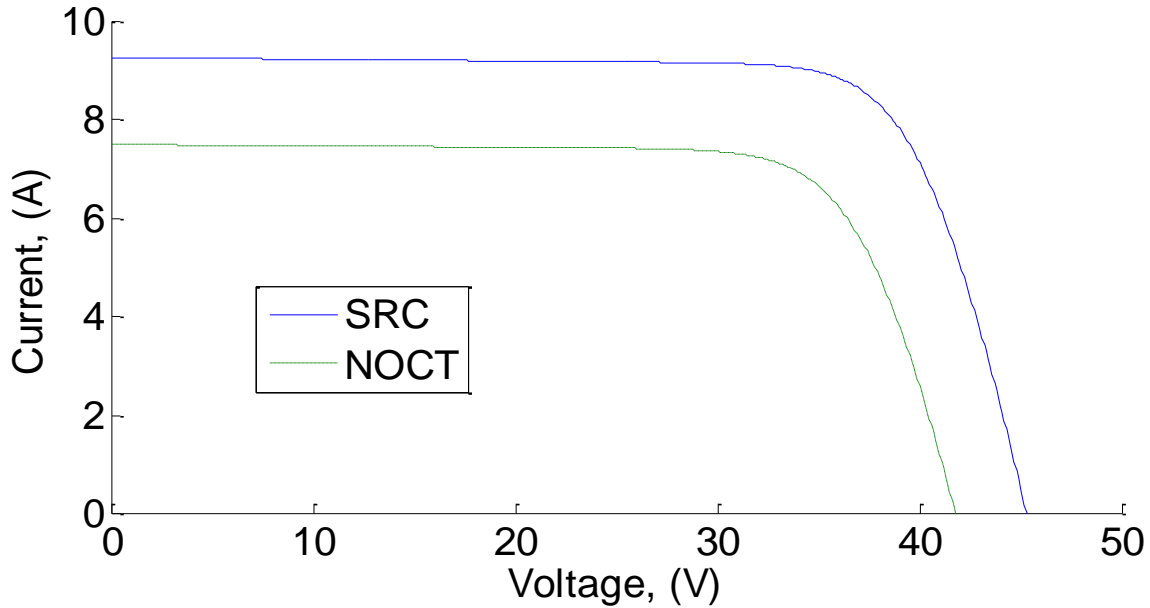


Figure 3.2: I-V Characteristics of CS6X-320P Solar Panel at SRC and NOCT

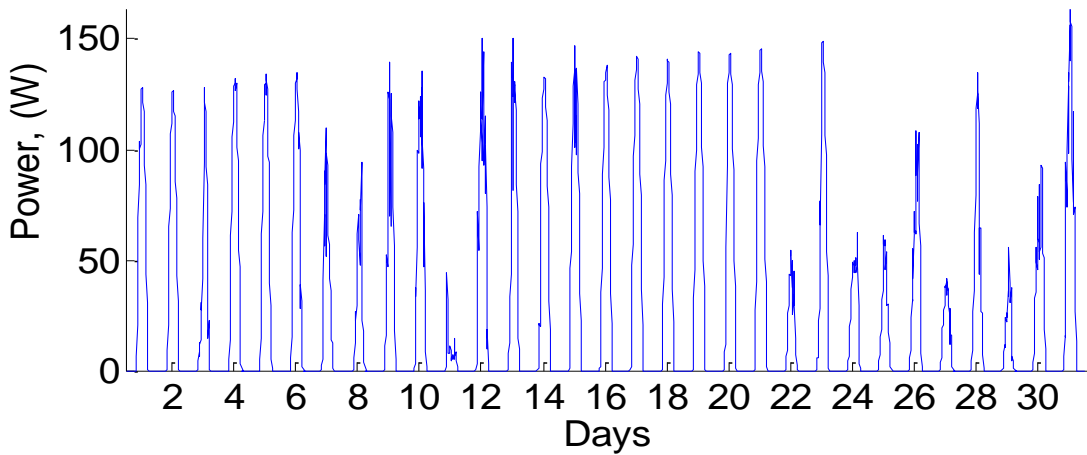


Figure 3.3: A Month Power Output of Solar PV

3.5.2 Wind Power Output

The wind turbine output is based on the models given by equations (3.54)-(3.55), (3.61) and (3.63). Hence, a variable speed wind turbine is implemented. The GE 1.5s wind turbine specifications given in Table 3.3 are used to verify the model. The power curve of the GE 1.5s is shown in figure 3.4. At wind speeds lesser than the cut-in speed the power out-put is zero, similarly, the power output at wind speeds higher than the cut-out speed is also zero. The latter is necessary to protect

the wind turbine from damage due to excessive wind gust. However, at wind speeds between the cut-in and rated speeds, a maximum power point algorithm is used to maximize the power output of the wind turbine. At every wind speed, the C_p - λ curve is drawn at several pitch angles. This enables the maximum value of C_p with corresponding values of pitch, λ , and rotor speed to be chosen. A sample C_p - λ curve is shown in figure 3.5.

At wind speeds above rated but below the cut-out speed, the pitch angle and C_p are chosen such that the rated power output and rated turbine rotor angular speed are maintained. By obtaining wind data for a month at a resolution of 10 minutes, the power output, wind speed data, pitch variation, C_p and rotor angular speed of the wind turbine are shown in the figures 3.6-3.10 respectively.

Table 3.3: GE 1.5s Specification [63]

Specification Parameters	Data Value
Rated Power	1.5MW
Rotor Diameter	70.5m
Area Swept	3904m ²
Minimum Rotor Speed	1.152 rad/s
Maximum Rotor Speed	2.304 rad/s
Rated Wind Speed	13m/s
Cut-in Wind Speed	4m/s
Cut-out Wind Speed	25m/s

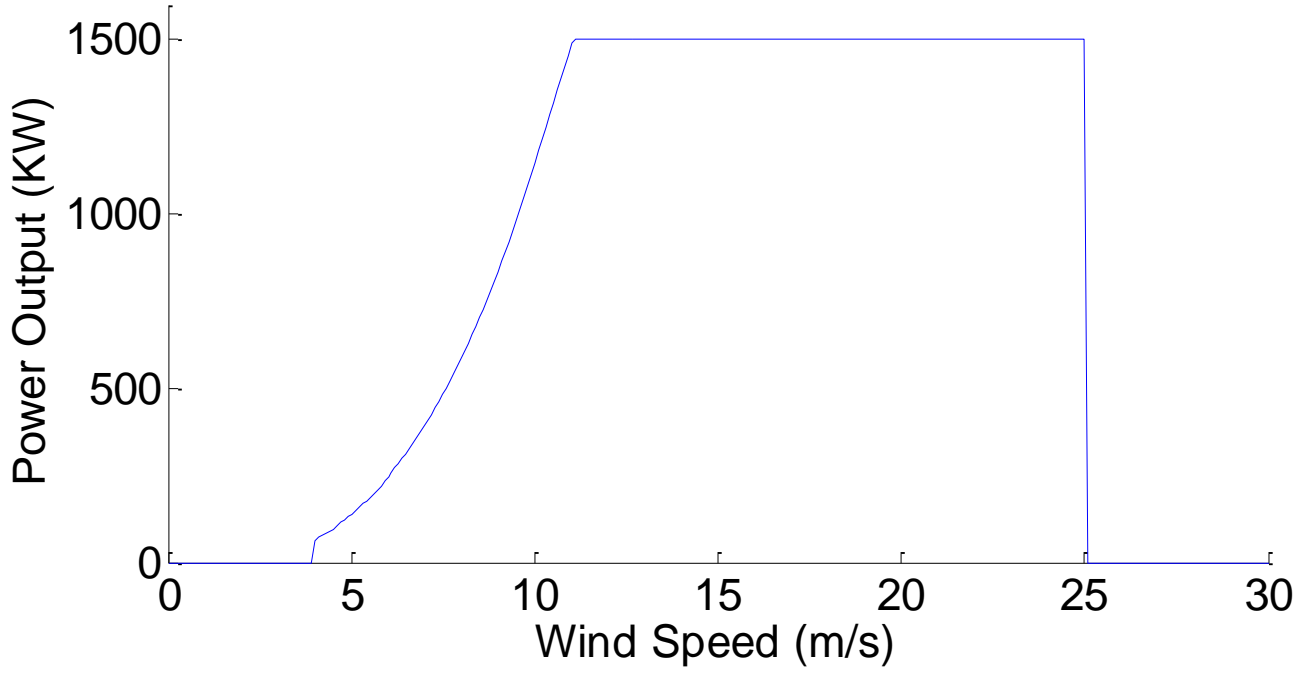


Figure 3.4: Power Curve of GE 1.5

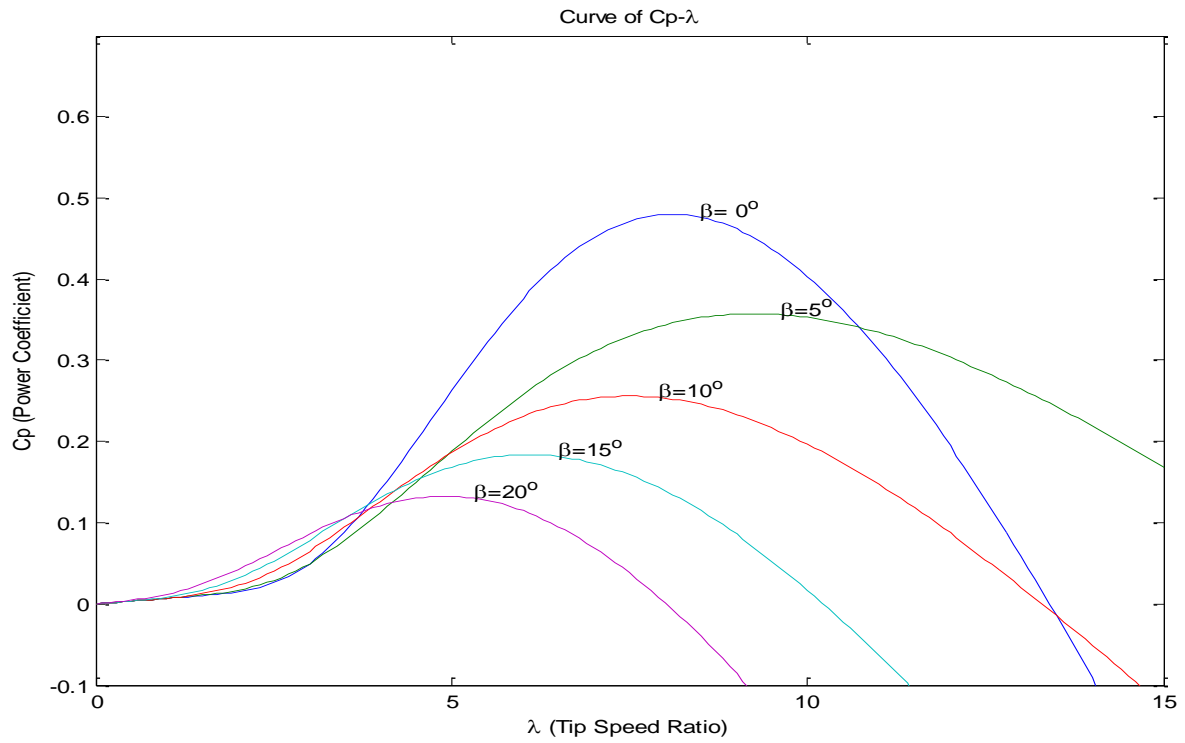


Figure 3.5: General Curve of Cp-λ

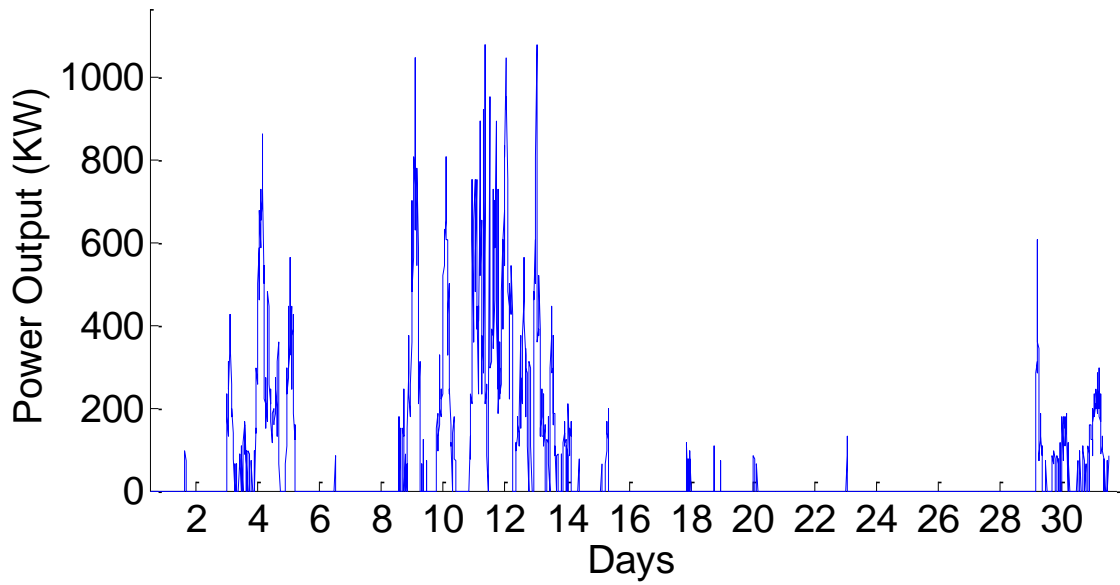


Figure 3.6: A Month Power Output of the GE 1.5s Model

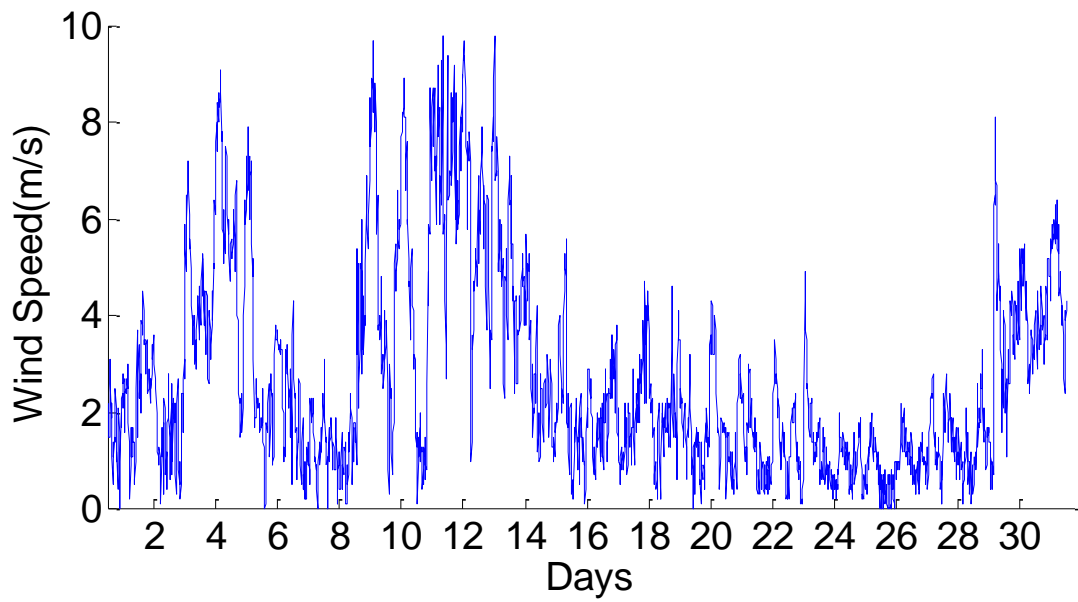


Figure 3.7: Wind Speed of a Month

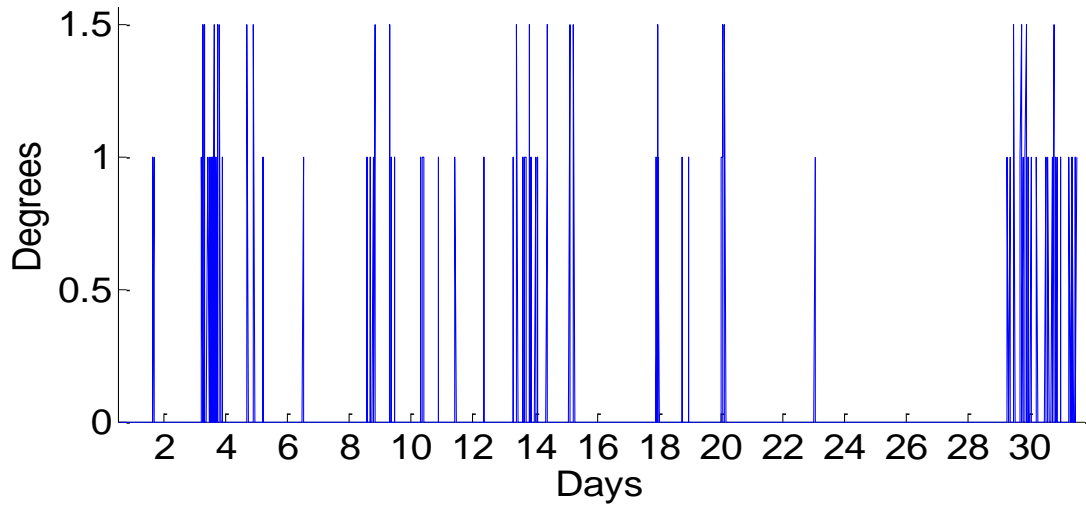


Figure 3.8: Pitch Variation of a Month

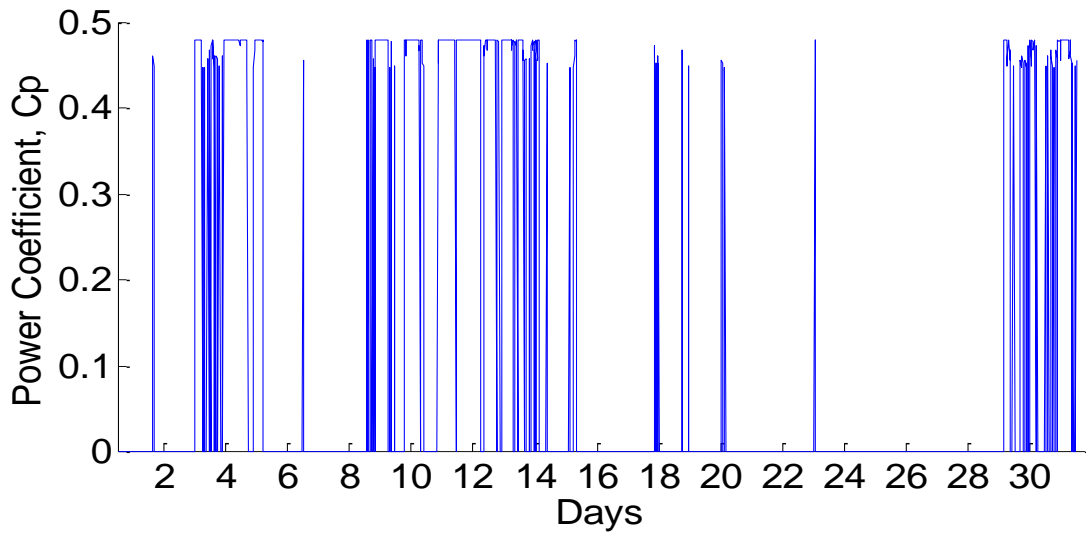


Figure 3.9: Plot of Power Coefficient for a Month

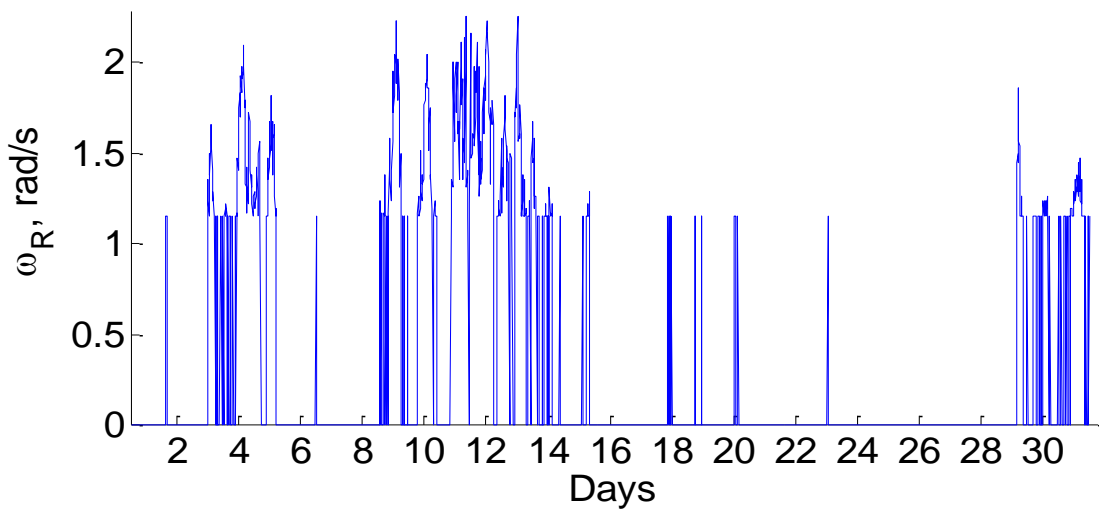


Figure 3.10: Rotor Speed Variation for a Month

3.5.3 Combined Wind Turbine and Solar PV Power Output

A combined power output of a solar PV farm and wind turbine is simulated and shown in figure 3.11 below. The number of solar panel is chosen such that the solar PV farm output is significant and not masked by the wind turbine output. The solar PV farm model consists of 6000 units of the CS6X-320P solar panel model. The graph of the individual and combined outputs is shown in figure 3.11.

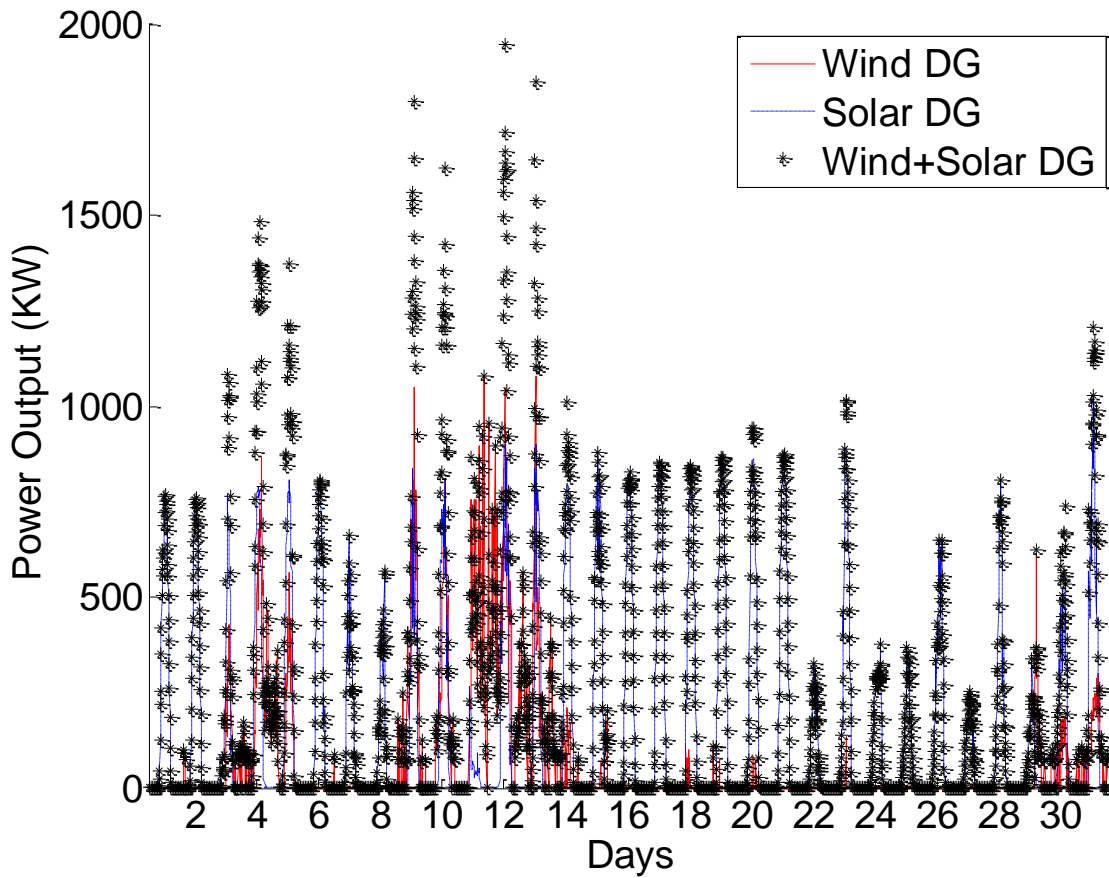


Figure 3.11: Combined Power Output of Wind Turbine and Solar PV DGs

3.5.4 Combined Wind Turbine, Solar PV and Conventional DG Power Output

A combined power output of the GE 1.5s wind turbine model, 6000 units of the CS6X-320P and the conventional diesel DG model given in (3.75). The coefficients and constant term in equation

(3.75) are taken as $A = 530$; $B = 6.89$; $C = 7.1 \times 10^{-4}$; $D = 7.32 \times 10^{-8}$. Equation (3.75) only computes the cost of generation. The study of the control mechanisms of generated power is not included in the scope of this work. The conventional DG is made to generate a constant 850 KW power output. The combined output curve is shown in figure 3.12.

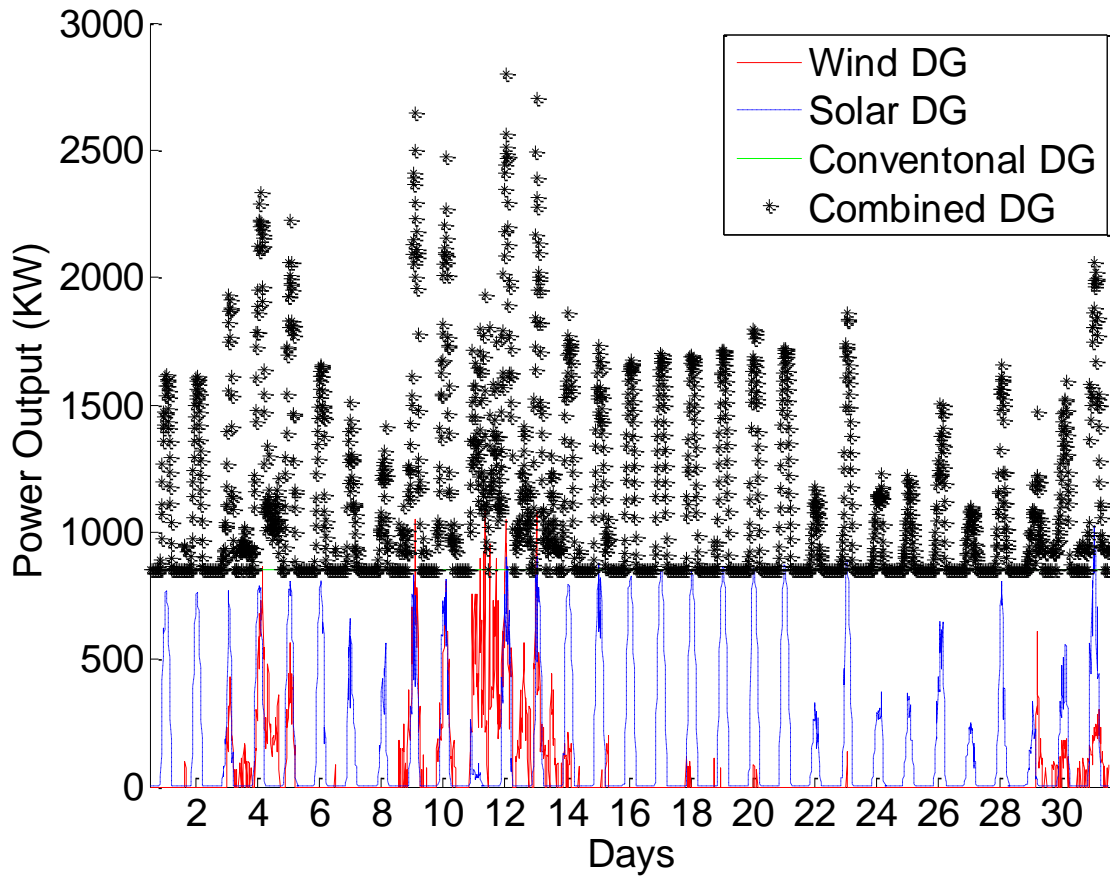


Figure 3.12: Combined Output of Wind, Solar PV and Conventional DG

3.5.5 Combined Solar PV Power and Energy Storage

A single CS6X-320P panel output is considered along with the energy storage system. The energy storage models given in (3.77)-(3.81) was used in a day charging session of the battery with the solar panel. The curves depicting available power output from the solar PV panel when the panel is acting alone, and when the panel charges a battery are shown in figure 3.13. Also, the pattern of

charging and energy storage of the battery system during the same period is given in figure 3.13.

The battery assumes a 500Wh capacity with a 100W charging and discharging power limits.

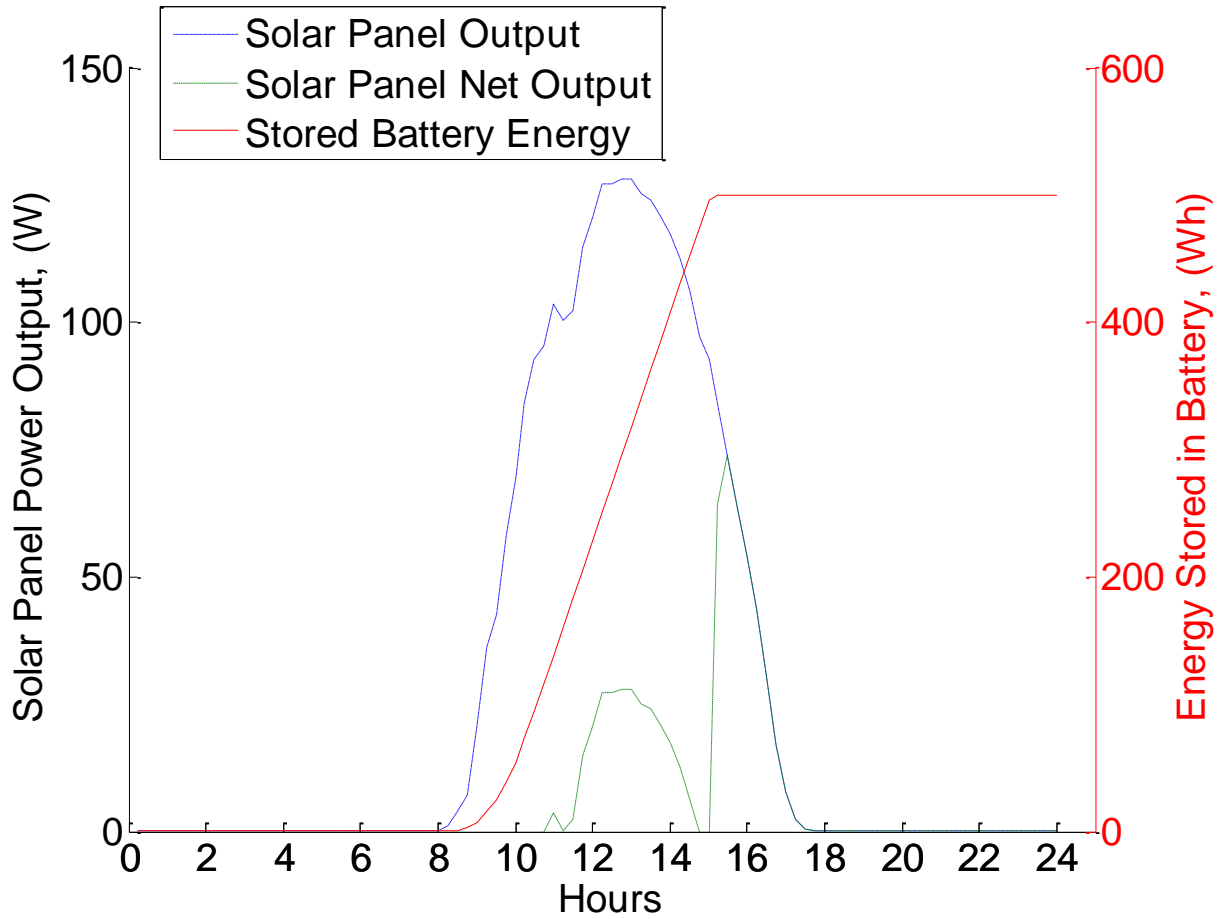


Figure 3.13: A Day Power Output of a Solar PV Panel with 500Wh Battery Charging

CHAPTER 4

PROBLEM FORMULATION AND METHODS

4.1 Proposed General Network Tie Set Algorithm

The tie set of any two nodes on a network consists of all possible minimal paths between the nodes. A minimal path consist of all paths traversed from an entry node to a particular target node without traversing any path and intermediary nodes more than once [64]. An up-state or good condition of all elements in any one path in the tie set assures connectivity between the nodes. Hence, all paths in a tie set are placed in parallel, such that reliability of the connection is a function of the union of the up-states of all the paths.

Figure 4.1 shows the flowchart of the proposed algorithm for the evaluation of all minimal paths in a distribution network. The algorithm uses an adapted form of the breadth first search (BFS) algorithm to search for all minimal paths and obtain the tie sets of every load point (LP). The algorithm can accommodate distribution networks with large number of source points (SP) and branches; either unidirectional, bidirectional or mixture of both in the same network. The algorithm searches for all ties by starting from the target LP and working out paths to all SPs. The inputs of the algorithm are all the input nodes or SP, output nodes or LP, and the predecessor table.

The elements of the proposed algorithm are briefly explained below:

1. Predecessor Table, $P(N_{out})$: The predecessors of any branch are other branches having the same receiving end node as the sending end node of that branch [65]. The predecessor table is unique for every target output node, N_{out} . $P(N_{out})$ contains the predecessors of all branches in the network such that the predecessors of any branch x_i , P_{x_i} , can be easily accessed. The steps required to obtain the predecessor table are well explained in [65].

2. Stack Box: This is used to facilitate the BFS algorithm and it works on a first-in first-out principle. This ensures that branches at the same depth are searched before moving to others. It is basically a row vector containing branches whose predecessors are yet to be exploited. A branch is deleted from the stack box after exploiting the predecessors and replacing it by them.
3. Route Table: The route table stores all viable possible paths and directions that the search could take. It also indicates the level of search the algorithm has reached through the last elements of all its rows. This last element is where the next search starts from. Once the route table supplies a route(s) to start a new search cycle based on the first element of the stack box, this route(s) is deleted from the route table. At the end of each search cycle, the route table may receive an updated version of the formerly deleted route(s) if the route(s) is not a dead end, does not lead to a cycle or a tie-set.
4. SubRoute: The subroute is the placeholder that stores the route(s) supplied by the route table at the beginning of every search cycle. The routes in subroute are chosen from the route table based on the fact that the first element of the stack box is the same as the last elements of those routes. Subroute is one of the two temporary stores which are initialized at every search cycle and deleted at the end.
5. SubRoute NC: This is the second temporary store of every cycle. It is used to specify the route(s) in SubRoute that pass the non-cyclical test. It also indicates routes which might be updated and returned to the route table as a viable route for future further exploitation.
6. Tie Set: This is a set of all ties or minimal paths between the target output node and all input nodes. The last element of all these ties is the input node or SP.

4.2 Monte-Carlo Simulation and Inverse Transform Method

There is always a level of uncertainty in the availability and operation of any element in a power system. This uncertainty is quantified with several reliability indices, such as the failure rate (λ), unavailability (U), and availability (A). Stochastic simulation approach, rather than the analytic method, is used to measure the reliability indices of the original system without DG and when reinforced with DG. Each component of the power system is assumed to either be in the up-state when it is not faulty or in down-state when in repair mode. The time-to-failure and time-to-repair of each component are taken as exponentially distributed. The exponential distribution is described in (4.1) and the time the system spends in any of the two states (t) is given by (4.2).

$$f(t) = \lambda e^{-\lambda t} \quad (4.1)$$

$$F(t) = 1 - e^{-\lambda t} \quad (4.2)$$

In general, λ is referred to as the rate of departure from a state; hence it can represent the failure rate and repair rate. $F(t)$ is the probability that the system will reside in a state for a period of time ($\leq t$) before going into another state. For the Monte-Carlo simulation (MCS), a random number generator is used in generating $F(t)$ and t is obtained through the inverse transform method (ITM) as given in (4.3).

$$t = -\frac{1}{\lambda} \ln(1 - F(t)) \quad (4.3)$$

When λ represents a failure rate, t is referred to as the mean-time-to-fail (MTTF) and mean-time-to-repair (MTTR) when λ represents the repair rate [64]. The flowchart depicting the several steps and processes involved in this use of Monte-Carlo simulation is drawn in figure 4.2. Repeated simulation sequences of operating–repair cycles are carried out till the mission time is reach. Via

counting and other enumeration processes, several reliability indices are calculated for every load point. The failure rate, availability (A) and unavailability (U) are given in (4.4) – (4.6).

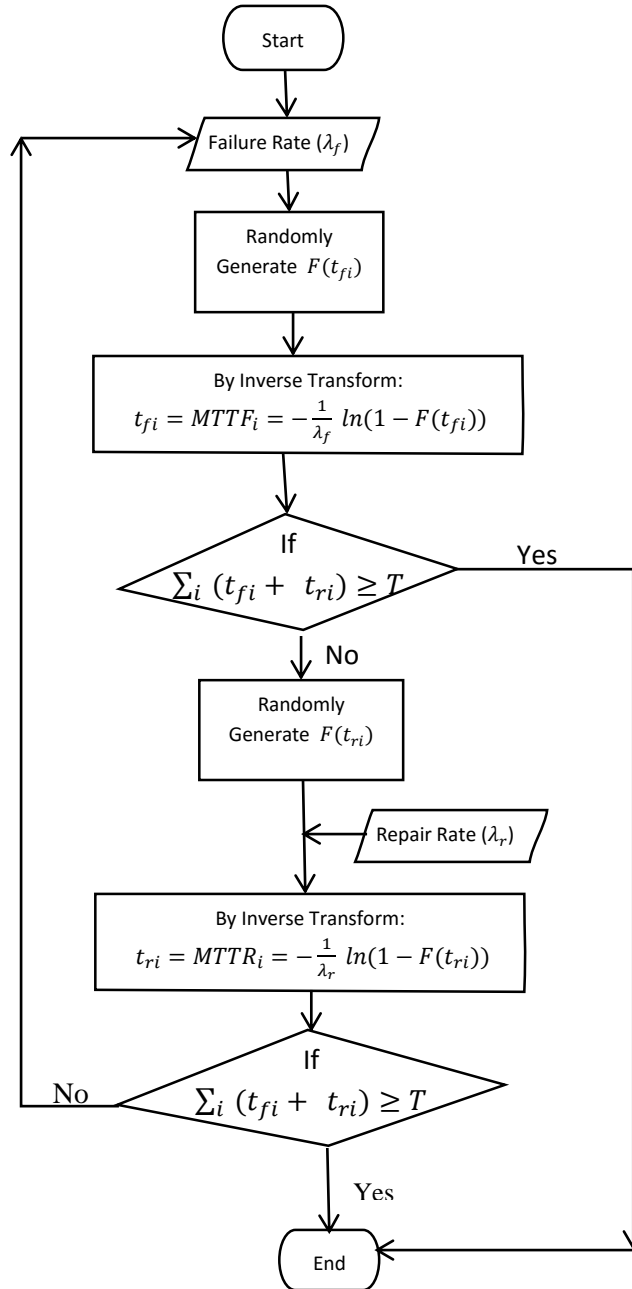


Figure 4.2: Flow Chart for the Monte-Carlo Simulation Process

$$\text{Failure Rate} = \frac{\text{number of failures}}{\text{total operational life simulated}} \quad (4.4)$$

$$\text{Availability} = \frac{\text{total uptime}}{\text{total operational life simulated}} \quad (4.5)$$

$$\text{Unavailability} = \frac{\text{total downtime}}{\text{total operational life simulated}} \quad (4.6)$$

In addition, the fact that the DG in operation does not meet the load does not mean the DG is totally down. This is referred to as a derated state of the DG. The effects of these derated outputs of DG are accounted for by the energy not supplied (ENS) index given in (4.7).

$$\text{ENS} = \sum_{\text{down time}} \text{load curtailed} \times \text{duration} \quad (4.7)$$

4.3 Proposed Method to Obtain Reliability Indices

The proposed method banks on a pseudo-digitization technique of representing the MTTF and MTTR obtained from MCS and ITM. Hence, the entire mission time of any component is represented by strings of ones and zeros at every time-division. In addition, the proposed method uses only simple operations, ‘logical and (\wedge)’ and ‘logical or (\vee)’ operations and basic arithmetic, to obtain the reliability indices of LPs and entire system. The method utilizes each component of the tie set of each LP to obtain each LP reliability indices.

After obtaining the tie set of each load point, the states of all components in each tie set over the entire period of observation is needed. A binary form of representing the states is chosen; ‘1’ for up state and ‘0’ for down state. The state of each component is updated or recorded every ‘D’ hour. The smaller ‘D’ is, the better is the accuracy of measurement. In this thesis, ‘D’ is limited by the time resolution of available wind speed, ambient temperature and solar radiation data, hence, $D = 0.25$ hrs. To conform to this, the results of the ITM algorithm, that are not multiples of D, are rounded up based on mid-interval points. To obtain the states of an LP, the states of each tie in the tie set of the LP need to be obtained. The state of each tie is the ‘and’ bitwise operation of the

states of its components, while the state of the entire tie set or an LP is the ‘or’ operation of all the ties in tie set of the LP. This operation is carried out per each time division, d. The ‘or’ operation gives the states of the LP. The entire operation is mathematically represented in equations (4.8)-(4.9). Via enumeration, the reliability indices of the LP can be obtained.

$$T_d^w = \bigwedge_{C^x \in T^w} C_d^x \quad \forall d \in \{1,2,3, \dots, N_d\} \quad (4.8)$$

$$S_d^z = \bigvee_{T^w \in S^z} T_d^w \quad \forall d \in \{1,2,3, \dots, N_d\} \quad (4.9)$$

Where C_d^x , T_d^w and S_d^z are the states of component ‘x’, tie ‘w’, and LP ‘z’ at time division ‘d’ respectively.

For instance, let the tie set of a hypothetical LP be as given in table 4.1. The tie set contains two paths between the LP and the SPs. The first tie, tie-1, has two components on its path while tie-2 has three components. The states of each component is obtained via ITM whereas the states of tie-1 and tie-2 are obtained from the ‘and’ operation of their respective components as shown in table 4.2. Table 4.2 shows a 3.50 hours window of the proposed procedure of obtaining the reliability at any LP via components’ states. The example has 14 time divisions ($N_d = 14$) with 15 minutes intervals, 5 components ($x = 5$) and 2 ties ($w = 2$) for a single LP ($z=1$). By using equations (4.8)-(4.9), the states of individual tie and the states of the entire LP is obtained at each time division as shown in table 4.2.

Table 4.1: Tie Set of an Example LP

Number of Ties	Components of the Tie Set
1	AB
2	CDE

Table 4.2: Operations to Obtain the States of an LP

Time(hr)	0.00	0.25	0.50	0.75	1.00	1.25	1.50	1.75	2.00	2.25	2.50	2.75	3.00	3.25	3.50
A	1	1	1	0	0	0	1	1	1	1	0	0	0	1	0
B	1	1	1	0	0	0	1	0	0	0	0	0	0	1	0
Tie-1	1	1	1	0	0	0	1	0	0	0	0	0	0	1	0
C	1	1	1	1	0	0	0	0	0	0	1	1	1	0	1
D	1	0	0	1	1	1	0	0	0	0	1	1	0	1	1
E	1	1	1	0	0	0	1	1	1	1	0	1	1	1	1
Tie-2	1	0	0	0	0	0	0	0	0	0	0	1	0	0	1
LP	1	1	1	0	0	0	1	0	0	0	0	1	0	1	1

From table 4.2, it is obvious that the example LP experiences 3 failures, has a total down time of 2.00 hours and a total uptime of 1.5 hours. The total mission time is 3.50 hours. The method is easily programmable, executes fast, and directly connects simulation results to their physical essence.

4.4 Problem Formulation

The objective function of this thesis is to increase the reliability of entire distribution system via proper placement and sizing of solar and wind DG, battery energy storage system and conventional diesel DG. The renewable DGs are used only during downtimes and the battery is discharged to support the renewable DGs, while the diesel is used when there is neither wind nor sunlight. The load point indices are needed to obtain the several system indices. The system indices are used to decide the performance of the entire system. The objective is to obtain the system with maximized system reliability indices and minimum cost of this reinforcement.

4.4.1 Load Point Reliability Indices

The load point (LP) indices are obtained via the analysis of the tie sets of each LP. Every component in the tie set is simulated via the ITM and MCS to obtain the state of each component

throughout the mission time (MT). The main quantities of counting are the states, either 1 or zero, of the component, tie-sets and LPs at any time. The process to obtain the LP states are illustrated in equations (4.8)-(4.9).

$$T_{ihy}^w = \bigwedge_{C^x \in T^w} C_{ihy}^x \quad \forall i, h, y \quad (4.8)$$

$$S_{ihy}^z = \bigvee_{T^w \in S^z} T_{ihy}^w \quad \forall i, h, y \quad (4.9)$$

Where: $i = 1, 2, 3, \dots, 1/D$; $h = 1, 2, 3, \dots, 8760$; $y = 1, 2, 3, \dots, MT$

Hence, ‘i’ is the index for interval number while ‘D’ is the duration, in hours, of each interval. ‘h’ is the index for the hour of the year, ‘y’ is the index for the year while ‘MT’ represents the planning horizon or mission time. Also C_{ihy}^x , T_{ihy}^w and S_{ihy}^z are the states of component ‘x’, tie ‘w’, and LP ‘z’ at time division ‘i’, at hour ‘h’ and year ‘y’ respectively.

After obtaining the states of an LP via (4.9), this states are further processed to obtain the reliability indices of the LP. The required procedures and proposed formulations are given below.

$$TUT = \sum_{y=1}^{nY} MTTF_y \quad (4.10)$$

But MTTF is defined in terms of LP state ‘S’, which is either ‘1’ or ‘0’, as given below.

$$MTTF = D \sum_{h=1}^{nH} \sum_{i=1}^{nD} S_{ihy}^z \quad (4.11)$$

Hence TUT (Total UpTime) of any LP can be expressed in terms of state is given in (4.12).

$$\text{TUT}_z = D \sum_{y=1}^{nY} \sum_{h=1}^{nH} \sum_{i=1}^{nD} S_{ihy}^z \quad \forall z \quad (4.12)$$

Similar to MTTF, the MTTR is obtained as given in (4.13), while TDT (Total Downtime) is given in (4.14). The number of failures (NF) experienced by an LP is given by equation (4.15).

$$\text{MTTR}_z = D \sum_{h=1}^{nH} \sum_{i=1}^{nD} (1 - S_{ihy}^z) \quad \forall z \quad (4.13)$$

$$\text{TDT}_z = D \sum_{y=1}^{nY} \sum_{h=1}^{nH} \sum_{i=1}^{nD} (1 - S_{ihy}^z) \quad \forall z \quad (4.14)$$

$$\text{NF}_z = \left\lfloor \frac{\sum_{y=1}^{nY} \sum_{h=1}^{nH} \sum_{i=1}^{nD} |S_{ihy}^z - S_{(i-1)hy}^z|}{2} \right\rfloor \quad \forall z \quad (4.15)$$

$$\text{Repair Time, } r_z = \frac{\text{TDT}_z}{\text{NF}_z} \quad \forall z \quad (4.16)$$

$$\text{Failure Frequency, } \lambda_z = \frac{\text{NF}_z}{\text{TUT}_z} \quad \forall z \quad (4.17)$$

$$\text{Availability, } A_z = \frac{\text{TUT}_z}{\text{TUT}_z + \text{TDT}_z} = \frac{\text{TUT}_z}{nY \times 8760} \quad \forall z \quad (4.18)$$

$$\text{Unavailability, } U_z = \frac{\text{TDT}_z}{\text{TUT}_z + \text{TDT}_z} = \frac{\text{TDT}_z}{nY \times 8760} \quad \forall z \quad (4.19)$$

$$\text{Annual Unavailability, } U_{a,z} = \lambda_z r_z = \frac{\text{TDT}_z}{\text{TUT}_z} \quad \forall z \quad (4.20)$$

$$\text{ENS}_z = D \sum_{y=1}^{nY} \sum_{h=1}^{nH} \sum_{i=1}^{nD} \text{PD}_{ihy} (1 - S_{ihy}^z) \quad \forall z \quad (4.21)$$

TUT_z is the sum of all the uptime sessions encountered by the LP, z , while TDT_z is the sum of the entire downtimes seen by the same LP, as presented in (4.10) - (4.14). NF_z , in (4.15) is given by the ceil operation of half of the number of times the LP changes state; from up to down state and vice-versa. The energy not served (ENS) at any LP is the sum of all the energy not met at the LP of concern is given (4.21).

4.4.2 System Reliability Indices

The LP indices are used to obtain the entire system indices in order to study the performance of the entire system as a single unit. These indices are either duration based, frequency based or energy based. The considered indices are:

1. System Average Interruption Duration Index (SAIDI)
2. Customer Average Interruption Duration Index (CAIDI)
3. System Average Interruption Frequency Index (SAIFI)
4. Energy not Served (ENS)

$$SAIDI = \frac{\sum_{z=1}^{nLP} U_{a,z} N_z}{\sum_{z=1}^{nLP} N_z} \quad (4.22)$$

$$CAIDI = \frac{\sum_{z=1}^{nLP} U_{a,z} N_z}{\sum_{z=1}^{nLP} \lambda_z N_z} \quad (4.23)$$

$$SAIFI = \frac{\sum_{z=1}^{nLP} \lambda_z N_z}{\sum_{z=1}^{nLP} N_z} \quad (4.24)$$

$$ENS = \sum_{z=1}^{nLP} ENS_z \quad (4.25)$$

4.4.3 Objective Functions and Constraints

The objectives of this thesis aim at optimizing both the cost of system reinforcement and the level of reliability obtained via the reinforcement. To calculate the total cost of system reinforcement, the total operational cost over the planning horizon must be estimated. The total operational cost (TOC) for 'nR' runs of the 'nY' simulation years is given in (4.26). The average annual operating cost (AAOC) and net present value for the planning horizon (PH) are given in (4.27) and (4.28) respectively.

$$TOC = \sum_{r=1}^{nR} \left(\sum_{y=0}^{nY} \sum_{h=0}^{nH} \sum_{d=1}^{nD} CF(P_{yhd}^T) \right) \quad (4.26)$$

$$AAOC = \frac{TOC}{nR * nY} \quad (4.27)$$

$$NPV = \sum_{m=1}^{PH} \frac{AAOC}{(1 + ir)^{m-0.5}} \quad (4.28)$$

Hence, the proposed objectives are given below in (4.29)-(4.32).

$$1. \text{ Minimize: } F(\text{Duration Index}) = \sum_{r=1}^{nR} \frac{SAIDI_r}{nR} \quad (4.29)$$

$$2. \text{ Minimize: } F(\text{Frequency Index}) = \sum_{r=1}^{nR} \frac{SAIFI_r}{nR} \quad (4.30)$$

$$3. \text{ Minimize: } F(\text{Energy Index}) = \sum_{r=1}^{nR} \frac{ENS_r}{nR} \quad (4.31)$$

$$4. \text{ Minimize: } F(\text{Cost}) = ICW \cdot P_W^R + ICS \cdot P_S^R + ICB \cdot C_B^R + ICD \cdot P_D^R + NPV \quad (4.32)$$

Where ICW, ICS, ICD and ICB are total investment cost of wind turbine, solar PV, battery and conventional DG, P_w^R , P_S^R , C_B^R , P_D^R are power rating of wind turbine system, solar PV farm, capacity rating of battery energy storage system, and power rating of conventional DG, and ir is interest rate.

The duration and frequency of interruption based reliability indices are represented in (4.29) and (4.30) respectively. The energy not served index is given in (4.31). Due to the stochastic nature of the MCS and ITM used, average values of these indices are sought over a repeated simulation cycle of ‘nR’ times. The one-time investment costs of all required DGs are summed and given in (4.32), with the last term representing the operational cost of the thermal DG.

The objectives are subject to several microgrid and individual unit constraints. Since the DG units are used only during islanding, equation (4.33) guarantees islanded loads (iL) -DGs output balance.

$$P_{ihy}^w + P_{ihy}^S + P_{ihy}^B + P_{ihy}^T + P_{ihy}^{iLNS} = P_{ihy}^{iL} \quad \forall i, h, y \quad (4.33)$$

$$0 \leq P_{ihy}^{iLNS} \leq P_{ihy}^{iL} \quad \forall i, h, y \quad (4.34)$$

$$P_{ihy}^B = \begin{cases} > 0 & P_{ihy}^w + P_{ihy}^S < P_{ihy}^{iL} \text{ and } C(t) > C_{min} \\ < 0 & P_{ihy}^w + P_{ihy}^S > P_{ihy}^{iL} \text{ and } C_{min} < C(t) < C_{max} \\ 0 & P_{ihy}^w + P_{ihy}^S = P_{ihy}^{iL} \end{cases} \quad (4.35)$$

$$P_{ihy}^T = \begin{cases} P_{ihy}^T & P_{ihy}^w + P_{ihy}^S + P_{ihy}^B < P_{ihy}^{iL} \\ 0 & \text{otherwise} \end{cases} \quad (4.36)$$

$$P_{ihy}^B \leq |P_{ihy}^{iL} - (P_{ihy}^w + P_{ihy}^S)| \quad \forall i, h, y \quad (4.37)$$

$$P_{ihy}^T \leq P_{ihy}^{iL} - (P_{ihy}^w + P_{ihy}^S + P_{ihy}^B) \quad \forall i, h, y \quad (4.38)$$

Where P_{ihy}^w , P_{ihy}^S , P_{ihy}^B and P_{ihy}^T represent power output of wind turbine, solar PV farm, battery and conventional DG at time division i , hour h and year y , and P_{ihy}^{iL} and P_{ihy}^{iLNS} are power demand of islanded loads and islanded loads not served at time division i , hour h and year y .

Limits on the island loads not served ($iLNS$) is maintained via (4.34). Equation (4.35) shows that the battery power is positive when discharging, negative when charging and zero otherwise. It also enforces that the battery charges only when the wind and solar DGs have excess power while the battery is not fully charged, and to discharge only when wind and solar DGs output are deficient. The thermal generator is required only when the sum of wind and solar DGs, and battery outputs do not balance islanded loads (4.36). However, the outputs of both the battery and thermal engine must only be as much as necessary not to cause imbalance in the system, equations (4.37) and (4.38) ensure this effects.

Each DG has a size limit constraint. These constraints are given in (4.39)-(4.42) below.

$$P_{w,min}^R \leq P_w^R \quad (4.39)$$

$$P_{S,min}^R \leq P_S^R \quad (4.40)$$

$$C_{B,min}^R \leq C_B^R \quad (4.41)$$

$$P_{T,min}^R \leq P_T^R \quad (4.42)$$

Hence, the output of each DG is limited by its rated size. These power output constraint is given below (4.43)-(4.45).

$$0 \leq P_{ihy}^w \leq P_w^R \quad \forall i, h, y \quad (4.43)$$

$$0 \leq P_{ihy}^S \leq P_S^R \quad \forall i, h, y \quad (4.44)$$

$$0 \leq P_{ihy}^T \leq P_T^R \quad \forall i, h, y \quad (4.45)$$

The charging and discharging equations of the battery are given in (4.46)-(4.47). The battery can be charged only via the renewable DG has given by (4.35).

$$\text{Charging : } C_{(i+1)hy}^B = C_{ihy}^B - \Delta d \eta_c P_{ihy}^B \quad \forall i, h, y \quad (4.46)$$

$$\text{Discharging : } C_{(i+1)hy}^B = C_{ihy}^B - \frac{\Delta d P_{ihy}^B}{\eta_d} \quad \forall i, h, y \quad (4.47)$$

$$C_{ihy,min}^B \leq C_{ihy}^B \leq C_{ihy,max}^B = C_B^R \quad \forall i, h, y \quad (4.48)$$

$$-P_{ihy,max}^B \leq P_{ihy}^B \leq P_{ihy,max}^B \quad \forall i, h, y \quad (4.49)$$

To limit the charging of the battery to its rated capacity value and discharge to a minimum state to charge enough to preserve battery life, equation (4.48) is deployed. The power output of the battery (P_{ihy}^B) is limited to within safe boundaries with (4.49).

4.5 Mixed-Integer Multi-Objective Particle Swarm Optimization

The multi-objective PSO (MOPSO), although requires much computation, is used because of its fast convergence rate and reliability. The objectives are treated individually for each candidate particle rather than using the traditional method that combines weighted objectives. The MOPSO is an extension of the single objective PSO. Generally, the PSO algorithms are global search methods based on social behavioral patterns of bird flocks known as swarm [66] [67]. Each candidate solution, called a particle, has the capacity to learn from its past experience and experience of other particles to update its position. The dynamics of MOPSO are well detailed in

[68]. The MOPSO add multi-dimensional analysis to the PSO where several best solutions for a given problem are obtained. These solutions are termed the Pareto set. The Pareto set contains non-dominated solutions of the problem obtained through the dominance criteria given in equations (4.50-4.51) [69]. If (4.50-4.51) is true, then x^1 dominates x^2 .

$$\forall i \in \{1,2,3, \dots, N_{obj}\} : f_i(x^1) \leq f_i(x^2) \quad (4.50)$$

$$\exists j \in \{1,2,3, \dots, N_{obj}\} : f_j(x^1) < f_j(x^2) \quad (4.51)$$

Where N_{obj} is the number of objective functions and, x^1 and x^2 are any two different solutions.

Several steps of the MOPSO are similar to PSO except for additional terms like non-dominated local set S^* , non-dominated global set S^{**} , and the external set. Furthermore, the criteria for selecting the individual particle local best X^* , and global best X^{**} are different [68]. At the onset, each particle position X and velocity V are initialized as given in (4.52), while the limits of V are expressed in (4.53). The dominance criteria (4.50)-(4.51) are used to select the members of S^* per individual particle, and to select members of S^{**} from the union of all S^* . The external set contains the Pareto set and is updated by non-dominated particles of S^{**} at every generation. Then closest particle in S^{**} to individual S^* is chosen as the global best while the corresponding particle in S^* is chosen as the local best. For other generations, the particle velocity and location are updated as in (4.54) and (4.56) respectively. The cycle continues until maximum number of generation is met.

$$x_{j,k} = x_{j,k}^{\min} + r(x_{j,k}^{\max} - x_{j,k}^{\min}) \quad (4.52)$$

$$V_{\max} = \frac{x^{\max} - x^{\min}}{N} \text{ and } V_{\min} = -V_{\max} \quad (4.53)$$

$$V_{j,k}(t) = w(t)V_{j,k}(t-1) + c_1r_1 \left(x_{j,k}^*(t-1) - x_{j,k}(t-1) \right) + c_2r_2 \left(\frac{x_{j,k}^{**}(t-1) - x_{j,k}(t-1)}{x_{j,k}(t-1)} \right) \quad (4.54)$$

$$w(t) = \alpha w(t-1) \quad (4.55)$$

$$x_{j,k}(t) = V_{j,k}(t) + x_{j,k}(t-1) \quad (4.56)$$

Where r , r_1 and r_2 are uniformly distributed random numbers in $[0, 1]$, and N is the number of intervals each parameter is divided into. Where α is a constant less than 1 but very close to 1, c_1 and c_2 are cognitive and social parameters positive, $x_{j,k}$ is a parameter of particle j in dimension k , $x_{j,k}^*$ is the local best of parameter k of particle j , and $x_{j,k}^{**}$ is the global best of parameter k of particle j , and $w(t)$ is the inertia weight defined in (4.55).

4.5.1 Dealing with the Discrete Variable

The expected optimization problem has a discrete variable which lies in every particle. The discrete variable cannot be dealt with like the continuous variable as explained in the section above. Given a set of discrete variables (X_{DV}) as in (4.57), the method of optimizing the index 'j' of the chosen discrete variable $x_j \in X_{DV}$ rather than directly optimizing the discrete variable is employed [70].

$$X_{DV} = \{x_1, x_2, \dots, x_{n_{DV}}\} \quad (4.57)$$

Where n_{DV} is the total number of discrete variables.

Normally, real coded variables in the range $[1, n_{DV}]$ are generated in every particle, hence in choosing an index of a discrete variable, the two closest integers to the real coded variables are used. A die is tossed to choose one of the two integers as the required index.

4.6 Theory of Calculating the Objective Functions

This thesis work has proposed a four objective optimization problem for the optimal design of a hybrid renewable electrical microgrid as given in (4.29)-(4.32). Furthermore, a bid is made to show the theories of calculating each objective. A matrix each for the base cases of C_{ihy}^x , T_{ihy}^w , and S_{ihy}^z are presented in (4.58)-(4.60) below.

$$C_{BC} = \begin{bmatrix} C_{111}^1 & C_{211}^1 & \cdots & C_{nD,nH,nY}^1 \\ C_{111}^2 & C_{211}^2 & \cdots & C_{nD,nH,nY}^2 \\ \vdots & \vdots & \vdots & \vdots \\ C_{111}^{nX} & C_{211}^{nX} & \cdots & C_{nD,nH,nY}^{nX} \end{bmatrix} \quad (4.58)$$

$$T_{BC,Z} = \begin{bmatrix} T_{111}^1 & T_{211}^1 & \cdots & T_{nD,nH,nY}^1 \\ T_{111}^2 & T_{211}^2 & \cdots & T_{nD,nH,nY}^2 \\ \vdots & \vdots & \vdots & \vdots \\ T_{111}^{nW} & T_{211}^{nW} & \cdots & T_{nD,nH,nY}^{nW} \end{bmatrix} \quad \forall z \quad (4.59)$$

$$S_{BC} = \begin{bmatrix} S_{111}^1 & S_{211}^1 & \cdots & S_{nD,nH,nY}^1 \\ S_{111}^2 & S_{211}^2 & \cdots & S_{nD,nH,nY}^2 \\ \vdots & \vdots & \vdots & \vdots \\ S_{111}^{nZ} & S_{211}^{nZ} & \cdots & S_{nD,nH,nY}^{nZ} \end{bmatrix} \quad (4.60)$$

Where C_{BC} , $T_{BC,Z}$, and S_{BC} contain base case (BC) state values of all components, tie-sets of the ‘z-th’ LP, and LPs respectively. Also, ‘nX’ and ‘nZ’ are the total numbers of all components and LPs respectively, while ‘nW’ is the total number of tie-sets of a corresponding LP. Furthermore, C_{BC} , $T_{BC,Z}$, and S_{BC} , all have the same number of columns since it represents the total number of states, ‘nstates’, in any simulation period defined in (4.61). And lets ‘k’ be the index of the states of the components.

$$k = 1, 2, 3, \dots, nstates = nD \times nH \times nY \quad (4.61)$$

Hence with the definition of the index ‘k’, C_{BC} , $T_{BC,Z}$, and S_{BC} can be re-written in terms of ‘k’.

Matrix C_{BC} is exemplified in (4.62).

$$C_{BC} = \begin{bmatrix} C_1^1 & C_2^1 & \dots & C_{nstates}^1 \\ C_1^2 & C_2^2 & \dots & C_{nstates}^2 \\ \vdots & \vdots & \vdots & \vdots \\ C_1^{nX} & C_2^{nX} & \dots & C_{nstates}^{nX} \end{bmatrix} \quad (4.62)$$

To infuse the effects of the MOPSO, every particle, X , has the required dimension and a general case of expected particle is expressed in (4.63). The location of all the DGs is indicated by L_{DG} . In order to assess the possibility of power transfer from L_{DG} to any LP, the states of each LP and corresponding tie-sets must be obtained. Hence, let $T_{LDG,Z}$ and S_{LDG} represent matrices containing states of tie-sets of individual LP and LPs similar to $T_{BC,Z}$, and S_{BC} respectively. Equation (4.64) gives a clarification of the operational states of any ‘z-th’ LP, at any state number ‘k’, during the base case and optimization.

$$X = [P_w^R, P_S^R, C_B^R, P_T^R, L_{DG}] \quad (4.63)$$

$$T_{k,LDG}^w \in T_{LDG,Z}; T_{k,BC}^w \in T_{BC,Z}; S_{k,LDG}^z \in S_{LDG}; S_{k,BC}^z \in S_{BC} \quad \forall k \quad (4.64)$$

The possibility of increasing reliability performance of any system is enhanced via existence of alternate power flow route when the base case fails via failure of any component(s). This is the essence of L_{DG} , $T_{LDG,Z}$ and S_{LDG} . Hence, there exist one or more states were an LP is islanded in the base case, this states must be found and analyzed for alternative route via the DGs placed at L_{DG} . The required procedures are delineated below.

$$\exists k \in \{1,2,3, \dots, nstates\} : C_k^x = T_{k,BC}^w = S_{k,BC}^z = \{ 0 \mid C^x \subset T^{w,BC} \text{ and } T^{w,BC} \subset S^{z,BC} \} \quad (4.65)$$

$$\therefore \text{iLP}_k = \{z \mid S_{k,BC}^z = 0\} \text{ and } P_k^{\text{iLP}} = \sum_z P_k^z \quad \forall z \mid S_{k,BC}^z = 0 \quad (4.66)$$

$$\text{But : } \text{NiLP}_k = \{z \mid z \in \text{iLP}_k \text{ and } S_{k,LDG}^z = 0\} \quad (4.67a)$$

$$\text{RiLP}_k = \text{iLP}_k - \text{NiLP}_k = \{z \mid z \in \text{iLP}_k \text{ and } z \notin \text{NiLP}_k \text{ and } S_{k,LDG}^z = 1\} \quad (4.67b)$$

$$P_k^{\text{RiLP}} = \sum_z P_k^z \quad \forall z \mid z \in \text{RiLP}_k \quad (4.68)$$

Hence, the set of islanded LP, ‘iLP’ and the total power demand of these LPs at any state, P_k^{iLP} , are given in (4.66). However, not all members of iLP are reachable via L_{DG} , hence iLP is divided in two groups; reachable (RiLP) and non-reachable islanded LPs (NiLP) in (4.67). And the total power demand of all members of RiLP is given in (4.68). Obviously, the only helpable LPs are those of the RiLP set. However, the level at which the demand of RiLP will be covered depends on the total available power from all DGs at the particular state ‘k’. First the conditions at which all RiLP demand will be met are given in (4.69).

$$P_k^w + P_k^S \geq P_k^{\text{RiLP}} \quad (4.69a)$$

$$P_k^w + P_k^S + P_k^B \geq P_k^{\text{RiLP}} \quad (4.69b)$$

$$P_k^w + P_k^S + P_k^B + P_k^T \geq P_k^{\text{RiLP}} \quad (4.69c)$$

If any condition of (4.69) is satisfied, arranged by priority, then all LPs of the RiLP group have their power needs covered. Hence, a final state matrix ‘ S_F ’ that registers these adjustments is required. First, S_F is a replica of S_{BC} before the adjustments are made in it as depicted in (4.70)-(4.71).

$$S_F = S_{BC} \quad (4.70)$$

$$S_{F(z \times k)} = \max(S_{k,BC}^z, S_{k,LDG}^z) = \frac{1}{2}(S_{k,BC}^z + S_{k,LDG}^z + |S_{k,BC}^z - S_{k,LDG}^z|) \quad \forall z | z \in \text{RiLP}_k \quad (4.71)$$

$$\text{But if : } P_k^w + P_k^s + P_k^b + P_k^t = P_k^{Av} < P_k^{\text{RiLP}} \quad (4.72)$$

$$\text{Then : } \text{CG}_k = \{ z | z \in \text{CR and } z \in \text{RiLP}_k \} \quad (4.73)$$

However, if the total available power, P_k^{Av} , is less than P_k^{RiLP} as shown in (4.72), then RiLP_k is divided to two groups; Critical group CG_k and Non-critical group NCG_k . All members of both CG_k and NCG_k groups are further ranked by the distance of each element from L_{DG} . Thereafter, the critical loads are given priority over the non-critical group members. Whenever P_k^{Av} is larger than the next demand in the hierarchy of LP to be met, then such LP state is updated and its power is deducted from P_k^{Av} has given in (4.74).

$$\text{if } P_k^{Av} \geq P_k^z, \text{ then } P_k^{Av} = P_k^{Av} - P_k^z \text{ and } S_{F(z \times k)} = \max(S_{k,BC}^z, S_{k,LDG}^z) \quad \forall z | z \in \text{CG}_k \quad (4.74)$$

If all CG_k members are supplied and $P_k^{Av} \geq P_k^z$ still holds for the first and more members of NCG_k , then (4.74) continues to hold for the LPs in NCG_k . But this not guaranteed, as $P_k^{Av} < P_k^z$ might hold even before all CG_k members are supplied. However, it is guaranteed that there must be at least one LP such that $P_k^{Av} < P_k^z$ and this condition with consequent actions are given in (4.74)-(4.75).

$$\exists z | (z \in \text{CG}_k \text{ or } z \in \text{NCG}_k) : P_k^{Av} < P_k^z \quad (4.74)$$

$$\therefore \text{PES}_z = \text{PES}_z + D \cdot P_k^{Av} \text{ and } S_{F(z \times k)} = \min(S_{k,BC}^z, S_{k,LDG}^z) \quad (4.75)$$

At this stage, the remaining available power $P_k^{Av} < P_k^z$ which is not enough for the next LP makes the LP be partially served. Hence equation (4.75) confirms that partial energy served (PES) but

the state of such LP will remain zero. Therefore, via the equations in section 4.4 and the use of final states of all LPs given in S_F all objectives can be comfortably calculated.

4.7 Other Important Algorithms

4.7.1 Clustering Algorithm

Similar to the amount of real numbers between any two numbers, there could be an enormous number of data points on the Pareto optimal front. To reduce the size of the Pareto optimal front to a preset size, the clustering algorithm is employed. Clustering algorithm groups non-dominated solutions into the same cluster based on their proximity in objective space. This process continues repeatedly until the required number of clusters is obtained. The algorithm for selecting the closest clusters is given in (4.76).

$$d_c = \frac{1}{n_1 n_2} \sum_{i_1 \in c_1, i_2 \in c_2} d(i_1, i_2) \quad (4.76)$$

Where d_c is the distance between the two clusters c_1 and c_2 , $d(i_1, i_2)$ is the distance between the two particles i_1 and i_2 , while n_1 and n_2 are the total number of particles in clusters c_1 and c_2 respectively. Hence, at any iteration any two clusters with minimum d_c are combined. Afterwards, a representative of each cluster is defined as the closest particle to the centroid of the cluster.

4.7.2 Fuzzy Approach to Extract Best Compromise Solution

After reaching the maximum number of generations and obtaining the required number of clusters, it is useful to indicate a solution of best compromise. The best compromise solution of all the non-dominated global best solutions can be selected using a fuzzy approach as explained in [71]. In the fuzzy logic approach for obtaining the best compromise solution, each objective function of every

non-dominated solution is mapped to a membership function value, μ_i , in the range [0, 1] using equation (4.77). This involves the maximum and minimum values of each i -th objective function; f_i^{max} and f_i^{min} .

$$\mu_i = \begin{cases} 1 & f_i \leq f_i^{min} \\ \frac{f_i^{max} - f_i}{f_i^{max} - f_i^{min}} & f_i^{min} \leq f_i \leq f_i^{max} \\ 0 & f_i \geq f_i^{max} \end{cases} \quad (4.77)$$

Then a normalized membership function, μ^k , representing the k -th non-dominated solution, is used to obtain the best compromise solution. The solution with the maximum μ^k is the best compromise solution. μ^k is defined in (4.78).

$$\mu^k = \frac{\sum_{i=1}^{N_{obj}} \mu_i^k}{\sum_{k=1}^M \sum_{i=1}^{N_{obj}} \mu_i^k} \quad (4.78)$$

CHAPTER 5

SIMULATION AND RESULTS

5.1 TEST SYSTEM: RBTS-BUS2

The earlier proposed algorithms will be implemented on the RBTS-Bus2 [72] to obtain all the tie sets of all LPs in these RBTS buses, the reliability indices at all the LPs, and the overall system reliability indices. The single line diagram and the single line block diagrams of RBTS-Bus2 are shown in figures 5.1 and 5.2 respectively. RBTS-Bus2 has 22 LPs, 56 line components and 55 nodes. The line components are 36 feeders (labeled 1-36) and 20 transformers (labeled 37-56).

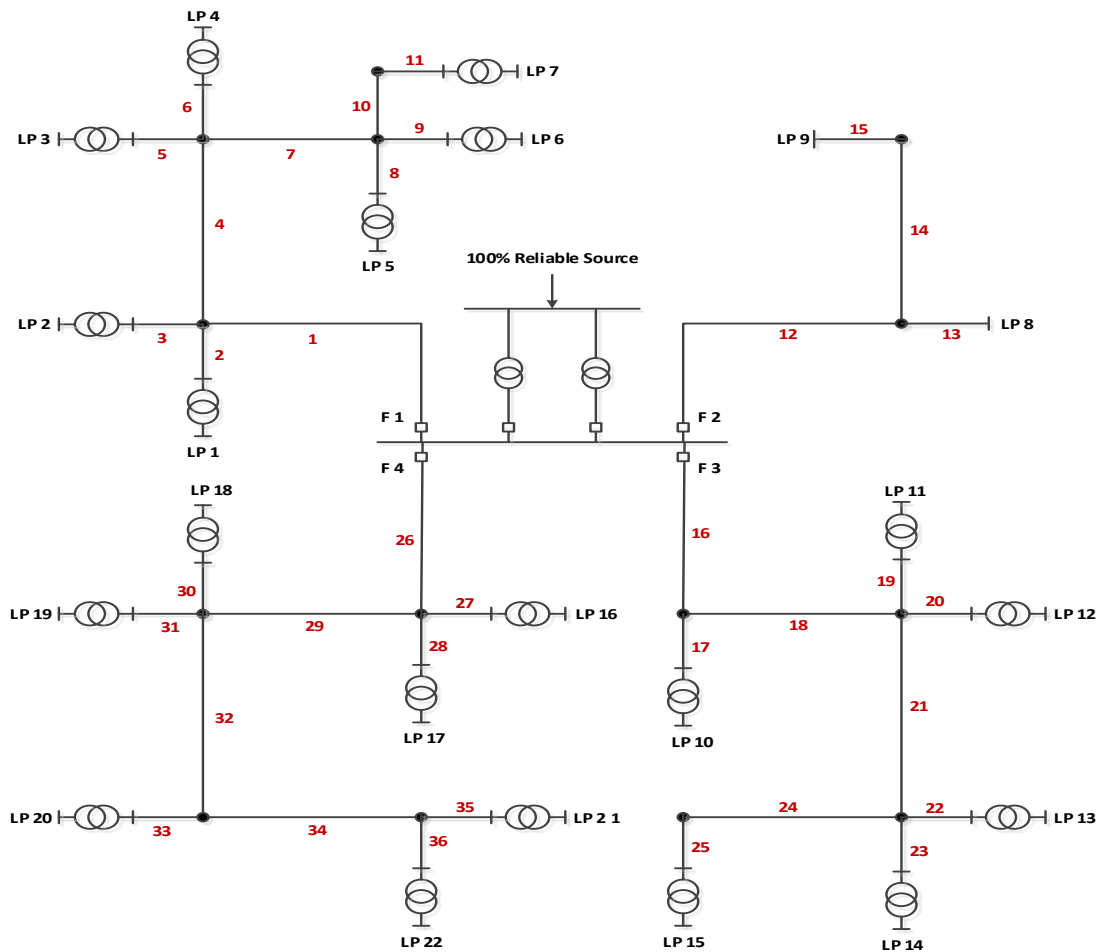


Figure 5.1: Single line diagram of RBTS-BUS2

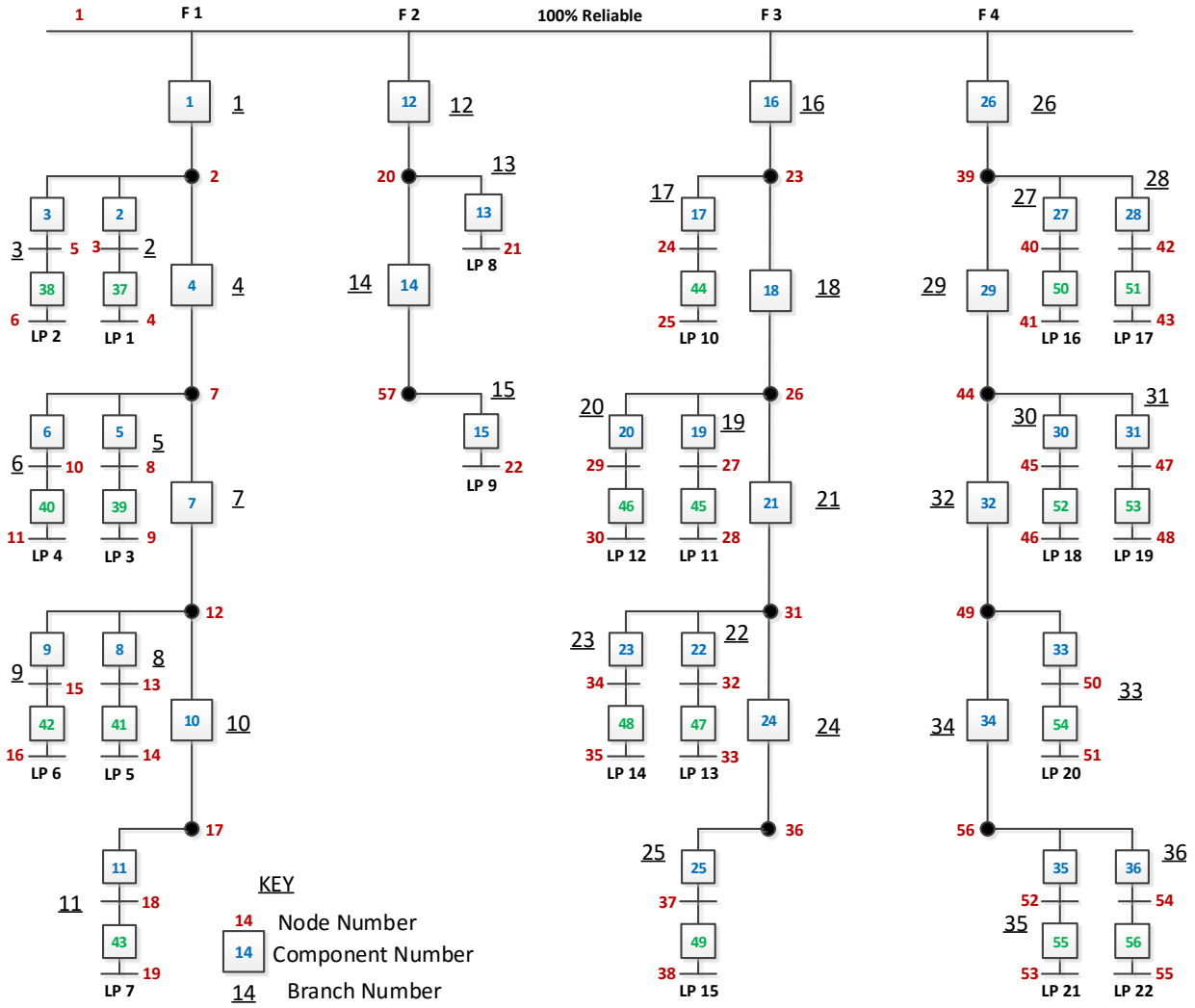


Figure 5.2: Single Line Block Diagram of RBTS-Bus2

5.1.1 Consumer Types and Load Modeling

The RBTS-Bus 2 has a total peak load of 20MW distributed over 22 LPs. Each LP consists of a unique consumer type. The four consumer types are outlined below:

1. Residential Consumer.
2. Commercial Consumer.
3. Industrial Consumer.
4. Government/Institution Consumer.

The numbers of each consumer type attached to each LP, and the peak load observed at each LP are shown in Table 5.1.1.

Table 5.1: Load Points Data and Consumers [72]

LP	Type	Peak Load (MW)	Number of customers
1	Residential	0.8668	210
2	Residential	0.8668	210
3	Residential	0.8668	210
4	Gov/Inst	0.9167	1
5	Gov/Inst	0.9167	1
6	Commercial	0.75	10
7	Commercial	0.75	10
8	Small user	1.6279	1
9	Small user	1.8721	1
10	Residential	0.8668	210
11	Residential	0.8668	210
12	Residential	0.7291	200
13	Gov/Inst	0.9167	1
14	Gov/Inst	0.9167	1
15	Commercial	0.75	10
16	Commercial	0.75	10
17	Residential	0.7291	200
18	Residential	0.7291	200
19	Residential	0.7291	200
20	Gov/Inst	0.9167	1
21	Gov/Inst	0.9167	1
22	Commercial	0.75	10

5.1.2 Seasonal Effects

Each consumer is unique in its consumption pattern, the consumption pattern depends on factors like the season of the year, the time of the day, and the day of the week. Four seasons were considered in every year, and season timing and sequence of the northern hemisphere is chosen. It is known that about 90% of the world population lives in the northern hemisphere. Table 5.2 shows the seasons and their sequence of occurrence, dates and hours. The seasons affects the consumption patterns of different consumers in diverse ways. The residential consumption has the largest seasonal power consumption variation. For instance, during summer, air conditioning and

refrigeration loads soar in number, while in winter, it is more of heating loads. The commercial loads show slight seasonal effects, while the industrial and government loads are almost immune to seasonal effects. Also the time of the days is a major cause of variation in consumption pattern of most consumers. Residential loads usually have peaks in the evenings towards early nights and reduces onwards to a minimum just few hours after midnight. The commercial consumers also show a marked time-based consumption, being more active from mid-morning to late afternoons. The industrial user is mostly consuming power at a constant rate except for few hours after midnight, hence showing an almost constant load profile. Residential loads seem a bit lower during weekends than week days. All other loads show no day-of-the-week variations. These pattern are depicted in tables provided in the appendix.

Table 5.2: Northern Hemisphere Seasons, Dates and Hours [73]

Season	Period	Hour Range	Total Days
Winter	December 21, Solstice – March 20, Equinox	1-1896 and 8497-8760	90
Spring	March 21, Equinox – June 20, Solstice	1897-4104	92
Summer	June 21, Solstice – September 20, Equinox	4105-6312	92
Fall	September 21, Equinox – December 20, Solstice	6313-8496	91

5.1.3 Load Profile

To produce the load profile of the several considered load types, efforts are made to represent seasonal effects in terms of time of the day, day of the week, and week of the year variations. This factors were represented as fractions in per unit as given in the appendix. The hourly loads (P_h), daily loads (P_d), and weekly loads (P_w) are given as percentages of daily peaks, weekly peaks, and annual peaks respectively. Hence, a per unit load demand of any consumer types at hour h of day d in week w is given in equation 5.1 below.

$$L(h, d, w) = P_w P_d P_h \quad \forall h, d, w \quad (5.1)$$

By using equation 5.1, the load profile of each consumer type is generated for a year. However, each 7 days of 52 weeks amounts to 364 days rather than 365 days per year. Hence, the allocation factor of the 365th day is missing. To solve this issue, the average of the allocation factors of the 364th and 1st day was used. Therefore, the per unit load demand of every consumer type at every hour for all 365 days amount to 8760 hourly load data. The load profiles of each consumer type are given in figures 5.1-5.4.

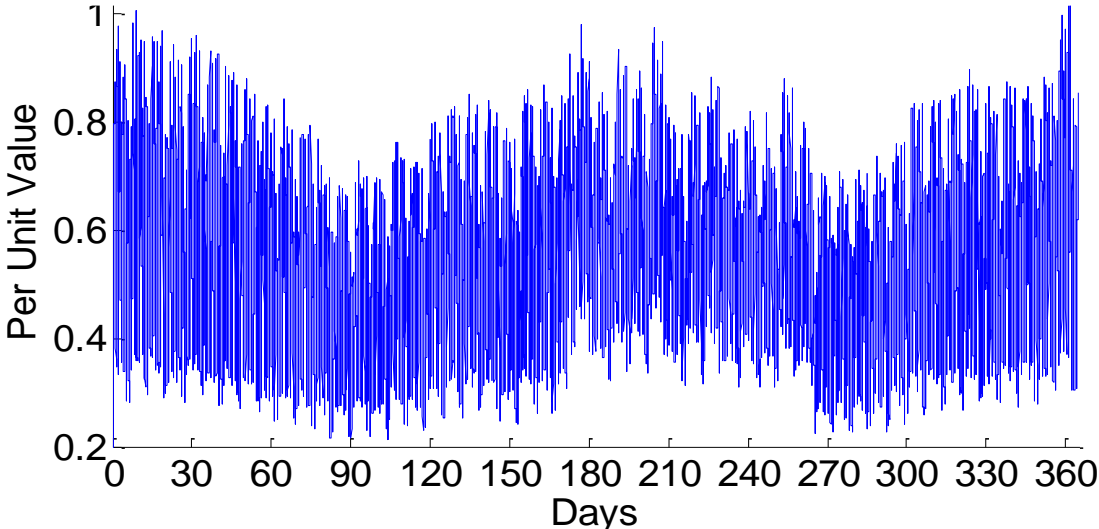


Figure 5.3: Residential Load Profile

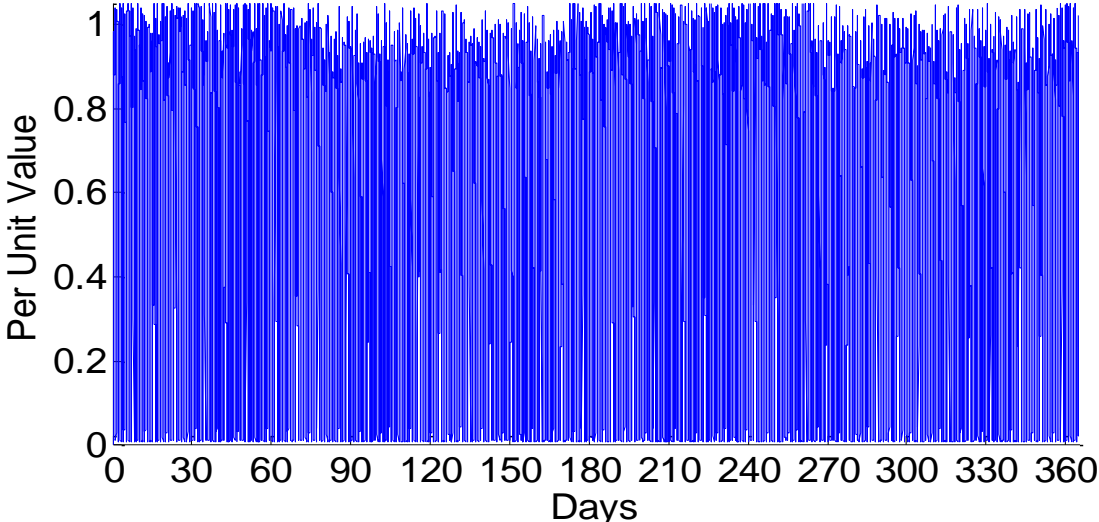


Figure 5.4: Commercial Load Profile

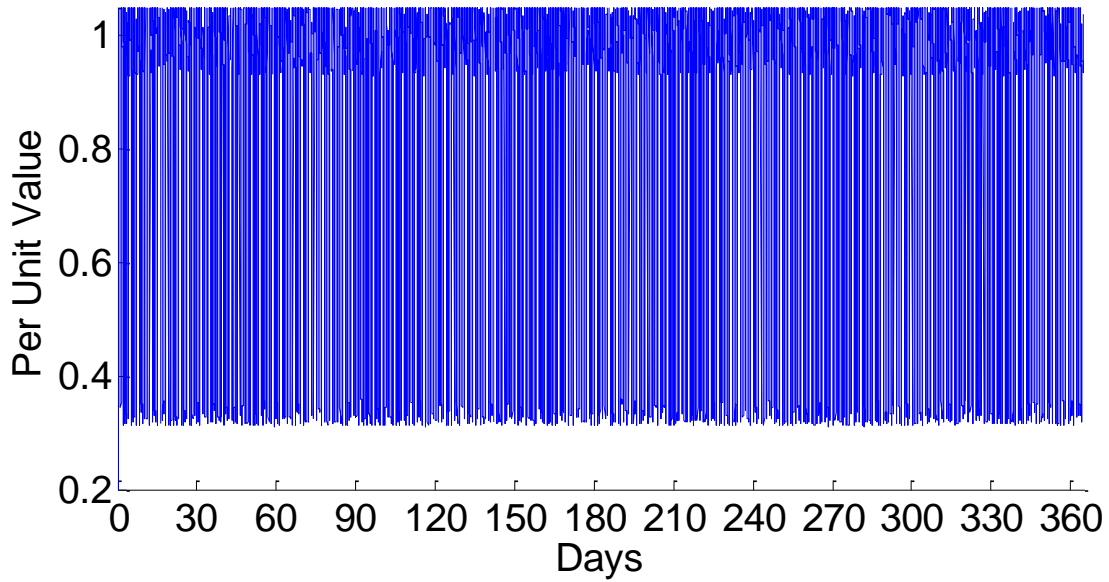


Figure 5.5: Industrial Load Profile

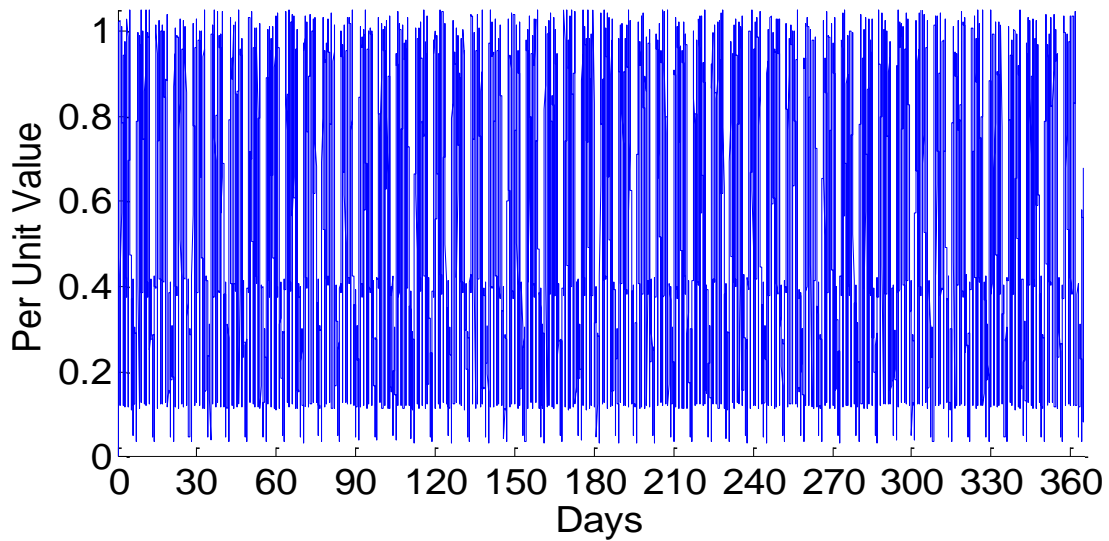


Figure 5.6: Government/Institution Load Profile

The load profile in Megawatts (MW) at every LP is obtained by multiplying the corresponding load profile in per unit with the corresponding peak load of each LP.

5.1.4 LP Tie-Sets and Reliability Data of RBTS-BUS2 Components

The proposed algorithm is used to obtain the tie sets of all the 22 LPs of RBTS-Bus2 as given in table 5.3. The tie sets consist of all components traversed from the source to the LPs. Obviously,

each LP has one path for receiving power from the SP. The SP as four main feeder components (1, 12, 16 and 26) which distribute power to all other sub-feeders. The main feeders begin every tie set, and each LP can receive power from only one of these four main feeders.

Table 5.3: Tie Set of LPs in RBTS-Bus2

LP	TIE SET	LP	TIE SET	LP	TIE SET
1	[1-2-37]	9	[12-14-15]	17	[26-28-51]
2	[1-3-38]	10	[16-17-44]	18	[26-29-30-52]
3	[1-4-5-39]	11	[16-18-19-45]	19	[26-29-31-53]
4	[1-4-6-40]	12	[16-18-20-46]	20	[26-29-32-33-54]
5	[1-4-7-8-41]	13	[16-18-21-22-47]	21	[26-29-32-34-35-55]
6	[1-4-7-9-42]	14	[16-18-21-23-48]	22	[26-29-32-34-36-56]
7	[1-4-7-10-11-43]	15	[16-18-21-24-25-49]		
8	[12-13]	16	[26-27-50]		

The reliability data of all the components in RBTS-Bus2 are given in table 5.4. Table 5.45.4 contains the failure rate (λ) in failures/year (f/y), and repair rate (μ) in repairs/year (r/y) of each component, and the length if the component is a feeder.

Table 5.4: Reliability Data of RBTS-Bus2 Components

Components	Length (km)	λ (f/y)	μ (r/y)
2, 6, 10, 14, 17, 21	0.64	2.3	500
25, 28, 30, 34	0.71	2.5	500
1, 4, 7, 9, 12, 16, 19	0.77	2.8	500
22, 24, 27, 29, 32, 35	0.83	3.1	500
3, 5, 8, 11, 13, 15, 18	0.88	3.4	500
20, 23, 26, 31, 33, 36	0.92	3.8	500
37 - 47	NA*	1.5	53
48-56	NA*	1.3	47

*NA mean Not Applicable (for Transformer Components)

5.2 LP and System Reliability Indices without DGs (Base Case)

The reliability indices of the 22 LPs in RBTS-BUS2 are calculated via the results of the proposed tie-set algorithm explained in section 4.1 and results given in Table 5.3, and the MCS and ITM simulations. The component reliability data given in Table 5.4 are used for the MCS and ITM simulations while the proposed pseudo-digitization method explained in section 4.3 is used to routinely capture the state of each component. Individual LP indices are obtained via the equations 4.10-4.21 given in section 4.4.1. However, due to the stochastic nature of the underlying MCS and ITM techniques, several repeated simulations are required to obtain steady average values of the LP indices. Figures 5.7-5.10 show how LP reliability indices vary with simulation time.

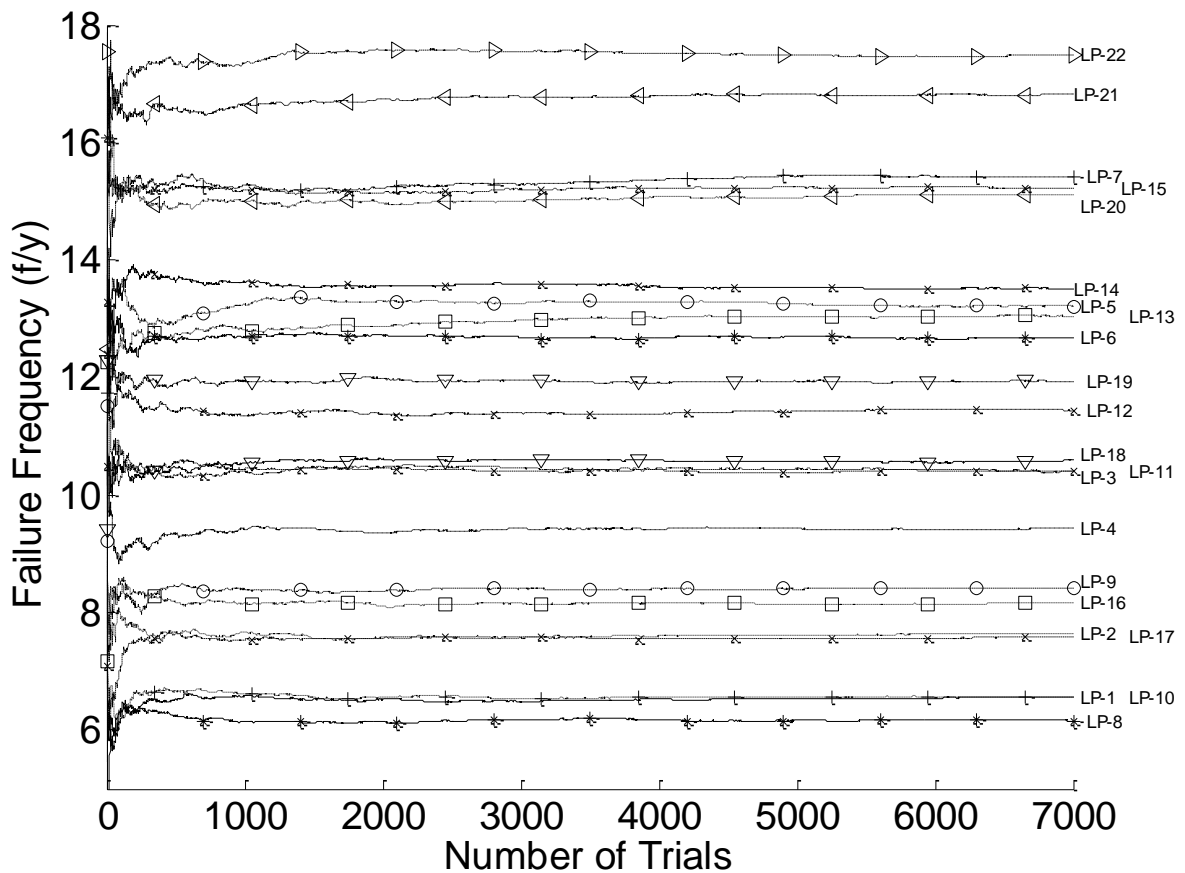


Figure 5.7: Variation of Failure Frequency of all LPs

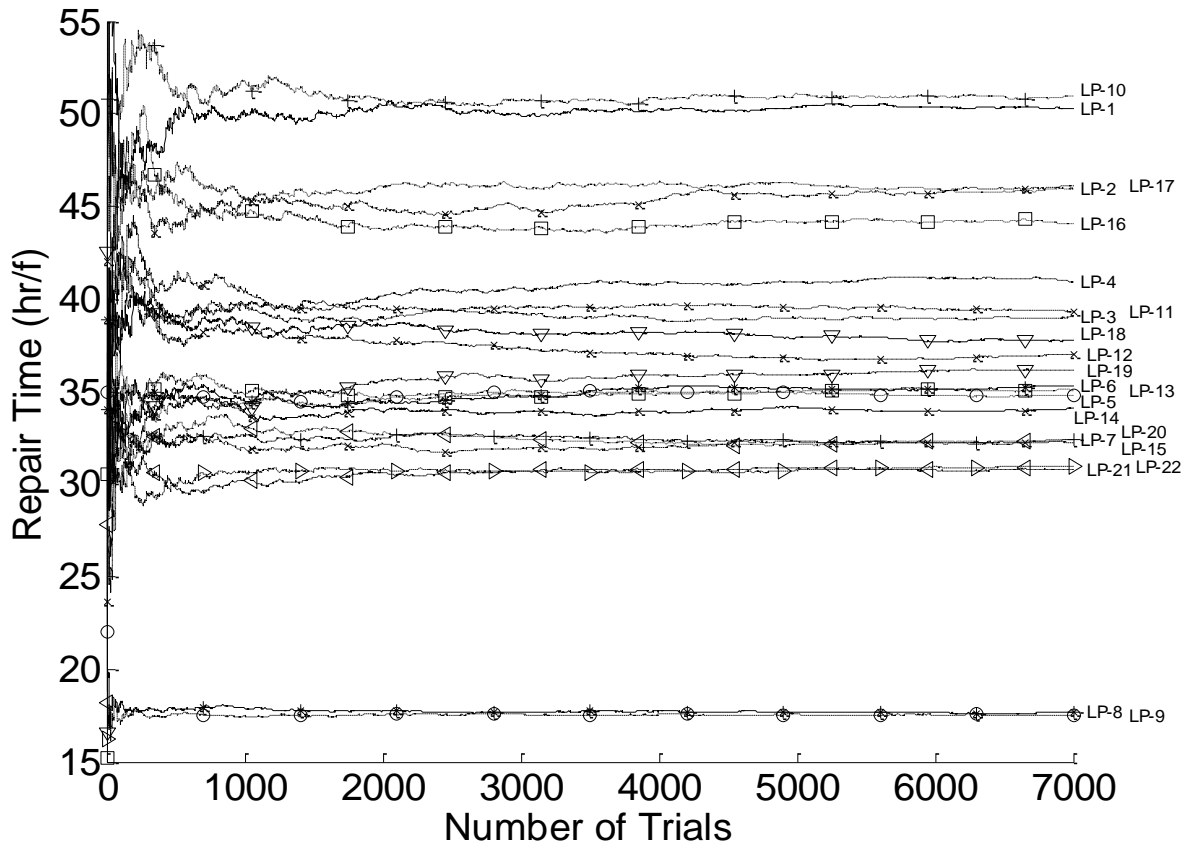


Figure 5.8: Variation of Repair Times of All LPs

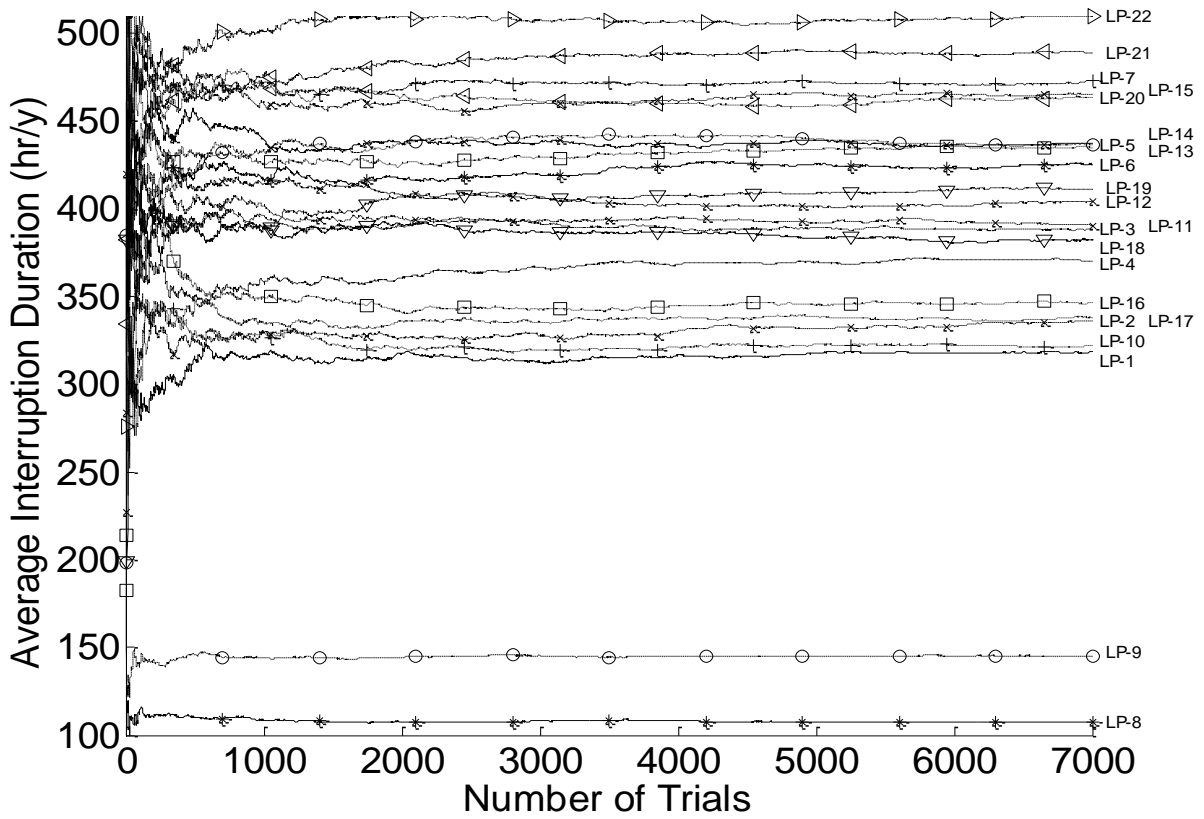


Figure 5.9: Variation of Average Interruption Duration of All LPs

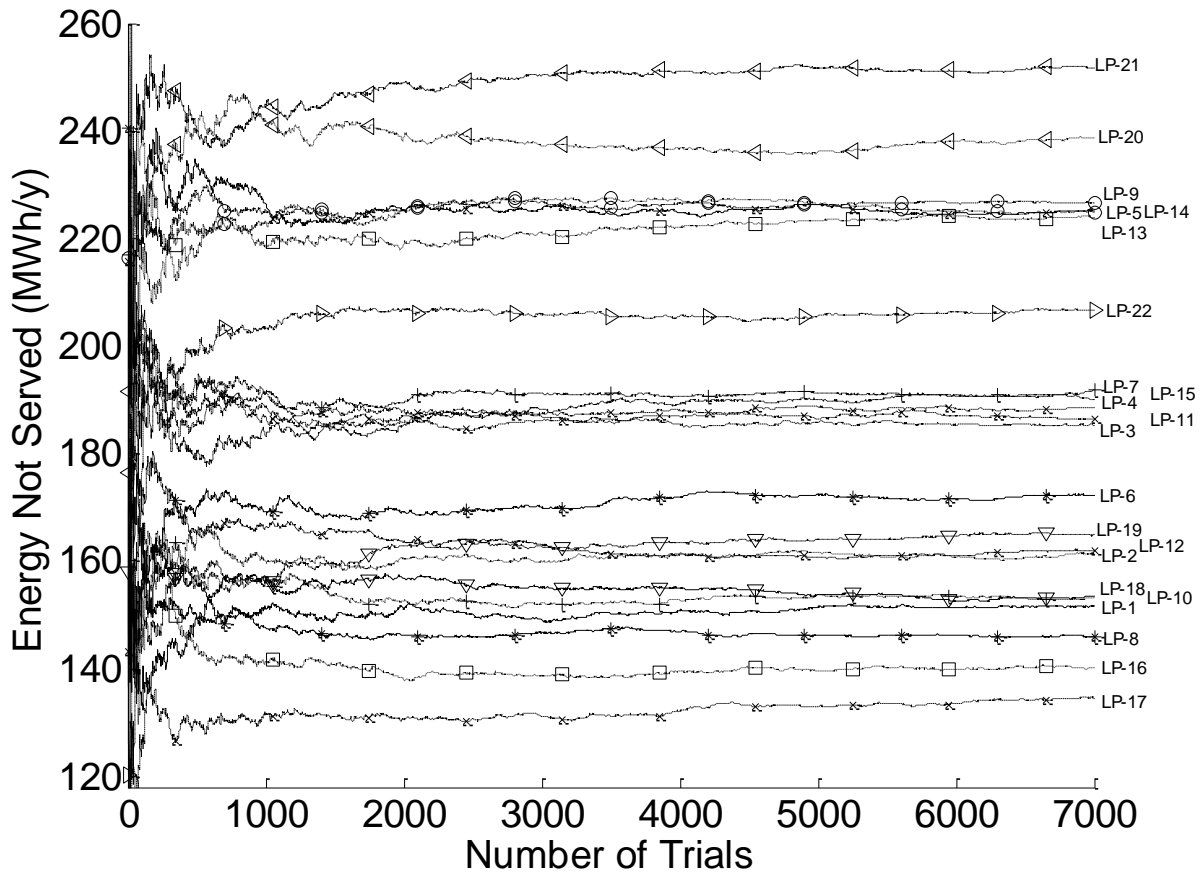


Figure 5.10: Variation of Energy Not Served of All LPs

The average values of several load point reliability indices are computed and given in table 5.5. The computed indices are availability (A), failure frequency (λ), repair time (r), average interruption duration (AID), average uptime duration (AUD), energy not served (ENS), average energy not served (AENS), and energy not served per interruption (ENSI).

The overall system indices are computed from individual LP reliability indices via equations 4.22-4.25 explained in section 4.4.2. The computed system indices are ASAI, SAIDI, CAIDI, SAIFI, ENS and AENS. The final values of these metrics, calculated and averaged over 7000 years of simulation time, are given in table 5.6.

Table 5.5: Reliability Indices of All Load Points without DGs

LP	A	λ (f/y)	r (h/f)	AID (h/y)	AUD (h/y)	ENS (MWh/y)	AENS (MWh/c.y)	ENSI (MWh/f)
1	0.963686	6.563195	50.29581	318.1138	8441.886	151.6378	0.7220850	23.974904
2	0.961413	7.647968	45.97139	338.0211	8421.979	161.4563	0.7688394	21.958303
3	0.955697	10.40796	39.01697	388.0962	8371.904	185.3369	0.8825567	18.632711
4	0.957784	9.430546	40.94249	369.8101	8390.190	190.1218	190.12177	21.048799
5	0.950171	13.21447	34.76453	436.5034	8323.497	224.8581	224.85814	17.908422
6	0.951445	12.66480	35.29847	425.3416	8334.658	172.3175	17.231747	14.300374
7	0.946008	15.41590	32.43142	472.9659	8287.034	191.7652	19.176516	13.149396
8	0.987739	6.160821	17.64953	107.4024	8652.598	145.9399	145.93989	23.982423
9	0.983416	8.425445	17.53368	145.2791	8614.721	226.7443	226.74426	27.365686
10	0.963262	6.554812	50.97041	321.8272	8438.173	153.2875	0.7299403	24.277394
11	0.955425	10.39537	39.31485	390.4751	8369.525	186.2899	0.8870945	18.756529
12	0.953907	11.44197	36.99422	403.7761	8356.224	161.9772	0.8098862	14.840457
13	0.950367	13.04579	35.06814	434.7848	8325.215	223.8718	223.87177	18.056672
14	0.950086	13.50976	34.06564	437.2471	8322.753	225.2121	225.21211	17.546131
15	0.946888	15.23095	32.26078	465.2650	8294.735	188.4818	18.848180	13.069047
16	0.960483	8.175797	44.08268	346.1687	8413.831	140.1577	14.015768	17.848311
17	0.961693	7.572952	46.07628	335.5670	8424.433	134.5792	0.6728959	18.478897
18	0.956327	10.58872	37.78023	382.5734	8377.427	153.4902	0.7674512	15.157606
19	0.953093	11.92793	36.14423	410.9031	8349.097	164.8657	0.8243283	14.502063
20	0.947074	15.10955	32.39954	463.6329	8296.367	238.7602	238.76024	16.685019
21	0.944181	16.81214	30.80377	488.9702	8271.030	251.7714	251.77137	15.860899
22	0.941873	17.48082	30.92646	509.1952	8250.805	206.5695	20.656955	12.546196

Table 5.6: System Reliability Indices without DGs

ASAI	SAIDI (h/c.y)	CAIDI (h/f)	SAIFI (f/c.y)	ENS (MWh/y)	AENS (MWh/c.y)
0.956233	383.39567	41.047540	9.340284	4079.491878	2.138098

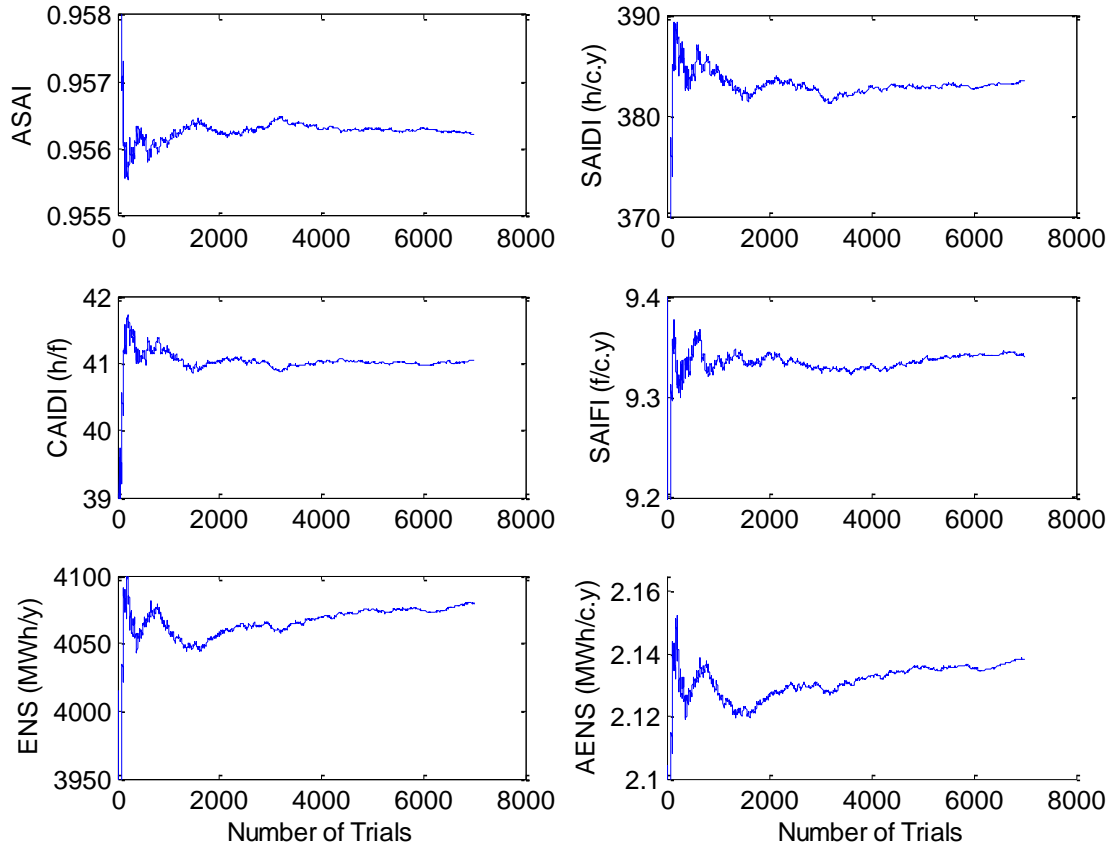


Figure 5.11: Variation of System Reliability Indices without DGs

Figure 5.11 depicts how the overall system reliability indices gradually converge to a steady value as the years of simulation increases. It also helps to justify the use of large simulation time.

5.3 LP and System Reliability Indices with System-Connected DGs

The methodology and formulations delineated in chapter 4 are applied on the RBTS-BUS2 test system to optimize the performance of the entire system and individual LPs. In the mixed-integer multi-objective particle swarm optimization, the integer decision variable is the location of all the DG resources (L_{DG}), while the other four decision variables ($P_w^R, P_S^R, C_B^R, P_T^R$) are real numbers. The lower limit of real coded decision variables, $P_{w,\min}^R, P_{S,\min}^R$ and $P_{T,\min}^R$, is 50KW, while

minimum capacity of the battery storage system, $C_{B,\min}^R$, is 50KWh. The charging and discharging rate is limited to 50% of C_B^R enabling full charge and discharge within 2 hours. Also, the charging/discharging efficiencies are 90% and the DOD is capped at 65% maximum. The location variable is a set of selected buses of RBTS-BUS2 as given in (5.2).

$$L_{DG} \in \{ 1, 2, 7, 12, 17, 20, 23, 26, 31, 36, 39, 44, 49, 56, 57 \} \quad (5.2)$$

The total installation cost of each type of DG are determined as ICW = \$1835/KW, ICS = \$2955/KW, ICB = \$700/KWh, ICD = \$400/KW and OCD = \$0.45/KWh [74] [75]. The wind speed, solar irradiance and ambient temperature data for 10 years with resolution of 15 minute per data point is used [76] [77]. Hence, each division interval, $D = 0.25$ hrs. Each particle of the optimization makes 30 runs of the 10-years set of data, culminating in 300 years of simulation.

The optimization procedure contains 50 particles per generation, each particle runs 300 years of simulation, and ends at 150 generations. Also the inertia weight, $w(t) = 1.1$, decrement factor, $\alpha = 0.99$, the acceleration constants, $C_1 = C_2 = 2.0$. Clustering the non-dominated local set and external set are kept at 10 and 100 particles respectively. Two cases of the optimization are analyzed; One with all DGs including the battery and the other without the battery.

5.3.1 System With All DGs Including Battery (Case-1)

In this case study, all five variables, including the battery size, are considered. All other parameters of the optimization are as stated earlier. Hence, the Pareto optimal front contains 100 solution points of the four objective functions and five decision variables. This four dimensional Pareto optimal front is shown in figure 5.12 given below.

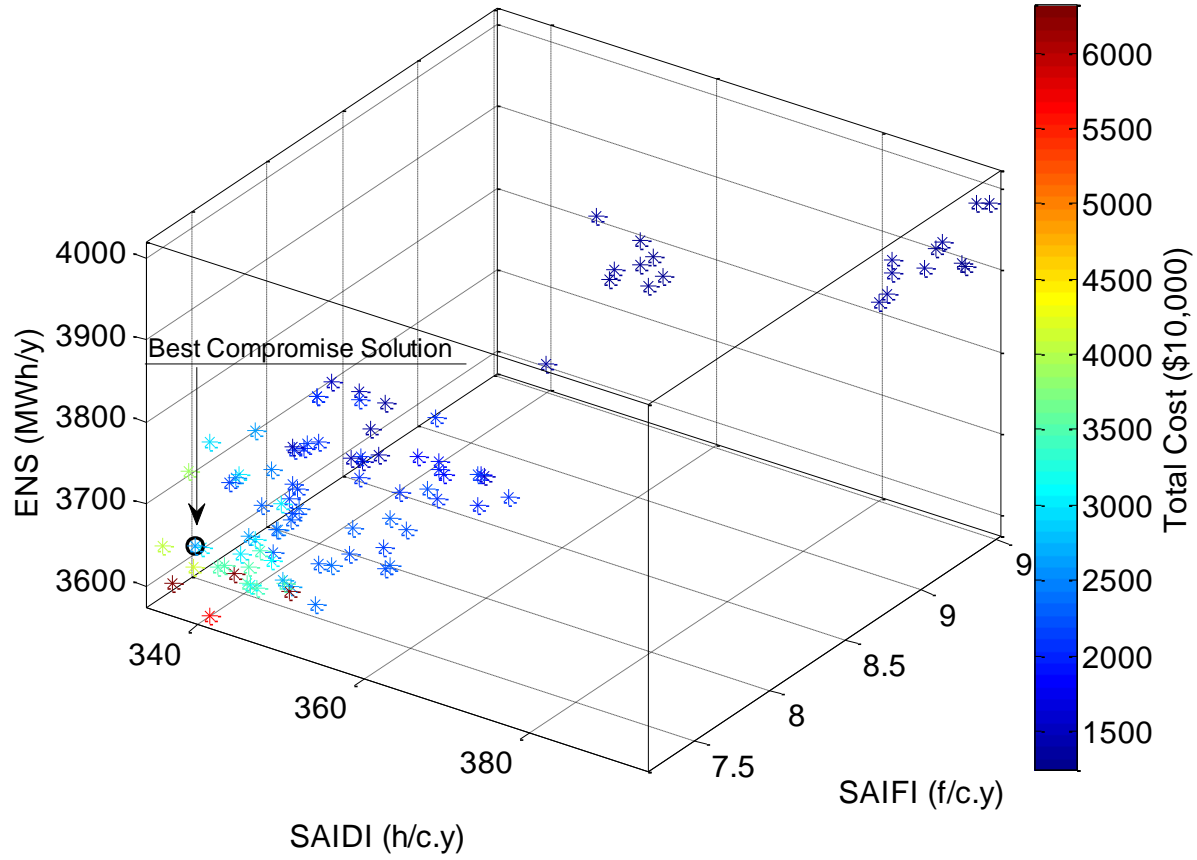


Figure 5.12: Plot of Four Dimensional Pareto Optimal Solutions (Case-1)

The plot of the four dimensional Pareto optimal solutions also shows the best compromise solution (BCS). The Pareto optimal solutions contain 100 solution points. However, other views of the Pareto optimal solutions are plotted in figures 5.13- 5.15. Also, the particle and objectives of the BCS solution are highlighted in table 5.7 given below.

Table 5.7: Variables and Objectives of the Best Compromise Solution (Case-1)

Particle Decision Variables					Objectives			
P_W^R (KW)	P_S^R (KW)	C_B^R (KWh)	P_T^R (KW)	L_{DG} (Bus)	SAIDI (h/c.y)	SAIFI (f/c.y)	ENS (MWh/y)	Total Cost (\$10,000)
5627.636	1619.12	8450.783	7365.021	49	336.4691	7.3679	3636.7367	2652.1345

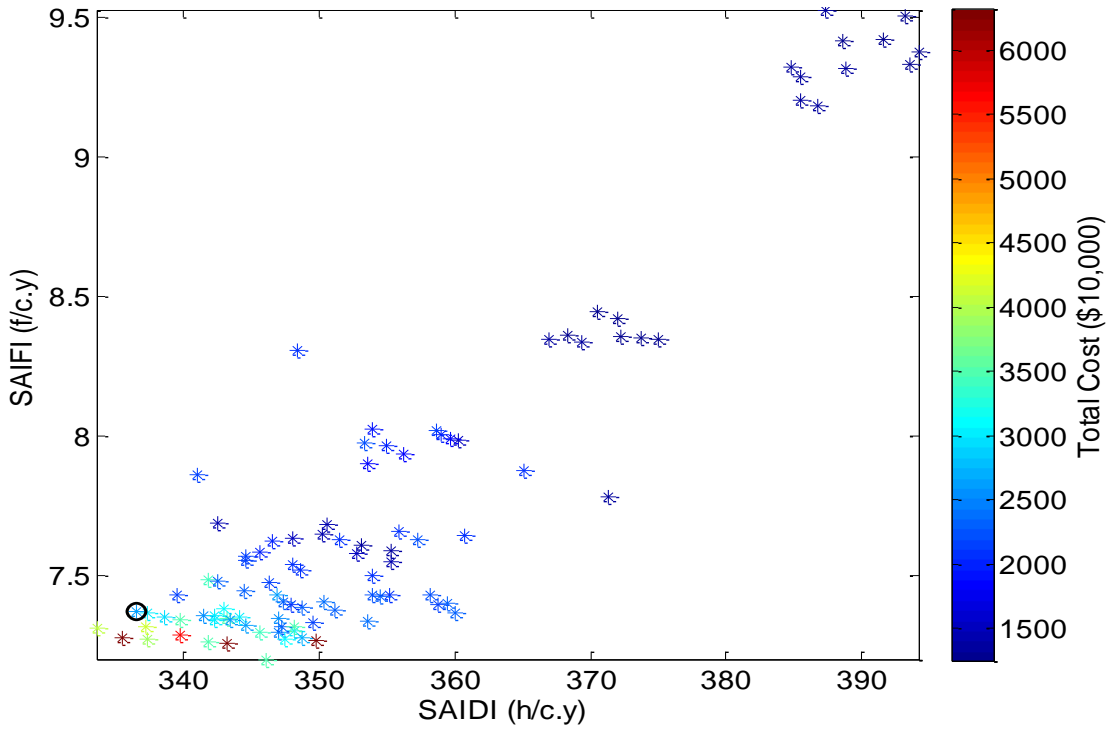


Figure 5.13: Plot of SAIFI, SAIDI and Total Cost

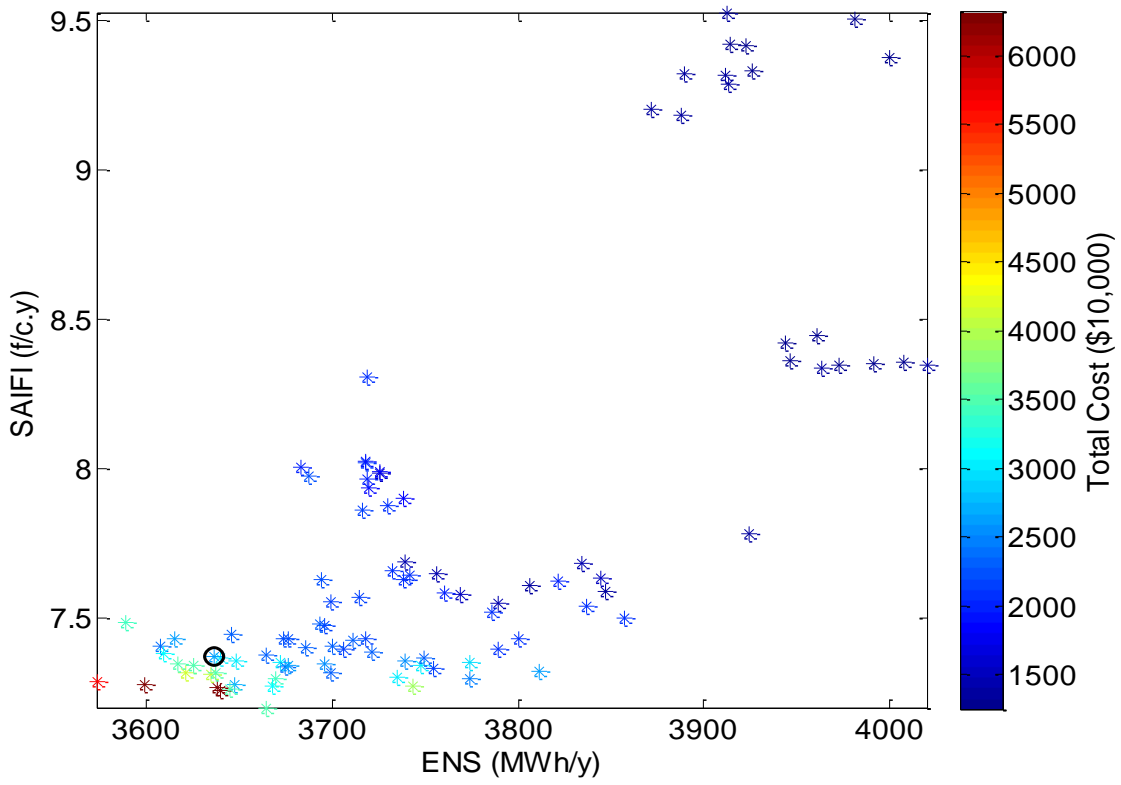


Figure 5.14: Plot of SAIFI, ENS and Total Cost

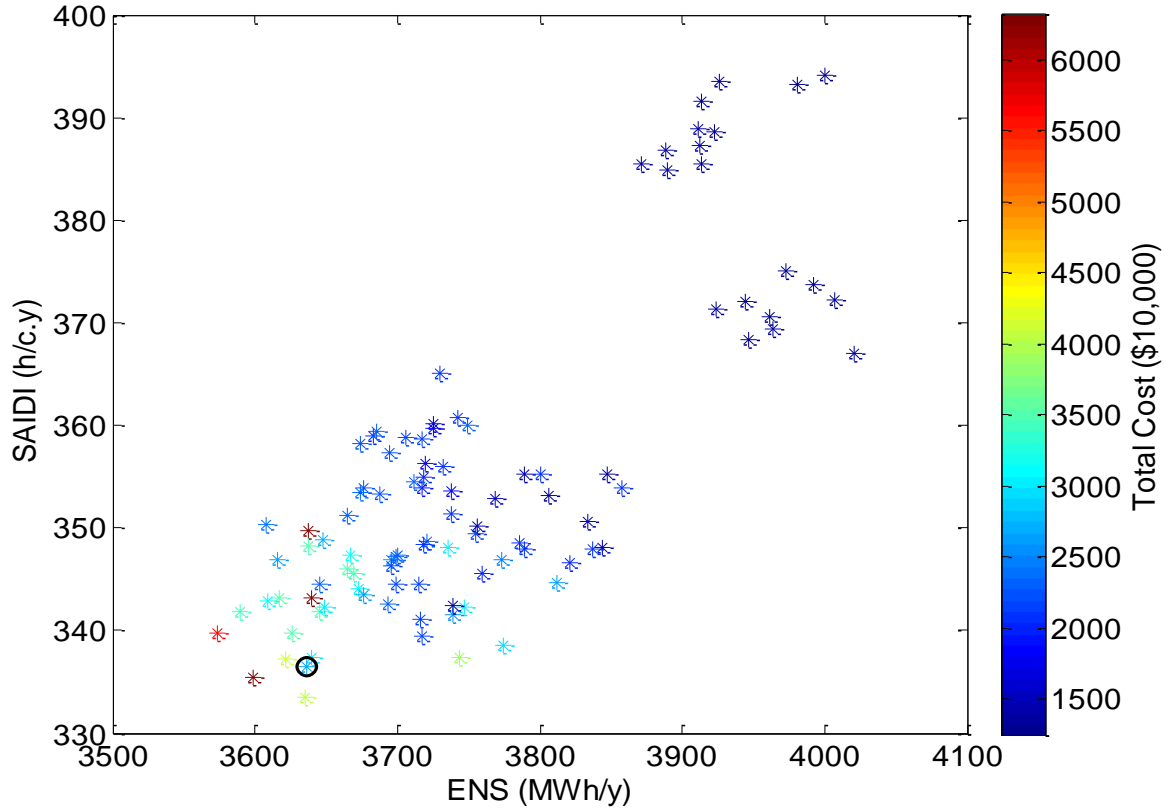


Figure 5.15: Plot of SAIDI, ENS and Total Cost

Furthermore, objective functions' values at both extremes are given and compared with the values at the base case where there are no DGs connected to the system in table 5.8. This gives a view in the direction of the amount of improvement that can be obtained even when two or more locations are chosen for the DG placements. Also, table 5.9 gives all the details of each particle decision variables and corresponding objective functions of the solutions containing the extreme values.

Table 5.8: Comparison of Objective Function Values at both Extremes

Objectives	Base Case (No DGs)	BCS	Case With DGs Installed	
			Minimum	Maximum
SAIDI (h/c.y)	383.3956	336.4691	333.5693	394.1832
SAIFI (f/c.y)	9.340	7.3679	7.1992	9.5255
ENS (MWh/y)	4079.492	3636.7367	3574.0041	4020.6553
Total Cost (\$10,000)	Not Applicable	2652.1345	1247.3576	6312.5785

Table 5.9: Values of the Eight Particles with the Extreme Objective Functions

PARTICLE DECISION VARIABLES					OBJECTIVES			
P_w^R (KW)	P_s^R (KW)	C_B^R (KWh)	P_T^R (KW)	L_{DG} (Bus)	SAIDI (h/c.y)	SAIFI (f/c.y)	ENS (MWh/y)	Total Cost (\$10,000)
Minimum and Maximum SAIDI								
10533.997	3477.545	7108.370	10077.882	15	333.5693	7.3091	3634.6484	4041.9717
3943.333	153.872	2379.029	5041.516	6	394.1832	9.3742	3999.6642	1259.5827
Minimum and Maximum SAIFI								
5320.448	4266.627	10171.950	7683.918	15	346.0237	7.1992	3664.5041	3473.6099
3876.521	166.047	2822.931	5531.846	7	387.2788	9.5255	3912.0823	1337.7581
Minimum and Maximum ENS								
12473.329	8127.877	4298.559	13020.124	15	339.6852	7.2844	3574.0041	5627.5908
4254.077	213.476	2314.286	5457.775	8	366.9481	8.3447	4020.6553	1330.8942
Minimum and Maximum Total Cost								
3468.218	146.954	2809.815	5436.278	7	393.1869	9.5052	3980.7714	1247.3576
12780.237	9582.388	8782.383	9727.498	15	335.4515	7.2768	3598.7543	6312.5785

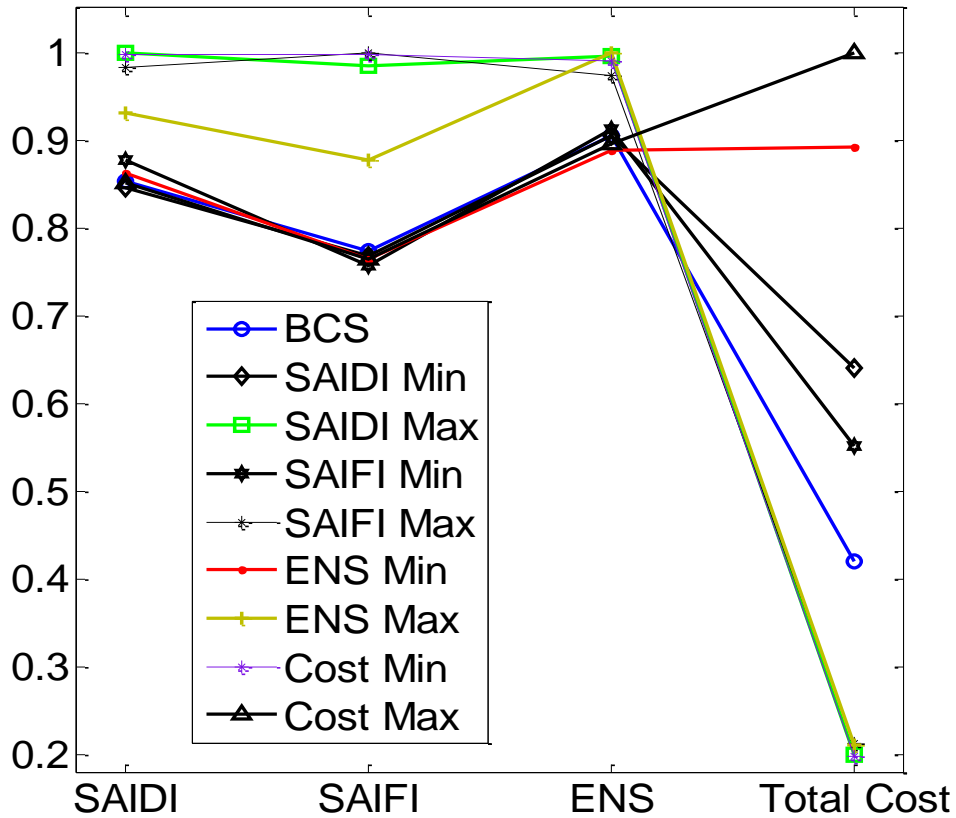


Figure 5.16: Plot of Normalized Objective Values BCS and Extreme Particles (Case-1)

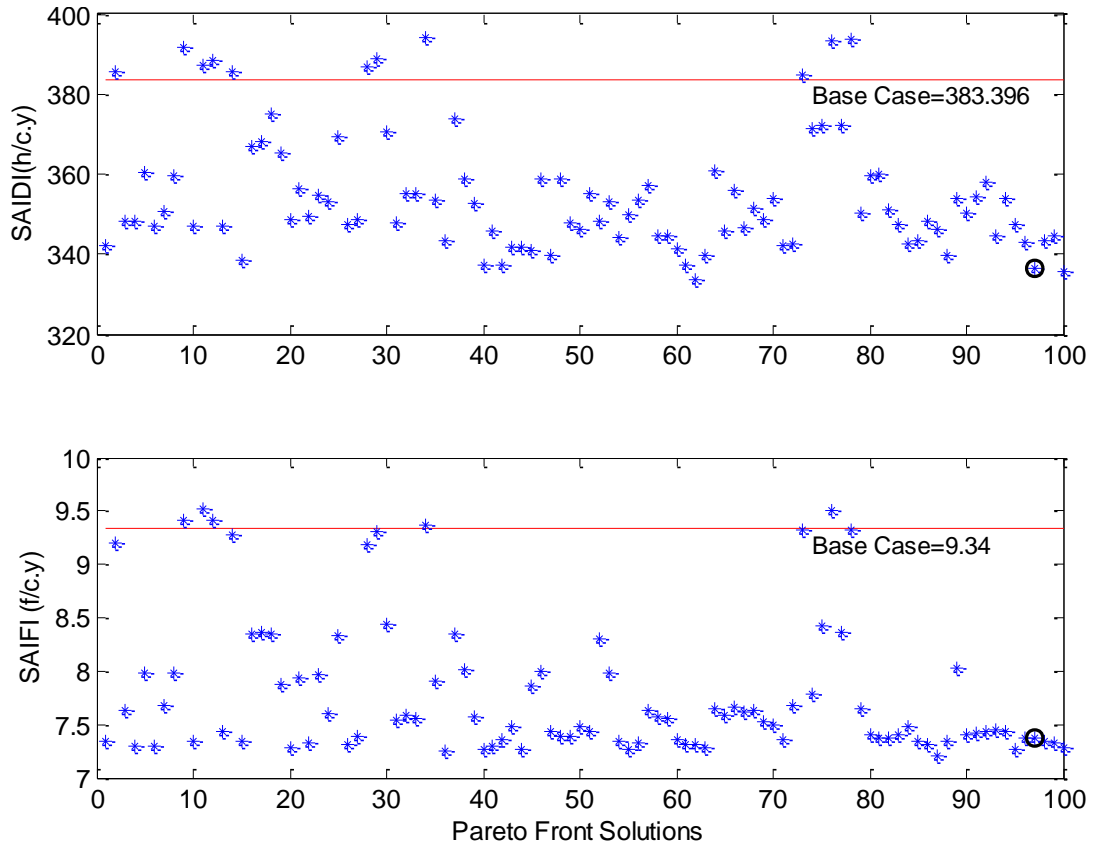


Figure 5.17: Comparison of SAIDI and SAIFI of Pareto Optimal Front with Base Case (Case-1)

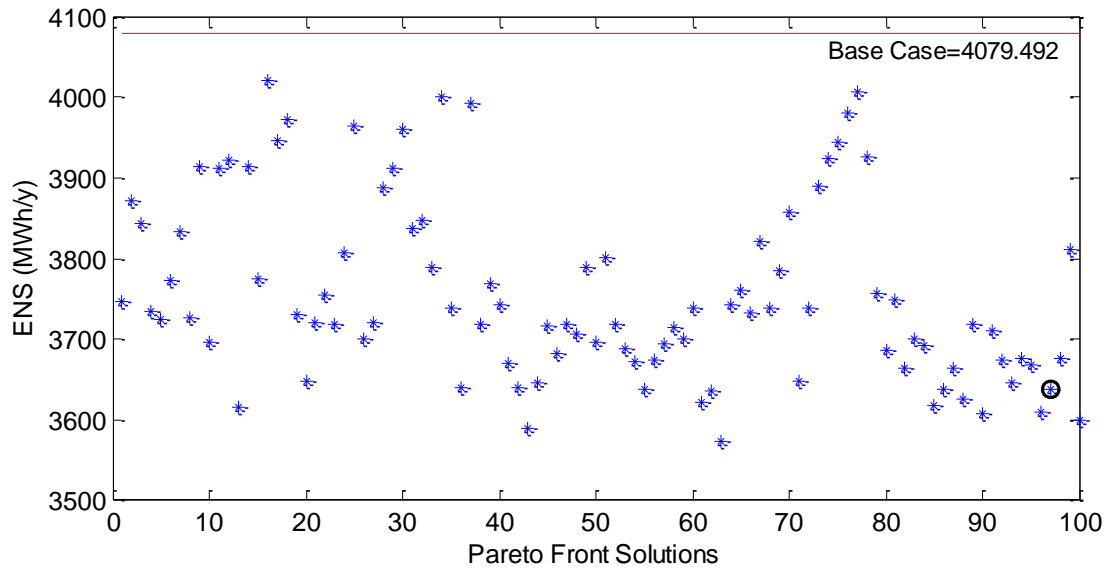


Figure 5.18: Comparison of Energy Not Served of Pareto Optimal Front with Base Case (Case-1)

Furthermore, table 5.10 gives the details of some reliability indices of all LPs based on the best compromise solution. It is obvious that several LPs performance criteria were improved while some LPs remain almost the same. Figure 5.16 shows line graphs of the BCS alongside particles with extreme objective function values given in table 9. Also figures 5.17 and 5.18 shows plots that compare some overall system performance indices, SAIDI, SAIFI and ENS, of all Pareto optimal front solutions with the base case indices. These show notable improvements with a wide variety of solutions to choose from based on personnel interest and budgets.

Table 5.10: Reliability Indices of All Load Points with DGs at BCS (Case-1)

LP	A	λ (f/y)	r (h/f)	AID (h/y)	AUD (h/y)	ENS (MWh/y)	AENS (MWh/c.y)	ENSI (MWh/f)
1	0.966539	5.959409	50.888889	293.120	8466.880	141.583758	0.674208	24.580514
2	0.965382	7.375324	42.592697	303.260	8456.740	141.382241	0.673249	19.857056
3	0.958171	10.081705	37.931677	366.420	8393.580	174.459502	0.830759	18.059989
4	0.958439	8.805981	43.136256	364.070	8395.930	187.171180	187.171181	22.176680
5	0.951473	12.717121	35.131818	425.095	8334.905	219.017594	219.017593	18.100628
6	0.957207	12.097694	32.371762	374.865	8385.135	153.204330	15.320433	13.230080
7	0.953226	14.435191	29.777616	409.740	8350.260	166.184216	16.618422	12.077341
8	0.987076	6.402749	17.913766	113.215	8646.785	153.378049	153.378049	24.268679
9	0.980838	9.542856	17.933226	167.855	8592.145	261.134284	261.134284	27.898962
10	0.961875	6.861598	50.602273	333.975	8426.025	158.814646	0.756260	24.062825
11	0.955197	10.489984	39.169162	392.475	8367.525	188.343580	0.896874	18.796764
12	0.944134	11.290775	45.909006	489.390	8270.610	194.585507	0.972928	18.253799
13	0.947506	12.749256	38.066639	459.845	8300.155	238.204733	238.204733	19.718935
14	0.949403	13.608552	34.305728	443.230	8316.770	227.549447	227.549447	17.612186
15	0.949506	15.418539	30.213456	442.325	8317.675	180.118818	18.011882	12.303198
16	0.962042	4.656760	74.220982	332.510	8427.490	134.540406	13.454041	30.031341
17	0.967523	3.679498	79.914326	284.495	8475.505	115.906754	0.579534	32.558077
18	0.970045	4.144139	65.276119	262.410	8497.590	105.004031	0.525020	26.120406
19	0.962467	4.966405	68.784519	328.790	8431.210	132.047442	0.660237	27.624988
20	0.961338	5.325911	66.148438	338.680	8421.320	172.770732	172.770732	33.744284
21	0.961017	6.597181	53.863565	341.495	8418.505	173.037252	173.037252	27.292942
22	0.962666	7.458458	45.550139	327.050	8432.950	134.924212	13.492421	18.791673

5.3.2 System With All DGs Excluding The Battery (Case-2)

This case studies only four variables, all but the battery size. All other parameters of the optimization are as stated earlier. Hence the four dimensional Pareto optimal front indicating the BCS is shown in figure 5.19. The Pareto optimal solution contains 100 solution points. However, other views of the Pareto optimal solutions are plotted in figures 5.20- 5.22. Also, the particle and objectives of the BCS solution are highlighted in table 5.11.

Table 5.11: Variables and Objectives of the Best Compromise Solution (Case-2)

Particle Decision Variables				Objective Values			
P_w^R (KW)	P_S^R (KW)	P_T^R (KW)	L_{DG} (Bus)	SAIDI (h/c.y)	SAIFI (f/c.y)	ENS (MWh/y)	Total Cost (\$10,000)
2105.499	6727.477	6032.992	15	339.7248	7.2852	3572.9993	2905.5699

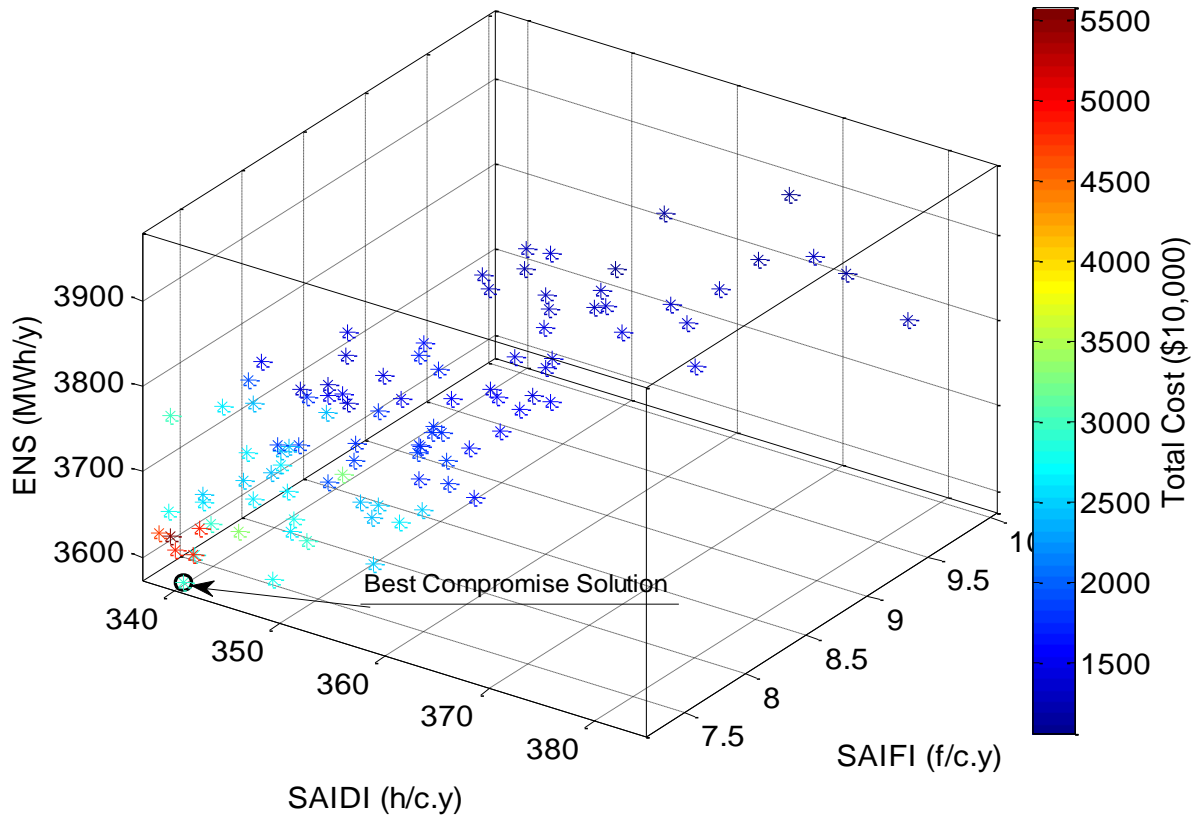


Figure 5.19: Plot of Four Dimensional Pareto Optimal Solutions (Case-2)

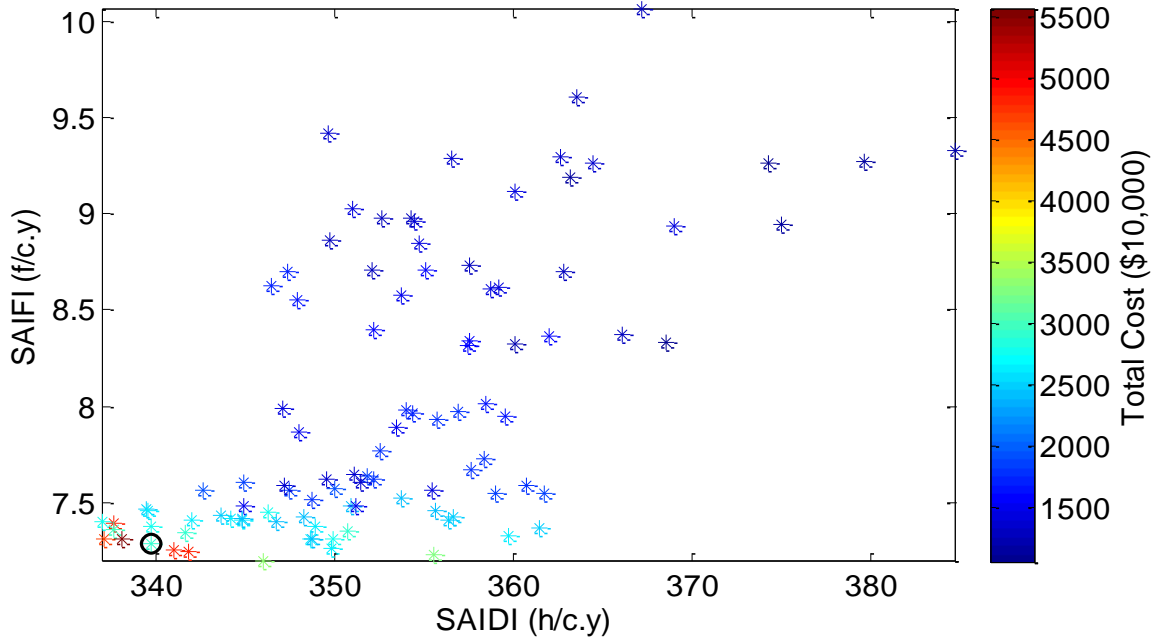


Figure 5.20: Plot of SAIFI, SAIDI and Total Cost (Case-2)

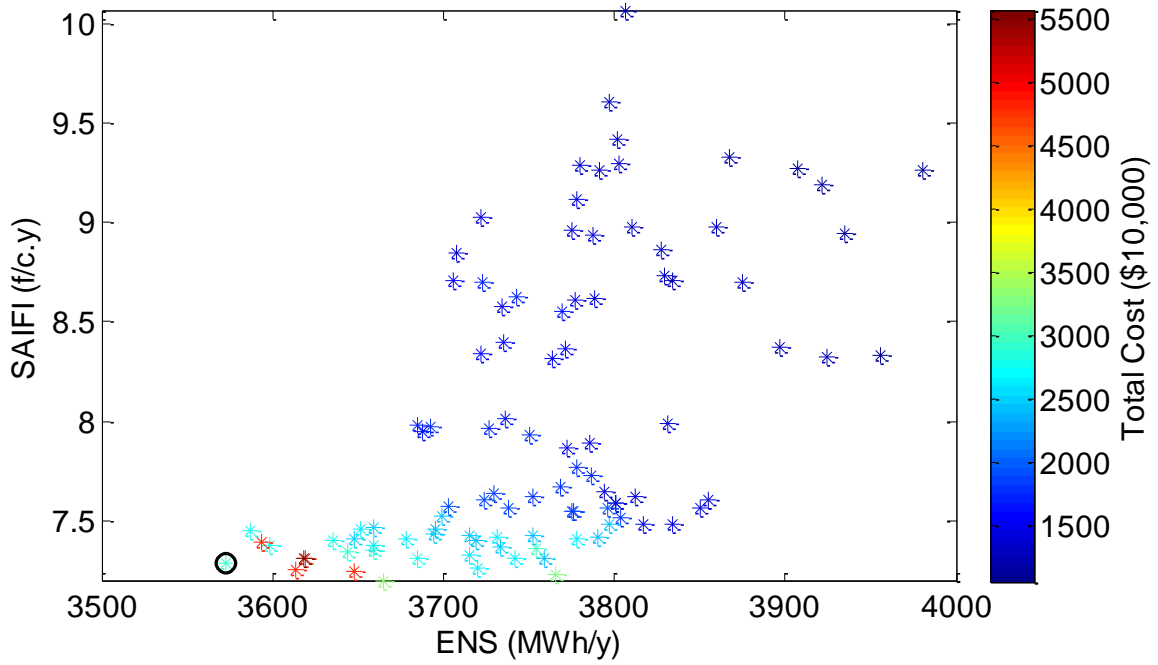


Figure 5.21: Plot of SAIFI, ENS and Total Cost (Case-2)

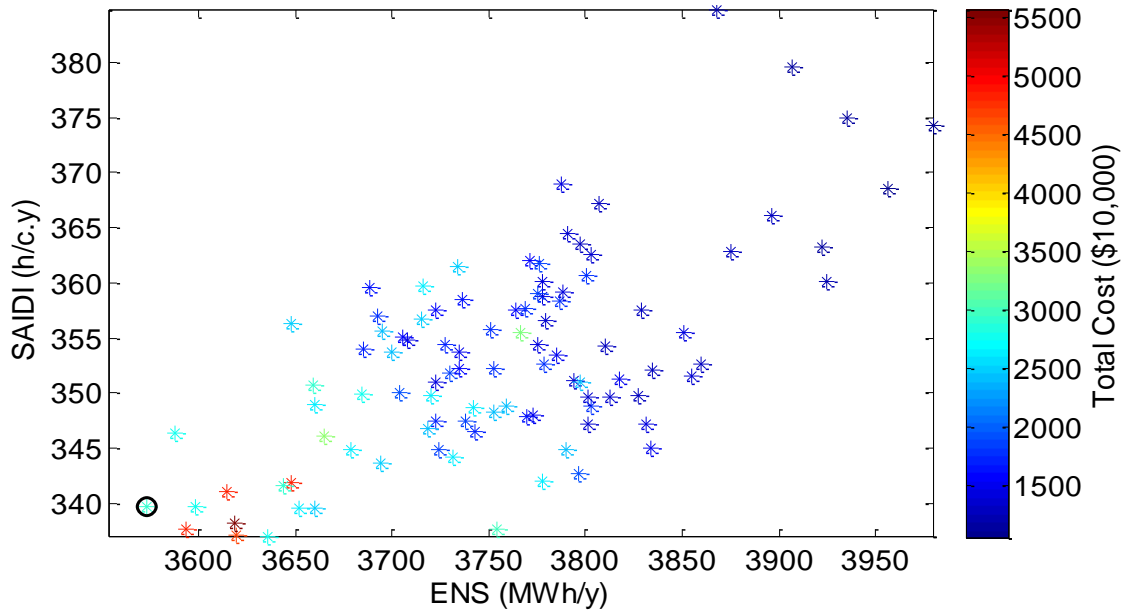


Figure 5.22: Plot of SAIDI, ENS and Total Cost (Case-2)

The extreme values of the objective functions are given and compared with the values at the base case where there are no DGs connected to the system in table 5.12. Also, table 5.13 gives all the details of each particle and corresponding objective functions of the solutions containing the extreme values. Objective values at these extremes alongside the BCS are plotted in figure 5.23. Similar to case-1, figures 5.24-5.25 show comparison of SAIDI, SAIFI and ENS of all Pareto front solutions of case 2 and those of the base case. Also table 5.14 gives LP reliability indices at all LPs for the BCS of case-2.

Table 5.12: Comparison of Objective Function Values at both Extremes (Case-2)

Objectives	Base Case (No DGs)	BCS	Case With DGs Installed	
			Minimum	Maximum
SAIDI (h/c.y)	383.3956	339.7248	336.9907	384.7351
SAIFI (f/c.y)	9.340	7.2852	7.1992	10.0606
ENS (MWh/y)	4079.492	3572.9993	3572.9993	3980.4247
Total Cost (\$10,000)	Not Applicable	2905.5699	1054.6671	5572.7070

Table 5.13: Values of the Eight Particles with the Extreme Objective Functions (Case-2)

PARTICLE DECISION VARIABLES				OBJECTIVES			
P_w^R (KW)	P_S^R (KW)	P_T^R (KW)	L_{DG} (Bus)	SAIDI (h/c.y)	SAIFI (f/c.y)	ENS (MWh/y)	Total Cost (\$10,000)
Minimum and Maximum SAIDI							
1532.8235	6551.2602	6366.0234	15	336.9907	7.4035	3635.2094	2795.8835
942.9921	1964.9322	6487.4541	7	384.7351	9.3242	3867.7818	1257.6006
Minimum and Maximum SAIFI							
966.3281	8102.1926	12326.1791	15	346.0237	7.1992	3664.5041	3372.4569
5132.6756	267.7756	1750.2064	10	367.2067	10.0606	3807.0219	1328.2603
Minimum and Maximum ENS							
2105.4997	6727.4771	6032.9921	15	339.7248	7.2852	3572.9993	2905.5699
4668.1432	64.7235	2113.9015	8	374.2768	9.2590	3980.4247	1054.6671
Minimum and Maximum Total Cost							
4668.1432	64.7235	2113.9015	8	374.2768	9.2590	3980.4247	1054.6671
12697.6538	9437.5281	7543.2478	15	338.1522	7.3129	3618.5778	5572.7070

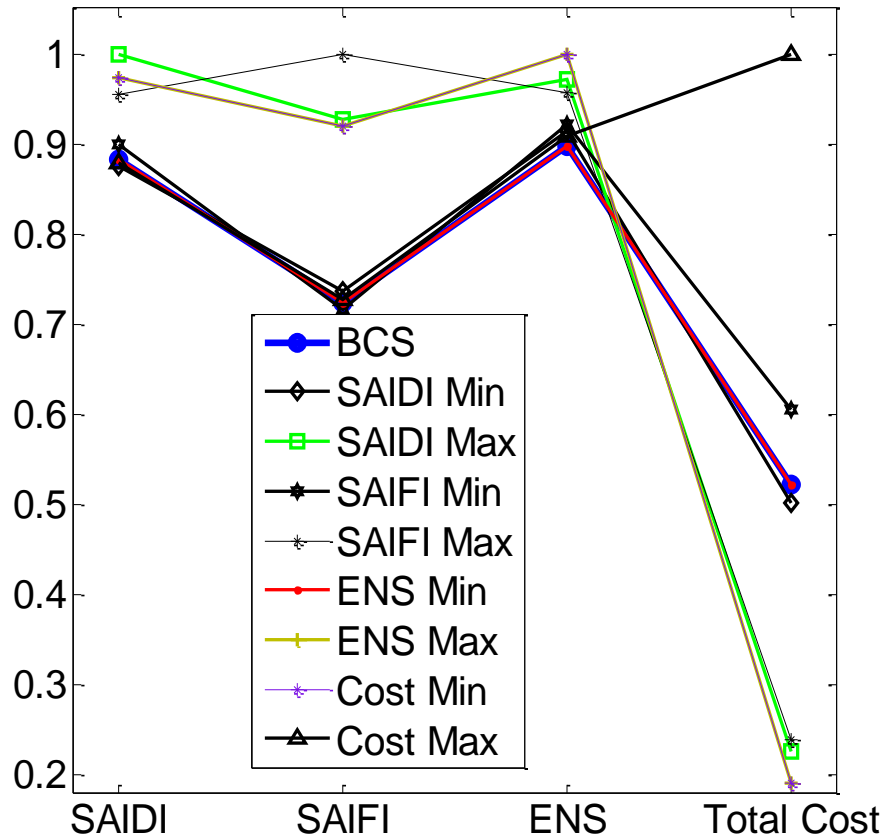


Figure 5.23: Plot of Normalized Objective Values BCS and Extreme Particles (Case-2)

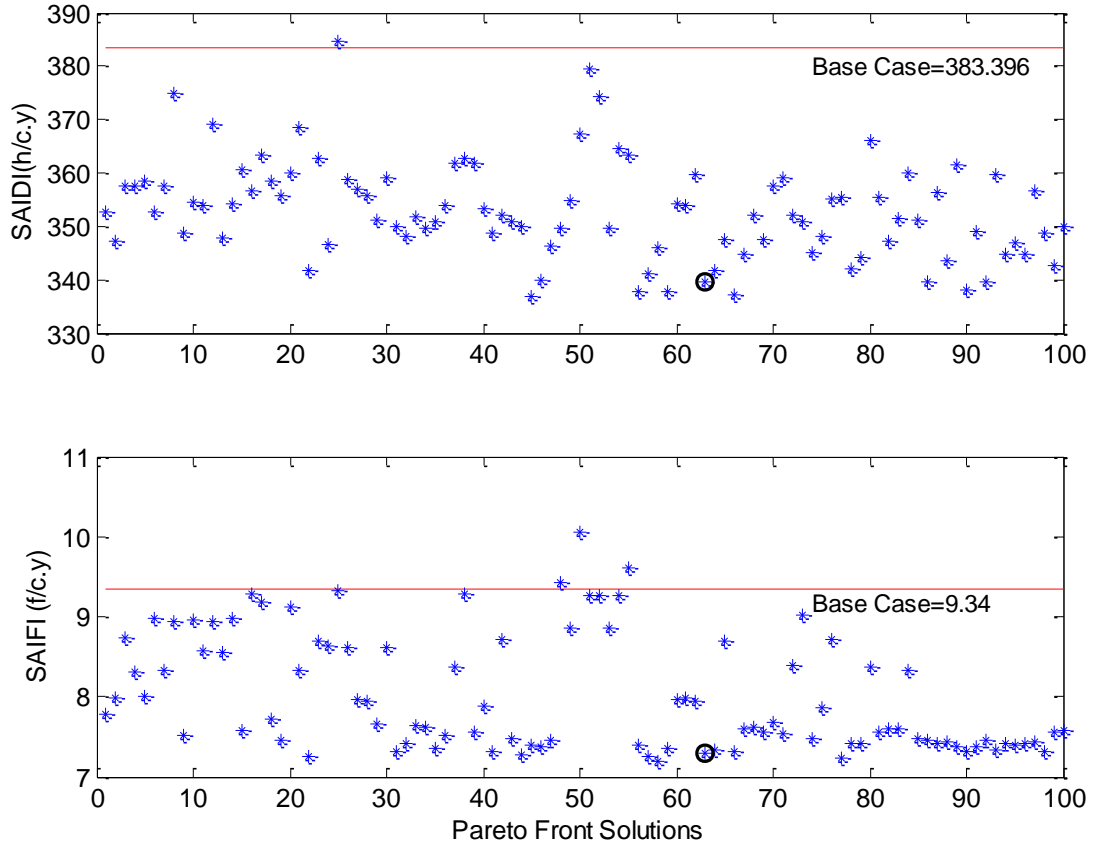


Figure 5.24: Comparison of SAIDI and SAIFI of Pareto Optimal Front with Base Case (Case-2)

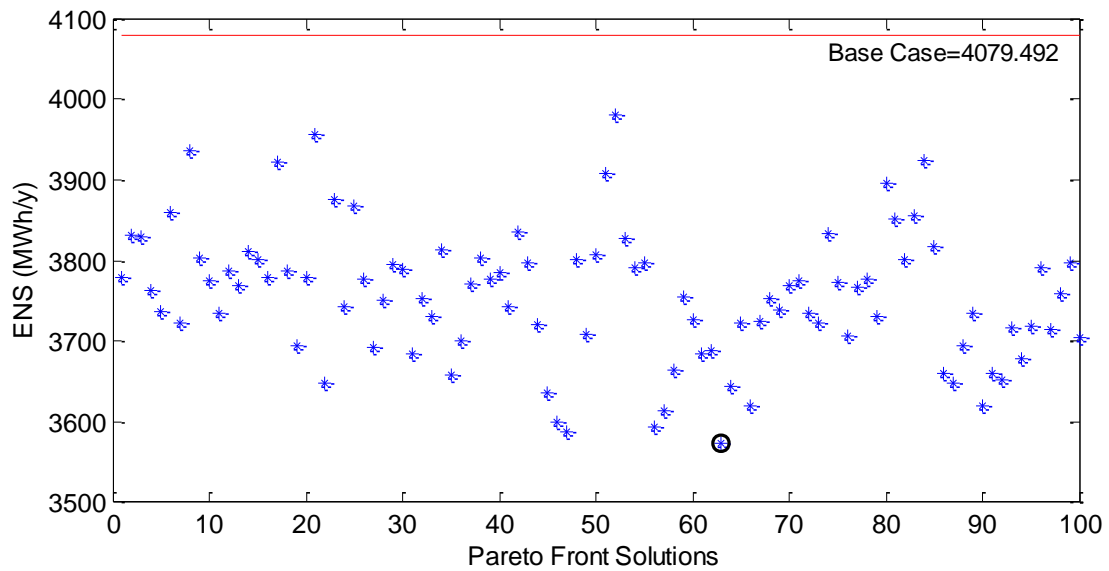


Figure 5.25: Comparison of Energy Not Served of Pareto Optimal Front with Base Case (Case-2)

Table 5.14: Reliability Indices of All Load Points with DGs at BCS (Case-2)

LP	A	λ (f/y)	r (h/f)	AID (h/y)	AUD (h/y)	ENS (MWh/y)	AENS (MWh/c.y)	ENSI (MWh/f)
1	0.962049	6.624751	52.163049	332.452500	8427.54750	158.644216	0.755449	24.891875
2	0.960993	7.755864	45.845036	341.698333	8418.301667	161.703542	0.770017	21.695466
3	0.959020	10.284804	36.395826	358.984167	8401.015833	171.432228	0.816344	17.380759
4	0.955228	9.484644	43.289183	392.200000	8367.8000	201.850963	201.850963	22.279356
5	0.953335	12.839136	33.397399	408.784167	8351.215833	209.816796	209.816796	17.141895
6	0.954527	12.362142	33.757839	398.342500	8361.657500	161.475295	16.147530	13.684347
7	0.949901	15.492843	29.821121	438.867500	8321.132500	177.478458	17.747846	12.059691
8	0.986686	6.395144	18.483228	116.629167	8643.370833	158.653413	158.653413	25.143172
9	0.982838	8.641645	17.701236	150.342500	8609.657500	234.785719	234.785719	27.643530
10	0.961822	6.567393	52.944855	334.435000	8425.56500	160.340793	0.763528	25.383767
11	0.955707	10.292556	39.445019	388.007500	8371.992500	186.313672	0.887208	18.940733
12	0.952313	11.2357997	39.040810	417.736667	8342.263333	167.814574	0.839073	15.683605
13	0.950851	13.153131	34.425307	430.545833	8329.454167	221.584007	221.584007	17.717271
14	0.947778	13.610779	35.462209	457.462500	8302.537500	235.447599	235.447599	18.251752
15	0.945753	15.338747	32.757583	475.203333	8284.796667	192.928932	19.292893	13.299329
16	0.966923	4.429861	67.647471	289.756667	8470.243333	117.590340	11.759034	27.452998
17	0.966257	3.977548	76.909367	295.588333	8464.411667	118.258235	0.591291	30.769706
18	0.968659	4.039949	70.156516	274.545833	8485.454167	110.993259	0.554966	28.362843
19	0.965395	5.313889	59.092105	303.142500	8456.857500	122.091899	0.610459	23.799591
20	0.965675	5.226051	59.581407	300.687500	8459.312500	155.262247	155.262247	30.765307
21	0.965832	4.238143	73.122353	299.314167	8460.685833	154.090417	154.090417	37.644239
22	0.970165	4.906383	54.906688	261.355833	8498.644167	106.006008	10.600601	22.270170

CHAPTER 6

CONCLUSION AND RECOMMENDATION

6.1 Conclusion

This thesis work has shown that the reliability performance of a distribution system can be improved via intelligent location and sizing of wind turbine, solar PV, battery storage system and diesel engines. Several system components models were acquired and harnessed together to obtain the much needed optimization model. The optimization model contained five decision variables and four objective functions, hence producing four dimensional Pareto optimal solutions.

In this thesis work, much emphasis has been placed on the improvement of both LP and entire system reliability performance indices. This thesis has also proposed several methodologies and formulations that can be used to simplify the procedures for obtaining, recording and enumerating the states of components, tie sets, and LPs. The proposed Tie-Set Algorithm and Pseudo-Digitization Technique led to a new form of reliability formulation sets which have been shown to be effective. This thesis work has utilized real-life solar irradiance, temperature and wind speed data to simulate and indicate the location of wind turbine, solar PV, storage and diesel conventional system in a microgrid. The simulation uses the Mixed-Integer Multiple Particle Swarm Optimization technique to arrive at the non-dominated solutions on the basis of five different objective functions. The best compromise solution is also indicated and analyzed. The formulations and exercises in this thesis can be utilized by major power distribution utilities to improve the reliability and reduce the outage costs of each LP and entire system in general.

6.2 Recommendation

Although several works and instances have been discussed and covered in this thesis work, some recommendations still exist. These are outlined below.

1. In this entire thesis work, it has been all about reliability performance and, size and location of hybrid DG systems using several classical reliability indices but power loss. Hence, an additional objective or constraints could be the entire system power loss function via power flow formulations.
2. Amidst the several simulations made in this thesis, the number of locations to be chosen for DG connection is limited. More DGs can be located in the system at different locations with all running simultaneously. This will definitely increase the reliability levels.
3. In another dimension, the entire theme of this thesis could have been the quest to formulate the rightly worldwide acceptable power flow model of a single bus that contains all for types of DGs included in this thesis. However interesting, this dimension will require not just simulations but practical implementations and verifications.

REFERENCES

- [1] A. Keyhani, Design of Smart Power Grid Renewable Energy Systems, New Jersey: John Wiley and Sons, Inc., 2011.
- [2] L. B, "Microgrids; Distributed Power Generation," *Power Engineering Society Winter Meeting*, Columbus, Oh, 2001.
- [3] M. Miner, "Neural Energy," 20 August 2014. [Online]. <http://www.neuralenergy.info/2009/06/micro-grid.html>.
- [4] E. Ghiani, S. Mocci and F. Pilo, "Optimal Reconfiguration of Distribution Networks according to the Microgrid Paradigm," *International Conference on Future Power Systems*, Amsterdam, 2005.
- [5] L. R.H, "MicroGrids," *Power Engineering Society Winter Meeting*, 2002.
- [6] H. Saadat, Power System Analysis, USA: PSA Publishing, 2010.
- [7] J. Guerrero, M. Chandorkar, T. Lee and P. Loh, "Advanced Control Architectures for Intelligent Microgrids—Part I: Decentralized and Hierarchical Control," *IEEE Transactions on Industrial Electronics*, vol. 60, no. 4, pp. 1254 - 1262, 2012.
- [8] M. Institute, "About Microgrids", 2014. [Online] www.microgridinstitute.org/about-microgrids.html.
- [9] R. E. Brow, J. Pan, X. Feng and K. Koutlev, "Sitting Distributed Generation to defer T&D Expansion," *IEEE PES Transmission and Distribution conference*, 2001.
- [10] R. Lasseter, A. Akhil, C. Marnay, J. Stephens, J.Dagle, R. Guttromson, A. S. Meliopoulos, R. Yinger and J. Eto, "White Paper on Integration of Distributed Energy Resources ,The CERTS Microgrid Concept," Berkeley, CA , April 2002.
- [11] P. Piagi and R. H. Lasseter, "Autonomous Control of Microgrids," *IEEE PES Meeting*, Montreal, 2006.
- [12] R.H.Lasseter, "MicroGrids," *Power Engineering Society Winter Meeting, 2002. IEEE (Volume:1)*, USA, 2002.
- [13] N. Hatziargyiou, H. Asano, R. Iravani and C. Marnay, " Microgrids," *IEEE Power and Energy Magazine*, vol. V, no. IV, pp. 78-94 , 2007 .
- [14] J. Kelly, Galvin Electricity Initiative, 20 May 2010. [Online]. www.slideshare.net/galvinpower/john-kelly-microgrid-briefing-on-capitol-hill-5202010.
- [15] W. HL and S. WG, Distributed Power Generation: Planning and Evaluation, CRC Press, 2000.

- [16] B. Hartono, Y. Budiyanto and R. Setiabudy, "Review of MicroGrid Technology," *International Conference on QiR (Quality in Research)*, Yogyakarta, 2013.
- [17] G. Venkataramanan and M. Illindala, "Microgrids and Sensitive Loads," *Power Engineering Society Winter Meeting, IEEE*, Wisconsin, 2002.
- [18] C. Marnay, F. J. Rubio and A. S. Siddiqui, "Shape of the MicroGrid," *Power Engineering Society Winter Meeting, 2001. IEEE*, Columbus, OH, 2001.
- [19] Y. Attwa and E. El-Saadany, "Reliability Based Analysis for Optimum Allocation of DG," *IEEE Canada Electrical Power Conference, 2007. EPC 2007*, Montreal, 2007.
- [20] M. Silverman, "Green Reliability," *Annual Reliability and Maintainability Symposium (RAMS)*, Florida, 2011.
- [21] J. Glover, S. Mulukutla, Thomas and J. Overbye, "Power Distribution," *Power System Analysis and Design*, Stamford, Cengage Learning, pp. 757-807, 2012.
- [22] C. A and K. D, *Power Distribution System Reliability: Practical Methods and Evaluations*, Wiley-IEEE Press, 2009.
- [23] O. S. A., "Real-Time Evaluation of System Dynamics to Improve Network Performance in Akure Electric Power Distribution System in Nigeria," *Electrical and Electronic Engineering (Published online at <http://journal.sapub.org/eee>)*, 2013.
- [24] G. P. R. V. and O. R. V., "Mitigation of Fault in the Distribution System by using Flexible Distributed Static Compensator (FD-STATCOM)," *International Journal of Modern Engineering Research (IJMER)*, vol. III, no. 4, pp. 2367-2373, 2013.
- [25] R. R., S. K. K. and R. N., "Power System Reconfiguration in a Radial Distribution Network for Reducing Losses and to Improve Voltage Profile Using Modified Plant Growth Simulation Algorithm with Distributed Generation," *Energy Reports*, vol. I, pp. 116-122, 2015.
- [26] H. Müller and T. Connor, "New 20kV network concept for an existing distribution network," in *China International Conference on Electricity Distribution (CICED)*, Nanjing, 2010.
- [27] H. Farhangi, "The Path of the Smart Grid," *IEEE Power and Energy*, vol. VIII, no. 1, pp. 18-28, 2010.
- [28] B. Kroposki, R. Lasseter, T. Ise, S. Morozumi, S. Papatlianassiou and N. Hatziaargyriou, "Making Microgrids Work," *IEEE Power and Energy*, vol. VI, no. 3, pp. 40-53, 2008.
- [29] B. Poornazaryan, P. Karimyan, G. G.B. and M. Abedi, "Optimal Allocation and Sizing of DG Units Considering Voltage Stability, Losses and Load Variations," *International Journal of Electrical Power & Energy Systems*, vol. 79, p. 42-52, 2016.

- [30] P. R. Benvindo, M. d. C. Geraldo, J. Contreras and J. S. Mantovani, "Optimal Distributed Generation and Reactive Power Allocation in Electrical Distribution Systems," *IEEE Transactions on Sustainable Energy*, vol. PP, no. 99, pp. 1-10, 2016.
- [31] A. Ameli, S. Bahrami, F. Khazaeli and M.-R. Haghifam, "A Multiobjective Particle Swarm Optimization for Sizing and Placement of DGs from DG Owner's and Distribution Company's Viewpoints," *IEEE Transactions on Power Delivery*, vol. 29, no. 4, pp. 1831-1840, 2014.
- [32] S. N. G. Naik, D. K. Khatod and M. P. Sharma, "Analytical Approach for Optimal Siting and Sizing of Distributed Generation in Radial Distribution Networks," *IET Generation, Transmission & Distribution*, vol. 9, no. 3, pp. 209-220, 2015.
- [33] H. B. Tolabi, M. H. Ali and R. M., "Simultaneous Reconfiguration, Optimal Placement of DSTATCOM, and Photovoltaic Array in a Distribution System Based on Fuzzy-ACO Approach," *IEEE Transactions on Sustainable Energy*, vol. VI, no. 1, pp. 210-218, 2014.
- [34] N. Kanwar, N. Gupta, N. K.R. and A. Swarnkar, "Improved Meta-Heuristic Techniques for Simultaneous Capacitor and DG Allocation in Radial Distribution Networks," *International Journal of Electrical Power & Energy Systems*, vol. 73, pp. 653-664, 2015.
- [35] W. Sheng, K.-Y. Liu, Y. Liu, X. Meng and Y. Li, "Optimal Placement and Sizing of Distributed Generation via an Improved Nondominated Sorting Genetic Algorithm II," *IEEE Transactions on Power Delivery*, vol. 30, no. 2, pp. 569-578, 2015.
- [36] Y. Hegazy, M. Othman, W. El-Khattam and A. Abdelaziz, "Optimal Sizing and Siting of Distributed Generators Using Big Bang Big Crunch Method," *International Universities Power Engineering Conference*, Cluj-Napoca, 2014
- [37] K. Nekooei, M. F. M., H. Nezamabadi-Pour and K. L. Y., "An Improved Multi-Objective Harmony Search for Optimal Placement of DGs in Distribution Systems," *IEEE Transactions on Smart Grid*, vol. IV, no. 1, pp. 557-567, 2013.
- [38] K. Zhan, Z. Hu, Y. Song, Z. Luo, Z. Xu and L. Jia, "Coordinated Electric Vehicle Charging Strategy for Optimal Operation of Distribution Network," *Innovative IEEE PES International Conference and Exhibition on Innovative Smart Grid Technologies*, Berlin, 2012.
- [39] Wikipedia, "Photovoltaics," 29 September 2015.[Online] <https://en.wikipedia.org/wiki/Photovoltaics>.
- [40] Wikipedia. [Online]. Available: en.wikipedia.org/wiki/Wind_power.
- [41] G. Barker and P. Norton, "Predicting Long-Term Performance of Photovoltaic Arrays Using Short-Term Test Data and an Annual Simulation Tool," NREL, 2003.

- [42] W. DeSoto, S. Klein and W. Beckman, "Improvement and Validation of a Model for Photovoltaic Array Performance," *Solar Energy*, vol. 80, pp. 78-88, 2006.
- [43] D. King, W. Boyson and J. Kratochvil, "Photovoltaic Array Performance Model, Sandia Report No. SAND2004-3535," Sandia National Laboratory, 2004.
- [44] A. H. Arab, F. Chenlob and M. Benghanemc, "Loss-of-Load Probability of Photovoltaic Water Pumping Systems," *Solar Energy*, vol. 76, no. 6, pp. 713-723, 2004.
- [45] H. Tian, F. Mancilla-David, K. Ellis, E. Muljidi and P. Jenkins, "A Detailed Performance Model for Photovoltaic Systems," NREL, 2012.
- [46] P. Pandey and K. Sandhu, "Multi Diode Modelling of PV Cell," *IEEE 6th India International Conference on Power Electronics (IICPE)*, pp. 1-4, 8-10 December 2014.
- [47] M. Suthar, G. Singh and R. Saini, "Comparison of Mathematical Models of Photo-Voltaic (PV) Module and Effect of Various Parameters on its Performance," *International Conference on Energy Efficient Technologies for Sustainability (ICEETS)*, pp. 1354-1359, 10-12 April 2013.
- [48] J. J. Soon and K.-S. Low, "Optimizing Photovoltaic Model for Different Cell Technologies Using a Generalized Multidimension Diode Model," *IEEE Transactions on Industrial Electronics*, vol. LXII, no. 10, pp. 6371 - 6380, 2015.
- [49] O. Wasynczuk, D. Man and J. Sullivan, "Dynamic Behaviour of A Class of Wind Turbine Generators During Random Wind Fluctuations," *IEEE Transactions on Power Apparatus and Systems*, Vols. PAS-100, no. 6, pp. 2837-2845, 1981.
- [50] P. Anderson and A. Bose, "Stability Simulation of Wind Turbine Systems," *IEEE Transactions on Power Apparatus and Systems*, Vols. PAS-102, no. 12, pp. 3791 - 3795, 1983.
- [51] J. A. Duffie and W. A. Beckman, *Solar Engineering of Thermal Processes*, Wiley, 2013.
- [52] M. Singh and S. Santoso, "Dynamic Models for Wind Turbines and Wind Power Plants," NREL, Texas, 2011.
- [53] S. Muyeen, J. Tamura and T. Murata, *Stability Augmentation of a Grid-connected Wind Farm*, London: Springer-Verlag, 2009.
- [54] J. Slootweg, *Wind Power: Modeling and Impact on Power System Dynamics*, Delft: Dissertation, 2003.
- [55] A. Manyonge, R. Ochieng, F. Onyango and J. Shichikha, "Mathematical Modeling of Wind Turbine in a Wind Energy Conversion System: Power Coefficient Analysis," *Applied Mathematical Sciences*, vol. VI, no. 91, pp. 4527-4536, 2012.

- [56] K. Halicka, P. Lombardi and Z. Styczynski, "Future-Oriented Analysis of Battery Technologies," *IEEE International Conference on Industrial Technology (ICIT)*, pp. 1019-1024, 17-19 March 2015.
- [57] A. A. Hussein and I. Batarseh, "An Overview of Generic Battery Models," *IEEE Power and Energy Society General Meeting*, pp. 1-6, 24-29 July 2011.
- [58] S. Kai and S. Qifang, "Overview of the Types of Battery Models," *30th Chinese Control Conference (CCC)*, pp. 3644-3648, 22-24 July 2011.
- [59] A. Sparacino, G. Reed, R. Kerestes, B. Grainger and Z. Smith, "Survey of Battery Energy Storage Systems and Modeling Techniques," *IEEE Power and Energy Society General Meeting*, pp. 1-8, 22-26 July 2012.
- [60] M. Ceraolo, "New Dynamical Models of Lead–Acid Batteries," *IEEE Transactions on Power Systems*, vol. XV, no. 4, pp. 1184-1190, 2000.
- [61] N. Medora and A. Kusko, "An Enhanced Dynamic Battery Model of Lead-Acid Batteries Using Manufacturers' Data," *28th Annual International Telecommunications Energy Conference*, pp. 1-8, 2006.
- [62] CanadianSolar, "Solar Modules," [Online]. Available: www.canadiansolar.com/solar-panels/cs6x-p.html.
- [63] wind-turbine-models.com, "General Electric GE 1.5s (Turbine)," 2 May 2013. [Online]. Available: en.wind-turbine-models.com/turbines/565-general-electric-ge-1.5s.
- [64] R. Billinton and R. N. Allan, *Reliability Evaluation of Engineering Systems*, New York: Plenum Publishing Corporation, 1992.
- [65] R. Allan, R. Billinton and M. de Oliveira, "An Efficient Algorithm for Deducing the Minimal Cuts and Reliability Indices of a General Network Configuration," *IEEE Transactions on Reliability*, Vols. R-25, no. 4, pp. 226 - 233, 1976.
- [66] M. A. Abido, "Optimal Power Flow using Particle Swarm Optimization," *International Journal of Electrical Power & Energy Systems*, vol. 24, no. 7, pp. 563-571, 2002.
- [67] C. A. Coello and M. S. Lechuga, "MOPSO: A Proposal for Multiple Objective Particle Swarm Optimization," Honolulu, 2002.
- [68] M. A. Abido, "Multiobjective Particle Swarm for Environmental/Economic Dispatch Problem," *International Power Engineering Conference*, Singapore, 2007.

- [69] E. Zitzler and L. Thiele, "Multiobjective Evolutionary Algorithms: A Comparative Case Study and the Strength Pareto Approach," *IEEE Transactions on Evolutionary Computation*, vol. 3, no. 4, pp. 257-271, 1999.
- [70] L. Li and F. Liu, *Group Search Optimization for Applications in Structural Design*, Springer-Verlag, 2011.
- [71] M. A. Abido, "Environmental/Economic Power Dispatch using Multiobjective Evolutionary Algorithms," *IEEE Transactions on Power Systems*, vol. XVIII, no. 4, pp. 1529-1537, 2003.
- [72] R. N. Allan, B. R., S. I., G. L. and S. K. So, "A Reliability Test System for Educational Purposes - Basic Distribution System Data and Results," *IEE Transactions on Power Systems*, vol. Vol1.6, no. No. 2, pp. 813-820, May 1991.
- [73] NPL, "When do the four seasons officially begin? (FAQ - Time)," 8 October 2014. [Online]. Available: [www.npl.co.uk/science-technology/time-frequency/time/faqs/when-do-the-four-seasons-officially-begin-\(faq-time\)](http://www.npl.co.uk/science-technology/time-frequency/time/faqs/when-do-the-four-seasons-officially-begin-(faq-time)).
- [74] IRENA, "Renewable Power Generation Costs in 2014," 2015.
- [75] IRENA, "Battery Storage for Renewables: Market Status and Technology Outlook," 2015.
- [76] "University of Oregon Solar Radiation Monitoring Laboratory," [Online]. Available: <http://solardat.uoregon.edu/SelectMonthlyAverage.html>.
- [77] B. P. Administration, "Meteorological Information from BPA Weather Sites," [Online]. Available: <http://transmission.bpa.gov/business/operations/wind/MetData.aspx>

VITAE

Name : YAHAYA AFOLABI ABASS
Nationality : Nigerian
Date of Birth : 1st May, 1986
Email : aayahaya5@gmail.com
Address : 26, Chief Taiwo Goriola Street, Sabo Sagamu, Ogun State, Nigeria.

Academic Background:

2016: **Master of Science** (Electrical Engineering),
King Fahd University of Petroleum and Minerals, Saudi Arabia.
CGPA: 3.675/4.000

2010: **Bachelor of Technology** (Electronic and Electrical Engineering)
Ladoke Akintola University of Technology, Nigeria.
CGPA: 4.34/5.00

2003: **Senior Secondary School Certificate**
Okota Grammar School, Okota Isolo, Lagos State, Nigeria.

Publications:

1. **Abass Yahaya** and Mohammad Al-Muhaini, "Reliability Assessment of Load Points Including Solar and Wind DGs", Accepted for presentation/publication in the International Symposium on Smart Electric Distribution Systems and Technologies (EDST) CIGRE SC C6Colloquium, Vienna, Austria, September 2015.
2. **Yahaya A. Abass**, Ali T. Al-Awami, and Taskin Jamal. "Integrating Generation Control and Economic Dispatch for Microgrid Real-Time Optimization", Accepted for presentation at the 2016 IEEE PES General Meeting, Boston, USA.

Memberships:

1. Student Member of Institute of Electrical and Electronics Engineers (IEEE)
2. IEEE King Fahd University of Petroleum and Minerals (KFUPM) Society
3. Cisco Certified Network Academy (CCNA-1) Student Member